2008

PRESSURE-TEMPERATURE EVOLUTION OF METAPELITES WITHIN THE ANACONDA METAMORPHIC CORE COMPLEX, SOUTHWESTERN MONTANA

Erin Haney
The University of Montana

Recommended Citation

Haney, Erin, "PRESSURE-TEMPERATURE EVOLUTION OF METAPELITES WITHIN THE ANACONDA METAMORPHIC CORE COMPLEX, SOUTHWESTERN MONTANA" (2008). *Graduate Student Theses, Dissertations, & Professional Papers*. 1262.
https://scholarworks.umt.edu/etd/1262

PRESSURE-TEMPERATURE EVOLUTION OF METAPELITES WITHIN THE ANACONDA METAMORPHIC CORE COMPLEX, SOUTHWESTERN MONTANA

By

Erin Marie Haney

B.S. Geology, Sonoma State University, Rohnert Park, CA, 2005

Thesis

presented in partial fulfillment of the requirements
for the degree of

Master of Science
in Geosciences

The University of Montana
Missoula, MT

Spring 2008

Approved by:

Dr. David A. Strobel, Dean
Graduate School

Dr. Julie Baldwin, Chair
Department of Geosciences

Dr. James Sears
Department of Geosciences

Dr. Paul Wilson
Department of Geography

Haney, Erin, M.S., May 2008 Geosciences

Pressure-temperature evolution of metapelites within the Anaconda metamorphic core complex, southwestern Montana

Chairperson: Dr. Julie Baldwin

This study shows the complete metamorphic evolution of metapelitic footwall rocks in the Anaconda metamorphic core complex, located in southwestern Montana. Pseudosections were constructed using the computer program THERMOCALC (*v. 3.26*) in conjunction with the internally consistent dataset of Holland and Powell (1998, version 5.5, updated Nov. 2003) in the model system NCKFMASH (Na_2O-CaO-K_2O-FeO-MgO-Al_2O_3-SiO_2-H_2O). Microprobe data reveals that garnet is very almandine rich and contains very little manganese, thus not requiring MnO as a component in the model system. X-ray mapping of garnet within metapelites indicate only one growth phase. Petrographic analysis in conjunction with pseudosections reveal peak metamorphism occurred at 3.3-5.3 kbars and 590-665°C with an assemblage of biotite + garnet + sillimanite + quartz + plagioclase + muscovite. Chemical composition of garnet, biotite, and plagioclase all verify peak metamorphic conditions on contoured pseudosections. Evolution of footwall rocks occurred along a prograde, clockwise path that was largely stable within sillimanite stability as evidenced by its abundance. These amphibolite facies metapelites equilibrated at or near the solidus.

ACKNOWLEDGMENTS

I would like to thank my advisor, Dr. Julie Baldwin, for all of her guidance while completing this project. I am grateful for all of her understanding and patience; this thesis would not have been completed without her. I also thank my committee members Dr. James Sears and Dr. Paul Wilson for their review of this document.

I thank my previous instructors who instilled a love for geology in me. Mr. Morse, my high school geology teacher, not only opened the door into the world of geology, but he also taught us how to hold strong in the face of doubt. Geology at Sonoma State University was an entirely different experience; sink or swim the decision was yours, there was no just getting your feet wet. Taking the plunge meant years of struggling to stay afloat, fortunately Dr. Rolfe Erickson, Dr. Tom Anderson, and Dr. Walt Vennum were there to teach you the strokes. Each of these professors showed me a different field of geology while instilling a sense of logic and reasoning in me. I especially thank Dr. Walt Vennum for introducing me to metamorphic geology and giving me a solid foundation in this science.

Everyone who assisted me in the field is appreciated, whether we reached the outcrop or not. Mark Wollam, Heather Henry, Jessica Bleha, and Doc Richardson I thank you, as without sample collection this project would not exist. I thank Connie Brown for all of our interesting and thought provoking discussions.

I could not have completed this thesis without the support and encouragement from my family. Every bump and stumble I came across on this long road, they were there to help me up and get me on my way again. I do not posses the words to express my appreciation for them. All I can say is thank you, thank you for everything.

Funding for this project was provided by Geological Society of America and Tobacco Root Geological Society grants.

TABLE OF CONTENTS

Page

APPENDICES

LIST OF TABLES

LIST OF FIGURES

CHAPTER 1

INTRODUCTION

Mountain belts occur worldwide as a result of earth's tectonic processes. As these features are uplifted and eroded their cores are exposed, revealing metamorphic rocks that hold the pieces needed to unravel the puzzle of the landscapes' formation. Once this puzzle is complete, the tectonic processes can be established, allowing for an improved understanding of the earth's dynamic behavior.

Metamorphic core complexes (MCCs) in the North American Cordillera developed during Eocene time as a result of oblique transtension between the North America and the Kula, Farallon, and Pacific plates (Foster et al., 2007; Eyal et al., 2006; Vanderhaeghe et al., 2003; Liu, 2001). Following crustal shortening and thickening from >100-56 Ma (House, 1997), large scale extension ensued, exposing mid-crustal metamorphic rocks in the footwalls of large detachment systems. MCCs are characterized by a low angle detachment fault that separates an unmetamorphosed hanging wall from a metamorphic and/or igneous footwall (Coney and Harms, 1984). These terranes are often characterized by a polymetamorphic history related to episodes of convergence and extension. Commonly, two or three metamorphic events are evident within the northern North American Cordilleran core complexes: 1) an older event related to protolith metamorphism, 2) a Jurassic to Cretaceous amphibolite facies event corresponding to Sevier orogenesis, and 3) greenschist to lower amphibolites facies overprinting during Tertiary normal faulting.

This study focuses on the petrology of pelitic schists of the Prichard Formation of the Belt Supergroup in the footwall of the Anaconda MCC 100 km east of the Bitterroot MCC in southwestern Montana (Fig. 1-1). Constraining peak pressures-temperature (*P-T)* conditions and the metamorphic evolution of the Anaconda metamorphic core complex (AMCC) footwall elucidates the orogenic processes operating during the Sevier orogeny prior to collapse of the orogen. The AMCC, exposed in the Flint Creek and Anaconda-Pintlar ranges, was recently described by O'Neill et al. (2003) (Figure 1-2), making it the easternmost complex in the chain of Cordilleran metamorphic core complexes that occurs from northern Mexico to southern Canada (Coney and Harms, 1984) (Figure 1-3). Integrated petrographic, chemical, and quantitative phase equilibria studies provide constraints on the metamorphic evolution of the AMCC. Mineral assemblage stabilities were modeled in the chemical system NCKFMASH (Na_2O-CaO- K_2O-FeO-MgO-Al_2O_3-SiO_2-H2O) using the phase equilibria modeling program THERMOCALC. The close proximity and similar rock types exposed in the AMCC compared to the Bitterroot and Clearwater metamorphic core complexes suggests that they have all undergone similar evolutions; however this study reveals that the AMCC exposes shallower crustal levels, which may relate to the aspect ratio of the Anaconda MCC compared to the adjacent complexes and yield insight into the processes responsible for orogenic collapse.

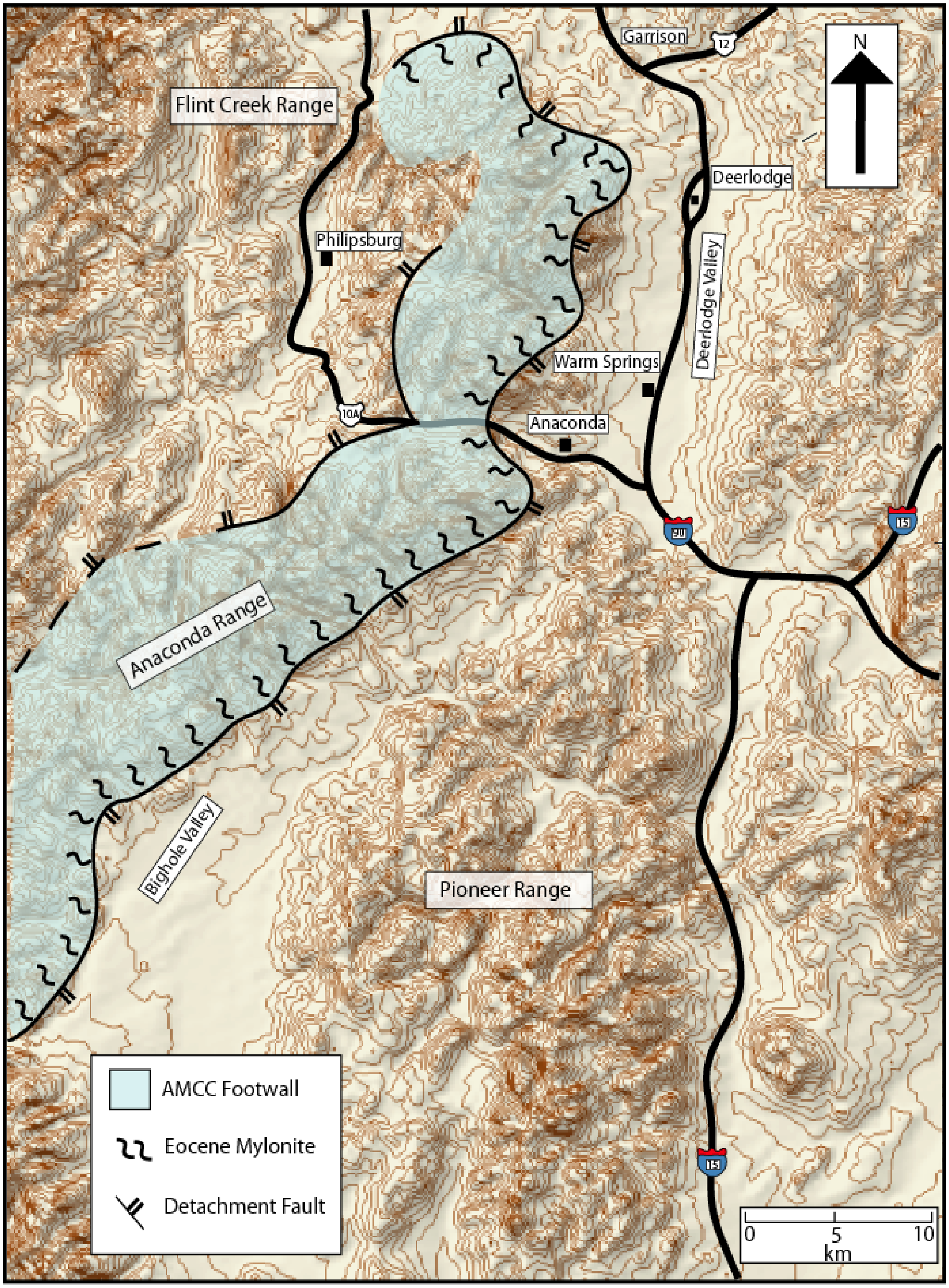

Figure 1-1. Footwall of the Anaconda metamorphic core complex exposed in the Anaconda and Flint Creek ranges. Figure modified from Grice, 2006.

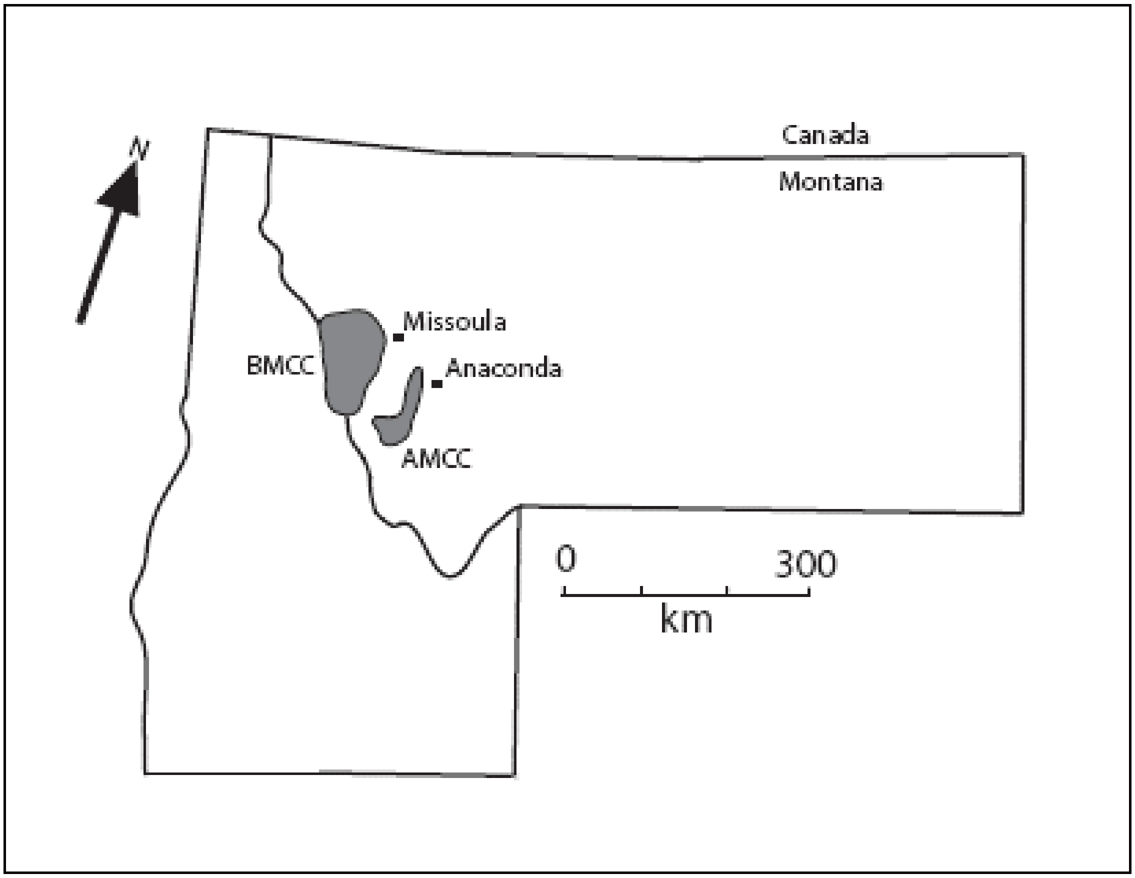

Figure 1-2. Illustration showing the location of Anaconda and Bitterroot metamorphic core complexes in southwestern Montana and northern Idaho. BMCC and AMCC refer to the Bitterroot and Anaconda metamorphic core complexes, respectively.

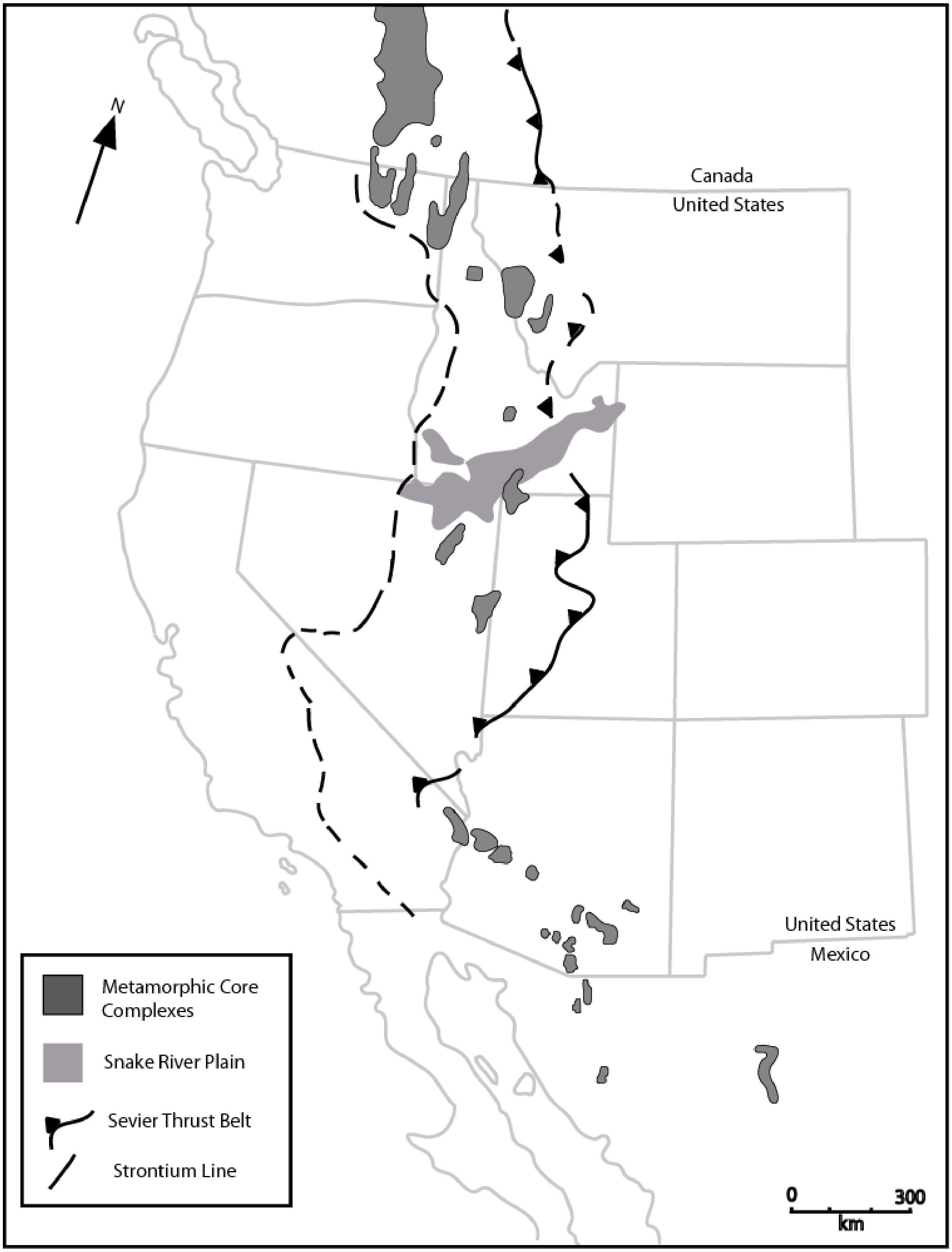

Figure 1-3. Chain of North American Cordilleran metamorphic core complexes from northern Mexico to southern Canada. Complexes north of the Snake River Plain contain similar characteristics to the Anaconda metamorphic core complex. Figure after Coney, 1980.

CHAPTER 2

CORDILLERAN METAMORPHIC CORE COMPLEXES

Metamorphic core complexes occur in orogenic belts worldwide and form during extensional tectonics following convergence, providing a window into the middle to lower levels of the crust that exposes the deeper levels of orogens. These features are quite familiar to geologists, as the surficial geology is well-characterized, however models for their formation remain equivocal. The Cordilleran metamorphic core complexes are a group of domal, anomalously deformed uplifts occurring in a narrow belt from northern Mexico to southern Canada (Davis and Coney, 1979; Coney, 1980; Coney, 1984) (Figure 1-3). Despite the fact that these features form a linear pattern and show striking similarities to one another, it is evident that there is a discontinuity across the Snake River Plain in which metamorphic core complexes to the north are older and most likely formed from different tectonic processes than complexes south of the Snake River Plain (Crittenden et al., 1978). These complexes are characterized by an older metamorphic-plutonic basement (footwall) terrane with an attenuated unmetamorphosed cover (hanging wall) that is cut by numerous younger-on-older faults (Misch, 1960; Armstrong, 1972; Coney, 1974; Coney, 1980a). Basement terranes generally have a low-dipping foliation encasing a mineral lineation that can contain boudins, folds, and ductile faults (Davis, 1977; Coney, 1979; Coney, 1980a). Metamorphic grade of the footwall often reaches upper amphibolite facies (Coney, 1980a). Separating the footwall from the hanging wall is a detachment fault that is generally characterized by a ~500-2000-m-wide mylonite zone (Coney, 1980a; Foster et al., 2007). Formations with in the hanging wall can be tectonically thinned or absent but are generally in normal stratigraphic succession (Davis and Coney, 1979).

The primary metamorphic event affecting footwall rocks in the Cordilleran MCCs occurred during the Cretaceous. Subsequent decompression occurred during Tertiary exhumation (Table 2-1). The Cordilleran hinterland has a strong Tertiary overprint that

Table 2-1. Summary of P-T-t data for selected North American core complexes.

Core Complex	Max P (kbar)	Max T (°C)	t – M2 meta. (Ma)	t – extension (Ma)	Width (km)	References
Shuswap	6-9[1]	620-820[1]	160-60[1]	60-48[1, 2]	†	[1]Vanderhaeghe et al., 2003; [2]Lorencak et al., 2001
Priest River	7-10[3,4]	770-930[3,4]	72[5]; 86[6]	55-43[3]	20-30[7] (Spokane Dome)	[3]Doughty & Price, 1999; [4]Rhodes, 1986; [5]Doughty et al., 1998; [6]Doughty & Chamberlain, 2004;[7]Foster et al., 2007
Clearwater	8-11[7,8]	575-750[7,8]	77-54[7]118[9]	52-46[7,10]	~35[7]	[8]Grover et al. 1992; [9]Vervoort et al., 2005; [10]Burmester et al., 2004
Bitterroot	6-8[11,12]	600-750[11,12]	64-56[11]; 80-53[12]	53-39[12-17]	30-35[87]	[11]House et al., 1997; [12]Foster et al., 2001; [13]Chase et al., 1983; [14]Garmezy, 1983; [15]Hodges & Applegate, 1993; [16]House & Hodges, 1994; [17]Foster & Fanning, 1997
Anaconda	3-4[18,19] 3.3-5.3[20]	650-750[18,19]; 600-650[20]	79 [19]	53-39[19]	15-20[7]	[18]Grice et al., 2005; [19] Grice, 2006; [20] *this study*
Pioneer	3.5[21]	680[21]	79[21]	54-45[21]	15-17[21]	[21]Silverberg, 1990.

† Shuswap complex is extremely wide. Gneiss domes within the complex average ~60 km in width.

was recognized by young K-Ar ages in basement rocks, listric normal faults, and decollement zones of the unmetamorphosed cover (Coney, 1980). This tectonic overprint proved to be extensional; it followed Sevier-Laramide compressional thrusting, preceded Basin and Range faulting, and was simultaneous with widespread ignimbrite eruptions (Davis and Coney, 1979; Coney, 1980). These Tertiary age features can have deformation of basement terranes that date back to Proterozoic times, making it difficult to decipher their history (Coney, 1980a). Granitic plutons are common in basement terranes along with pegmatitic, migmatitic, and other late-stage differentiates and leucocratic phases (Crittenden et al., 1978; Coney, 1980a). These plutonic bodies usually form sheet-like or lensoid masses that are sub-parallel to foliation but also cross it (Coney, 1980).

The formation of the Cordilleran MCCs and their relationship to overlapping magmatism is still equivocal, but gravitational collapse is currently the most accepted hypothesis. Coney and Harms (1984) put forth the gravitational spreading theory for the formation of the Cordilleran core complexes, stating that these features formed due to crustal thickening along the Cordilleran hinterland during the Mesozoic followed by Cenozoic extension. Deep seated extension transpired due to the gravitationally unstable tectonically thickened crust within the Sevier orogenic belt (O'Neill et al., 2004). Liu (2001) argues that even though at isostatic equilibrium a thickened crust is dynamically unstable and will collapse. Post-orogenic extension only occurs when the lithosphere is sufficiently weakened by thermal processes associated with orogenesis. Ductile spreading within the lower crust is a mechanism that can account for both extension and exhumation of core complexes and associated plutonism (Liu, 2001). The major silicic

Cordilleran volcanism in the mid-Tertiary is not accounted for in this mechanism, as major mantle upwelling is the likely source for the voluminous eruptions (Liu, 2001). The numerous MCCs within the thickened Cordillera are evidence for the gravitational collapse model (Liu, 2001; Coney and Harms, 1984).

Although gravitational collapse seems to be the forerunner theory for core complex development and the features within them, other hypothesis are still being tested. Gneiss domes in orogens could be the result of diapiric upwelling in association with thinning of previously thickened crust (Whitney and Teyssier, 2002). Evidence for decompression is highly evident in the Thor-Odin dome in the Shuswap metamorphic core complex, British Columbia, Canada, supporting the theory that decompression drives partial melting (Whitney and Teyssier, 2002). Ductile thinning, causing decompression, and buoyant rise of deep, hot orogenic crust may generate a positive feedback that drives the upward movement and partial melting of the crust (Whitney and Teyssier, 2002). Gneiss domes may be diapirs that are emplaced high enough into the crust to retain their domal shapes, as seen in North American Cordilleran metamorphic core complexes (Whitney and Teyssier, 2002). This process may account for the rapid cooling that follows decompression as diapirism is an efficient mechanism of heat and mass transfer in the crust (Whitney and Teyssier, 2002).

CHAPTER 3

REGIONAL BACKGROUND

Precambrian

The Prichard (also known as the Greyson) Formation is stratigraphically the lowest unit deposited in the Belt basin during Precambrian time (Figure 3-1). The Prichard Formation is a dark-greenish-grey, laminated argillite and silty argillite, containing beds, less than 5-cm-thick, of white to tan very fine grained sandstone and siltstone (USGS, 2005). Sediments are of marine influence and were deposited in an intertidal to subtidal zone of a shallow, flat shelf (Bloomfield, 1983).

Age	Group	Formation	Description
Middle Proterozoic	Missoula	Garnet Range	Fine grained, green-gray quartzite with interbedded argillite.
		McNamara	Fine-medium grained quartzites characterized by trough crossbeds and flat lamination capped by thin argillite beds.
		Bonner	Highly recrystallized quartzite with beds of schist and phyllite.
		Mt. Shields	Phyllites, quartzites, with minor schists.
		Shepard Snowslip	Quartzites, phyllites, and calc-silicates.
	Middle Belt Carbonate	Wallace	Fine grained quartzites. Greenish, diopside rich, calc-silicate gneiss. Marble and minor schist.
	Ravalli	St Regis	Small zone of kyanite bearing pelitic schists. Fine-medium grained, laminated, gray quartzites with thin beds of phyllites and
		Revett	
		Burke	
	Lower Belt	Prichard	Reddish-brown weathering biotite-muscovite schists containing variable amounts of quartz, sillimanite, feldspar, and garnet. Discordant lenses of leucosome present.

Figure 3-1. Stratigraphic column of lower Belt Supergroup Formations found within the Anaconda metamorphic core complex and surrounding areas. Formation descriptions after Lonn et al., 2003.

Lying stratigraphically above the Prichard Formation are the Ravalli Group, Snowslip Formation, and Shepard Formation (Lonn et al., 2003). The Ravalli Group sediments are composed of fine- to medium-grained quartzites separated by pelitic layers (Lonn et al., 2003). The Snowslip Formation is composed of red sand and clay with abundant ripples and mud cracks (Lonn et al., 2003). Dolomitic siltite-argillite laminae are common near the base of the Snowslip Formation with siltite and quartzite increasing up-section (Lonn et al., 2003). Green, dolomitic siltite and argillite layers in microlaminae and couplets are characteristic of the Shepard Formation (Lonn et al., 2003). These formations are present in both the Flint Creek and Anaconda-Pintlar ranges (Figure 3-2).

Mesozoic

Convergence began in the Mesozoic along the western margin of Laurentia with the Sevier orogeny, which resulted in thrusting within the back-arc region. The Sevier belt, which developed during Jurassic to Late Cretaceous time, forms a major structural element from southern California to northern Canada (Burchfield et al., 1992). Thrust faults associated with the Sevier belt have thin-skinned geometries, eastward direction of transport, and young east to west. In western Montana, Sevier thrust faults are typically controlled by bedding of Belt basin rocks (Burchfield et al., 1992). Thin-skinned Sevier-style thrusting was thus superimposed on the Belt basin resulting in a thicker package of sediments in the west and a thinner Paleozoic and Mesozoic package to the east (Foster, 2000). In the Anaconda-Pintlar and Flint Creek ranges, Sevier thrusts carried Proterozoic and Phanerozoic rocks eastward (O’Neill et al., 2004). Compression during the Sevier

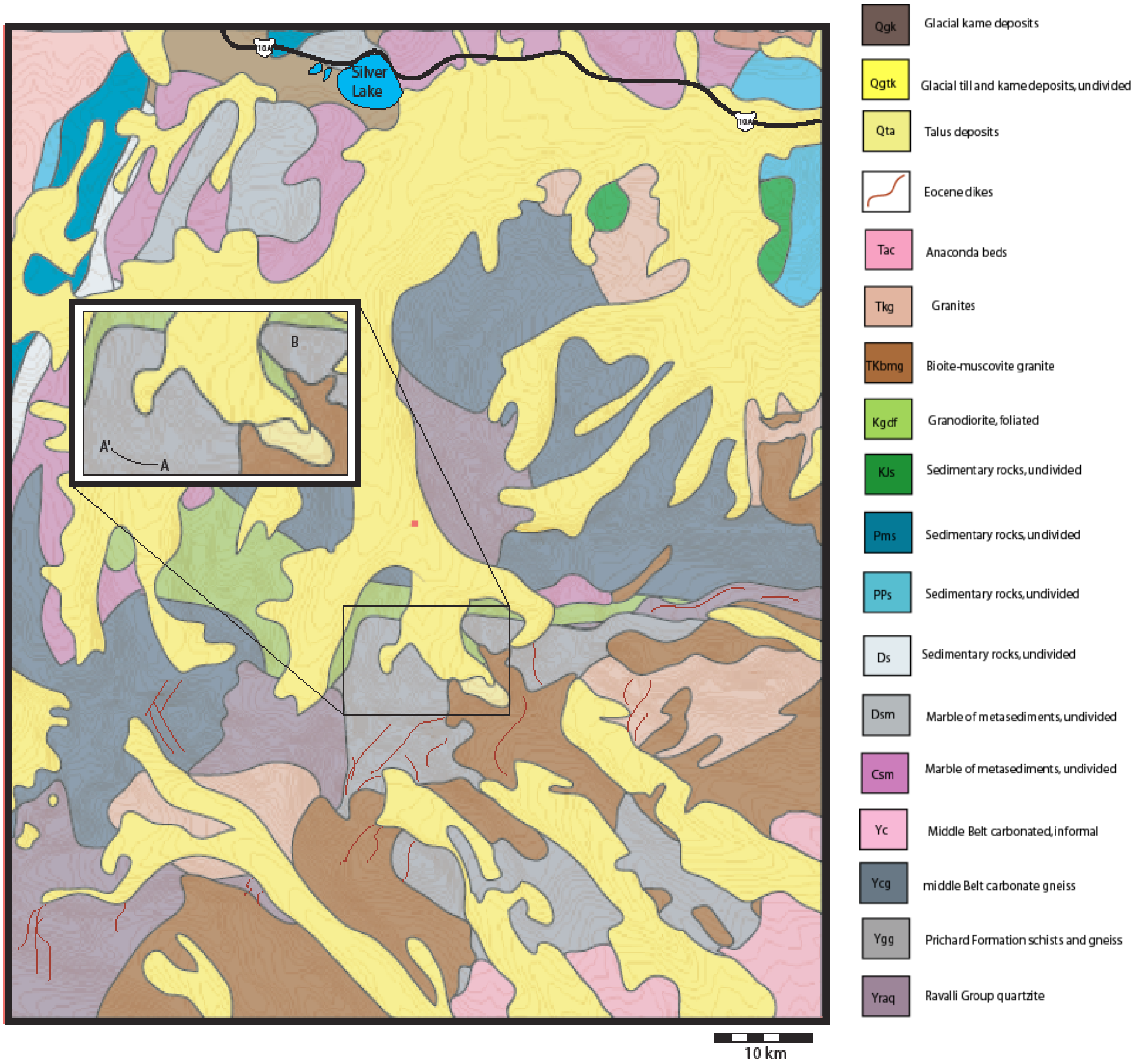

Figure 3-2. Geologic map of the Anaconda MCC footwall in vicinity of collected samples. Enlarge area A-A' shows traverse of samples collected in this study. Point B shows approximate collection site of ME-231 of Grice, 2006. ME-231 is a sample of the meta-Greyson formation taken from the Lake of the Isle shear zone that was used for thernobarometry. Thermobarometry results from ME-231 is used as a comparison from results in this study. Figure after Lonn et al., 2003.

orogeny resulted in thickening of the lithosphere. The tectonic evolution during the Sevier is summarized by three major events: 1) Late Cretaceous growth of the tectonically and magmatically thickened wedge, 2) Late Cretaceous extensional collapse of the hinterland in conjunction with foreland thrusting, and 3) Eocene extension (Kalakay, 2004a).

The Cordilleran magmatic arc is a >4000-km-long belt of granitoid intrusions formed as a consequence of the eastward dipping subduction zone along the western margin of North America from late Triassic to late Cretaceous time (DeCelles, 2004). The Idaho batholith formed during the Mesozoic and early Tertiary and intruded Precambrian crust (metasedimentary rocks of the Belt Supergroup) (Foster et al., 2001). Three major overlapping 'provinces' occurred during the Cretaceous to Tertiary east of the Idaho-Bitterroot batholith, making up the foreland of the Sevier orogen: Sevier style thin-skinned fold and thrust belt, a belt of silicic extrusive and intrusive rocks, and Laramide-style basement cored uplifts (Foster, 2001). The Sevier orogenic wedge grew during an overlap between arc magmatism and crustal shortening (Kalakay et al., 2004a). It developed large basement culminations between ~80-70 Ma, which was replaced by silicic plutons, including the Boulder batholith, that cut the fold and thrust belt at all crustal levels (Kalakay, 2003). This resulted in 50-60 km thick hinterland culminations by ~70 Ma (Kalakay et al., 2004a). The Boulder, Pioneer and Philipsburg batholiths, along with smaller plutons, occur 100-80 km east of the Idaho-Bitterroot batholith forming a belt of Late Cretaceous magmatic rocks that were intruded broadly contemporaneously around ~85 and 65 Ma (Foster et al., 2001; Liu, 2001). Thrusting in western Montana was primarily active between ~80 and 50 Ma (Foster et al., 2001). Late Cretaceous plutons were emplaced along thrust fault ramps within the Anaconda metamorphic core complex (Kalakay et al., 2001; Grice, 2006).

Latest Cretaceous time saw major changes in the deformation of the lithosphere as a result of an increase in rate of convergence of the western margin of the North American plate and changes in subduction geometry (Burchfield et al., 1992). The

Laramide orogeny is expressed as contractional deformation in the former cratonal areas east of the fold and thrust belt (Burchfield et al., 1992). Significant shortening occurred (≥ 200 km) in the northern part of western Montana and southern Canada in conjunction with the eastward migration of the Cordilleran magmatic arc until Paleogene time (Lageson et al., 2001). In Montana, Laramide structures strike obliquely to the fold and thrust belt and are associated with NW-striking left-lateral faults.

Quantitative thermobarometry of metamorphic rocks together with U-Pb dating of zircon and monazite within the Bitterroot and Clearwater core complexes, define three regional deformational events: crustal shortening 100-80 Ma, magmatism and crustal thickening at 64-56 Ma, and high-temperature isothermal decompression at 56-48 Ma (House, 1997). Large scale extension, north of the Snake River plain, is evidenced by detachment faults in MCCs in which extension generally youngs to the south. The Shuswap MCC detachment was largely active from ~60-48 Ma (Vanderhaeghe et al., 2003). The onset of extension in the Priest River MCC occurred from ~55-43 Ma (Doughty and Price, 1999). Both the detachments of the Bitterroot and Anaconda MCCs accommodated large scale crustal extension from ~53-39 (Hodges and Applegate, 1993; House and Hodges, 1994; Foster and Fanning, 1997; Foster et al., 2001; Grice, 2006). Initial collapse of the orogen in the Bitterroot MCC coincides with mid-crustal granitic intrusions of the about the same age ~ 52-50 Ma (Foster et al., 2001). Metamorphosed pelitic rocks in the Snow Peak area (Clearwater MCC), northern Idaho, record two episodes of regional deformation. The second metamorphic event resulted in replacement or reequilibration of the original metamorphic assemblage producing a peak assemblage of kyanite + garnet + biotite + muscovite + quartz + plagioclase + ilmenite + graphite

(Lang and Rice, 1985). Early inclusion assemblages in garnet cores at Boehls Butte (Clearwater MCC) indicate *P-T* conditions around 500°C and 5-6 kbars (House, 1997). Thermobarometry of rocks at Snow Peak, northwestern border of the Bitterroot lobe of the Idaho batholith, define a clockwise *P-T* path that is consistent with published data from the Bitterroot metamorphic core complex (MCC) footwall, which indicates M2 peak conditions of 650-750°C at 6-8 kbars (Table 2-1) (Foster et al., 2007; House, 1997). The loop is interpreted to represent regional thickening associated with east verging thrusting from the Sevier and Laramide orogenies (House, 1997).

Cenozoic

Following crustal shortening and mountain building in the North American Cordilleran, extension and widespread magmatism ensued (Liu, 2001). The Lewis and Clark fault zone acted as a sinistral transpressional shear zone during thrusting, which occurred from the Cretaceous to the Paleogene (Foster et al., 2007). The Lewis and Clark line (LCL) divides major thrust slabs within the Cordilleran fold and thrust belt (Sears and Hendrix, 2004). Sears and Hendrix (2004) concluded that the LCL represents a rotational shear zone that supplied the relationship between clockwise rotating thrust slabs that formed the Alberta and Helena salients during Cretaceous and Paleocene time.

In the Eocene, the LCL was reactivated as a right-lateral to accommodate for large scale extension as core complexes were exhumed (Foster et al., 2007). North of the LCL, core complexes were exhumed by paired east-west detachment faults (e.g. Priest River); while to the south the Bitterroot and Anaconda MCCs were exhumed by a single east dipping detachment fault (Figure 3-3) (Grice, 2006; Foster et al., 2007).

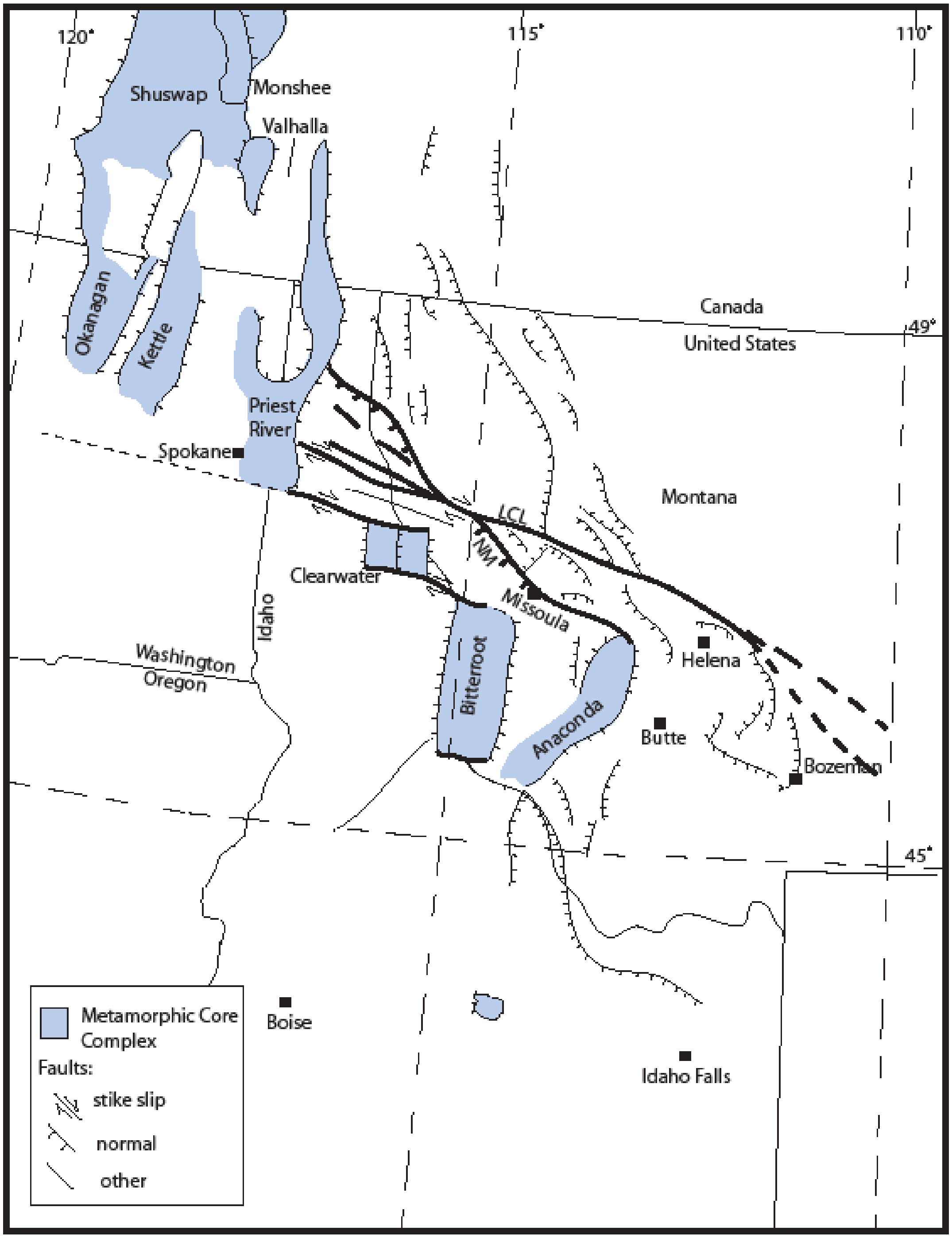

Figure 3-3. Schematic of metamorphic core complexes north of the Snake River Plain in relationship to the Lewis and Clark fault zone. NM refers to the Ninemile fault. Figure after Foster et al., 2007.

Decompression of the thickened lithosphere from the Sevier and Laramide orogenies was accommodated by detachment systems in MCCs. Extension in the Priest River MCC occurred from ~55-43 Ma (Price and Doughty, 1999) and in the Bitterroot and Anaconda MCCs from ~53-39 (Hodges and Applegate, 1993; House and Hodges, 1994; Foster and Fanning, 1997, Foster et al., 2001; Grice, 2006). Oblique convergence between the Kula, Farallon, North American, and Pacific plates starting at ~53 Ma was responsible for the dextral transtension during Eocene time in the Cordillera (Foster et al., 2007; Madsen et al., 2006). The Priest River, Clearwater, Bitterroot, and Anaconda MCCs are kinematically linked by dextral transtension through the LCL (Foster and Kalakay, 2003). Transpiring during the same time ~53-45 Ma was widespread Challis-Colville-Kamloops volcanics (Foster et al., 2007; Madsen et al., 2006).

CHAPTER 4

Anaconda Metamorphic Core Complex

Introduction

The Anaconda extensional terrane lies in western Montana and contains exhumed exposures from three different crustal levels (Wolfe, 2003). The deepest rocks are amphibolite grade pelitic schists and para and orthogneisses that are cut by synextensional granites. Boudinage, rootless isoclinal folds, and concentric folds indicate high strain in these rocks (Wolfe, 2003). A greenschist mylonite zone overlies lower level rocks and contains concentric folds whose hinges are sub-parallel to stretching lineations (Wolfe, 2003). Unmetamorphosed volcanoclastics cap the mylonite zone (Figure 4-1)

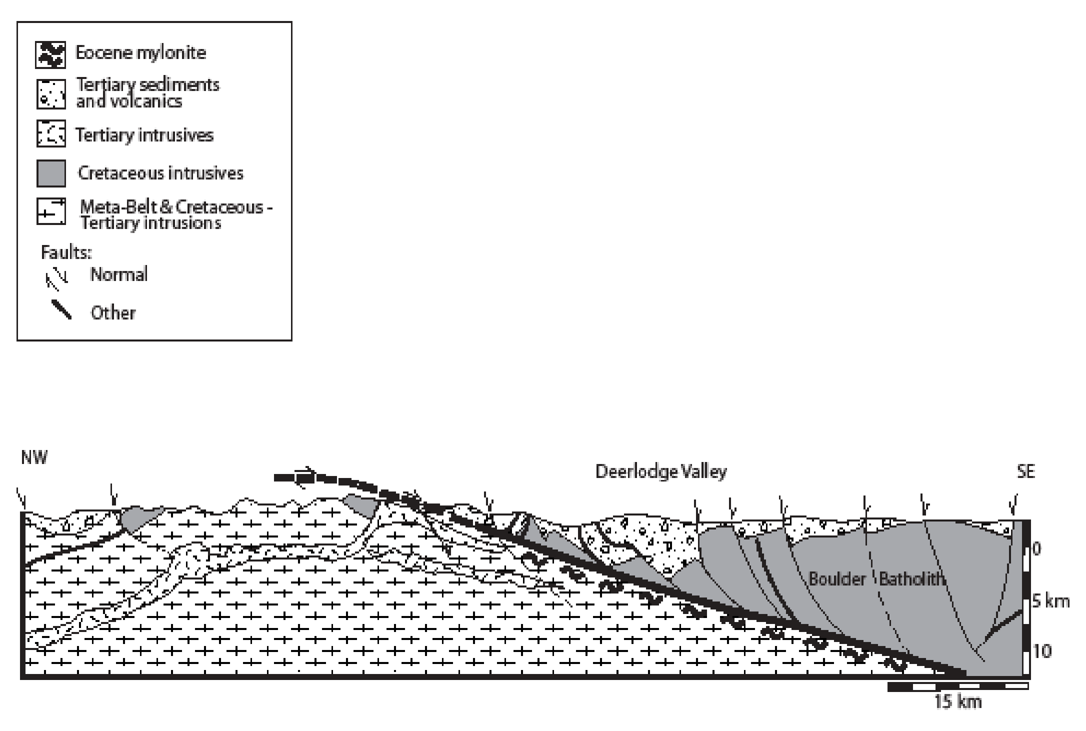

Figure 4-1. Cross section of the Anaconda metamorphic core complex, with Eocene mylonite beneath the detachment fault. Figure modified from Grice, 2006.

(Foster et al, 2007; Grice, 2006; Grice et al., 2005). The Eocene Anaconda detachment fault translated the Boulder batholith tens of kilometers eastward, exposing the deformed, metamorphosed footwall that contains evidence of crustal anatexis (Kalakay et al., 2004). These rocks show high grade metamorphic assemblages due to dynamic and thermal processes from thrusting; some also contain overprint polyphase extensional fabrics that post-date hinterland thickening (Kalakay et al., 2004). Folding is thought to have occurred during extension as well as during Sevier contractional thrusting as is evidenced by dike emplacement and corresponding alignment of fold hinge orientation and stretching lineations (Wolfe, 2003). Pelitic schists within this study area contain assemblages that are not overprinted by subsequent extensional fabrics.

The AMCC is superimposed on a plutonically thickened tectonic culmination within the Sevier orogenic belt which is underlain by Archean crystalline basement and metasediments of the Belt Supergroup (O'Neill, 2004). Its structural aspect is that of a segmented, elongate antiform that is northeast trending in the Anaconda range and north-northeast trending in the Flint Creek range separated by the Warm Springs synform that is east trending and passes beneath the town of Anaconda (O'Neill, 2004). Decollement style thrust faults, folds, and Late Cretaceous to Paleogene small to moderate size epizonal plutons are characteristic of the area (O'Neill, 2004). Shallow plutons within the AMCC overlap in time with both crustal thickening and extension in this part of the Sevier orogen (Foster, 2000).

Footwall

Rocks in the core of the complex, with exposures in the Anaconda and Flint Creek ranges, are mainly metamorphosed Mesoproterozoic Belt quartzites, argillites, and pelites that correspond to the Missoula Group, Helena Formation, Ravalli Group, and Prichard Formation (Figure 3-1) (Foster et al., 2007). Late Cretaceous (~73 Ma) plutonic rocks intrude older Belt metasedimentary rocks in the core of the complex (O'Neill, 2004). High structural levels expose rocks that contain older deformational fabrics that are overprinted by shallow dipping mylonitic fabrics with an east southeast and west northwest mineral lineation (O'Neill, 2004). Mineral lineations and foliations decrease in intensity with distance beneath the detachment (O'Neill, 2004). Early kyanite-bearing assemblages are replaced by pseudomorphs of fibrolitic sillimanite zones with evidence that supports partial melting in high-temperature sillimanite zones (Foster et al., 2007). Partial melting in footwall rocks occurs as discordant lenses. Initial thermobarometry from garnet-bearing metapelites within the migmatite zone indicate peak metamorphism around 650-750°C at 3-4 kbars (Grice, 2006; Grice et al., 2005; Foster et al., 2007) that is inferred to be Cretaceous in age as indicated by 79 Ma hornblende ^{40}Ar/ ^{39}Ar dates on metadiorite and Cretaceous granodiorite that intrude the migmatitic zone (Foster et al., 2007).

Major structures within the footwall include folds and low angle thrust faults that are related to shortening during compression (Grice, 2006; Sears and Hendrix, 2004). The Georgetown thrust is the largest of the thrust faults and places middle Proterozoic Belt rocks over Paleozoic and Mesozoic sedimentary rocks (Grice, 2006; Lonn et al., 2003). This folded thrust defines the eastern edge of the large allochthon known as the Sapphire tectonic block that extends west into the Bitterroot detachment fault (Grice, 2006; Lonn et al., 2003). The Georgetown thrust has >7000 m of stratigraphic offset and marks the western boundary of the AMCC footwall from the central Anaconda-Pintlar range to the northern Flint Creek range (Grice, 2006; O'Neill et al., 2004). Younger normal faults and brecciation related to ongoing extension continue to cut footwall rocks (O'Neill et al., 2004).

Detachment Fault

Emmons and Calkins (1913) were first to note that the Anaconda detachment fault was like the "great Bitterroot fault" (Foster et al., 2007*;* Lonn et al., 2003; Grice, 2006). The 100-km-long low angle normal fault of the AMCC is distinguished by a 300-500-m-thick greenschist facies mylonitic shear zone that shows top-to-the-east-southeast displacement (Foster et al., 2007; Grice et al., 2005; O'Neill et al., 2004). This sinuous fault zone cuts the southeast margin of the Anaconda range in the Big Hole Valley, trends northeastward through the town of Anaconda, and northward toward the east side of the Flint Creek range (O'Neill et al., 2004). The detachment is not continuous as it is variably cut by younger listric normal faults, has been removed by erosion, and is covered by hanging wall slivers and talus (Foster et al., 2007). Gently southeast-dipping low-angle Tertiary normal faults place Mesoproterozoic through Paleozoic sedimentary rocks on Tertiary granitic rocks or on sedimentary rocks older than the overlying detached rocks (O'Neill, 2004). The northeastern edge of the detachment trends into a steeply-dipping complex zone of ductile deformation that appears to merge with the Ninemile fault, an important element of the east-west trending Lewis and Clark line (O'Neill et al., 2004;

Foster et al., 2007; Grice, 2006; Yin and Oertel, 1995). The Anaconda detachment is separated from the Bitterroot detachment by a zone of fractured and faulted hanging wall rocks which was intruded by a northeast trending Eocene dike swarm; this may have accommodated differential extension between the two detachment systems (Foster et al., 2007).

The detachment fault zone dips gently east along the east front of the Flint Creek and Anaconda ranges and gently west on the western front, defining the two northeast trending antiforms (O'Neill et al., 2004; Foster et al., 2007; Grice, 2006). In the Anaconda and northern Flint Creek range most of the upper Missoula Group Belt rocks are missing, indicating that stratigraphic offset exceeds several kilometers at the detachment (O'Neill et al., 2004). East of the core complex, the fault surface is curvilinear as it gently dips east, south, and southeast while to the west of the Flint Creek range it dips gently west but is locally steep to vertical (O'Neill et al., 2004). The gentle east dip is supported by industry exploration wells in the Deerlodge basin (McLeod, 1987; Grice, 2006; Foster et al., 2007).

The onset of extension in the AMCC is constrained to ~53 Ma and lasted until at least 39 Ma based on cooling ages obtained from two-mica and biotite granite and granodiorite plutons in the ACC lower plate rocks, using $^{40}Ar/^{39}Ar$ thermochronology and $^{206}Pb/^{238}U$ zircon crystallization ages (Grice, 2006; Foster et al., 2007). A lateral cooling gradient was observed within micas, validating top-to-the ESE direct unroofing of the lower plate (Grice, 2006). Mylonites within the shear zone contain both mesoscopic and microscopic fabrics with kinematic indicators that include porphyroblasts, rolled porphyroblasts, pinch and swell structures and asymmetric mica fish that imply eastward tectonic transport of overlying rocks (O'Neill, 2004). Differential strain is evident throughout the mylonite zone, as 1-2-m-thick ultramylonite zones are separated by 5-15-m-wide mylonite and protomylonite zones (Foster et al., 2007*;* Grice, 2006). In the footwall, near Lake of the Isle shear zone (LISZ), mica ^{40}Ar/ ^{39}Ar cooling ages also indicate the geometry of the detachment fault to a steeply dipping listric normal fault at 54-70° within the upper brittle crust which shallows out in the middle crust to 7-12° (Grice, 2006). Around 25 km of Eocene horizontal movement occurred along this fault as is signified by the reconstruction of Late Cretaceous granodiorite plutons within the detached hanging wall (Grice, 2006). The mylonite zone transitioned from plastic to brittle behavior as is indicated by broken feldspar porphyroclasts encircled in a matrix of plastically deformed quartz ribbons (Pauli et al., 2003). Relative age of the fault suggest that it youngs west to east (Foster et al., 2007).

Hanging Wall

The hanging wall consists mainly of unmetamorphosed cover rocks of the Lowland Creek volcanic sequence and Mesoproterozoic though Mesozoic sediments that are variably tilted within fault bound basins (Grice et al., 2004; Grice et al., 2005; Lonn et al., 2004). Stratigraphically lower basins are steeply dipping (50-60°) toward the detachment (Foster et al., 2007; Kalakay et al., 2003; O'Neill et al., 2004). Higher stratigraphic basins are more moderately dipping (25-0°) and contain mainly volcanic flows, tuffs, and volcanoclastics of the 53-48 Ma Lowland Creek volcanic sequence (Foster et al., 2007). To the west, flank sediments show less cataclastic and stratigraphic disturbance but show intense amounts of stratigraphic attenuation (Lonn et al., 2004).

Cutting strongly broken and shattered hanging wall sediments of the AMCC are normal and strike-slip faults of small displacement (Lonn et al., 2004). In the eastern part of the core complex, these rocks are cut by numerous east-dipping listric normal faults that merge with the underlying detachment fault (Lonn et al., 2004). Syntectonic conglomeritic units overlie upper plate rocks of the core complex and are locally brittle, fractured, broken, and extended (Lonn et al., 2004).

Lake of the Isle Shear Zone

The Lake of the Isle shear zone lies within the AMCC footwall and contains high temperature, extremely attenuated, mid-crustal Proterozoic and Cambrian rocks that are cut by Eocene faults (Grice et al., 2004a). This is a ductile, sinuous shear zone that lies in the northeastern Anaconda-Pintlar range (Grice, 2006). Preliminary thermobarometry from Lake of the Isle shear zone (LISZ), structurally beneath the detachment, indicate upper amphibolite to lower granulite facies metamorphism (Grice, 2006). This shear zone is overprinted by the Storm Lake stock which gives a biotite $^{40}Ar/^{39}Ar$ of 79 ± 1.1 Ma and deforms a late Cretaceous quartz diorite sill, indicating ductile attenuation in the footwall preceded the main detachment normal faulting by >20 Ma (Grice et al., 2004a; Grice, 2006). The LISZ contains kyanite-bearing assemblages that are overprinted by high-temperature, low-pressure sillimanite and andalusite assemblages (Kalakay et al., 2004a). Shear zone lineations plunge gently in concurrence with younger over older stratigraphic relationships (Kalakay et al., 2004). Preliminary geothermobarometry of metapelites from the Lake of the Isle shear zone indicates pressures and temperatures around 3.8 ± 1.8 kbar and 657 ± 176°C (Grice, 2006).

CHAPTER 5

METHODS

Sample Preparation

Pelitic schists were collected from Lake of the Isle shear zone (LISZ) located in the Mount Evans 1: 24,000 quadrangle just west of Anaconda, Montana. Ongoing studies of the AMCC by Professor Tom Kalakay at Rocky Mountain College, Billings, Montana concluded that pelitic schists at this location (E 033031 N 5103478) would result in the most suitable metamorphic assemblages for examination.

A total of thirty thin sections from twenty-two hand samples were prepared for petrographic observations. Billets were cut, from fresh surfaces, as a representative section of each hand sample. More than one billet was produced if a single billet could not represent the hand sample as a whole. Spectrum Petrographics, Inc. (www.petrography.com) was used to produce thin sections. Thin sections whose hand samples contained visible garnets were finished with a microprobe polish while all other samples were finished with a standard glass cover slip. Composition of garnet is a sensitive monitor of metamorphic *P-T* conditions which may be determined by electron microprobe analysis (Spear, 1993), which this study intended to utilize.

Equilibrium assemblages were determined by textural relationships of minerals. Nine representative samples were analyzed for major element chemistry by X-ray fluorescence spectrometry (XRF).

In order to ensure accurate whole rock geochemical data, grinding them into a fine powder is the best method of obtaining a representative sample (Van Grieken and Markowicz, 1993). Hand samples were cut into roughly 1"x 2" x ½" squares for pulverization in the alumina ceramic shatterbox housed at University of Montana. Only fresh surfaces from hand samples were used. Surfaces were polished with 600 grit silicon carbide to assure no metal fragments from the rock-saw saw blade adhered to the rock Pure silica sand was run in the shatterbox between each rock sample to ensure contamination did not occur. Three grams of each sample was weighed out and sent to Activation Laboratories Ltd. Ancaster, Ontario for XRF analysis. Here the powders were fused and cast as disks in the final preparation for analysis.

Pseudosections

Introduction

The whole rock composition of sample MTAF13 (Figure 5-1; Table 5-1) was used in conjunction with phase equilibria computer modeling programs to quantitatively determine the *P-T* evolution of the AMCC through the construction of pseudosections, which are mineral assemblage diagrams for a specific bulk composition. Sample MTAF13 was chosen for modeling as it contains the most garnet and has a mineral assemblage that appears to be in equilibrium from petrographic analyses. Although melt is present in the rock, it comprises a small proportion of it. It is therefore assumed that the rock equilibrated in a closed system in which metasomatism and melt loss did not occur. Forward modeling from the pseudosection approach provides a quantitative method for interpreting the *P-T* evolution of a sample, as this approach accounts for both bulk composition and multivariant equilibria (Baldwin et al., 2005). These diagrams depict the stability fields of mineral assemblages in *P-T* space so that the complete prograde

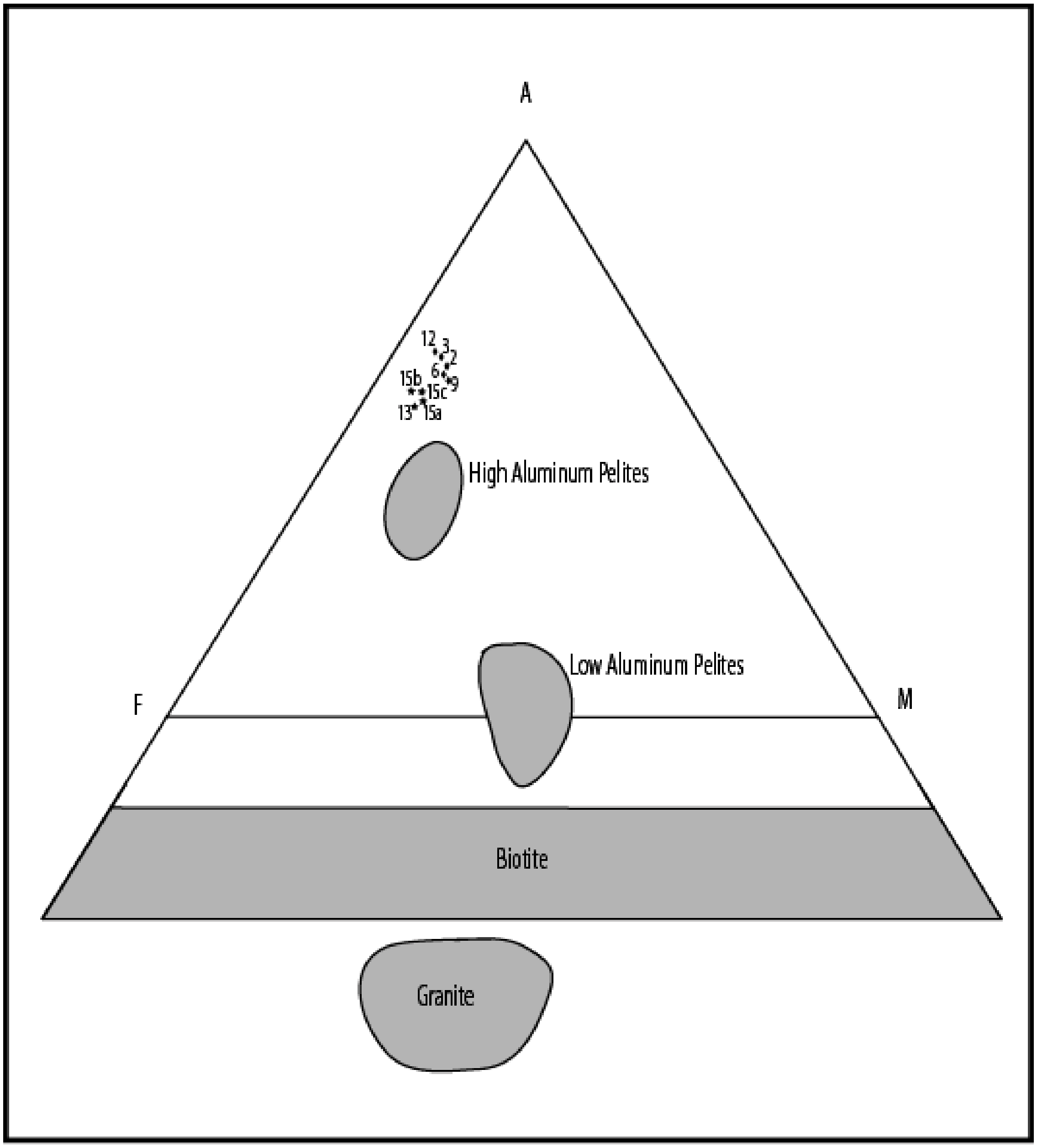

Figure 5-1. AFM projection showing whole rock bulk composition of metapelites from the Anaconda metamorphic core complex footwall. Garnet bearing samples are starred. Numbers next to samples localities correspond to XRF samples in table 5-1. High aluminum, low aluminum, and granite zones are after Spear, 1993.

Table 5-1. XRF results from meta-pelites in the Anaconda metamorphic core complex footwall.

Component	SiO2	Al2O3	Fe2O3	MnO	MgO	CaO	Na2O	K2O	TiO2	P2O5	Cr2O3	LOI	Total
Detection Limit	0.01	0.01	0.01	0.001	0.01	0.01	0.01	0.01	0.01	0.01	0.01	0.01	0.01
MTA 12	55.42	26.23	9.47	0.039	1.71	0.17	0.63	3.84	1.15	0.04	< 0.01	1.43	100.1
MTA 3	61.44	21.16	7.81	0.063	1.67	0.29	0.46	3.94	0.88	0.16	< 0.01	2.17	100
MTA 2	64.31	19.71	6.82	0.044	1.48	0.46	0.64	3.06	0.72	0.15	< 0.01	1.96	99.34
MTAF 13	57.64	21.39	11.37	0.178	1.88	0.73	0.97	3.36	0.9	0.13	< 0.01	1.17	99.71
MTA 9	62.37	19.26	8.02	0.048	1.85	1.26	1.86	3.26	1	0.06	< 0.01	1.57	100.6
MTA 6	67.81	16.51	6.66	0.04	1.45	1.44	1.89	2.2	0.86	0.04	< 0.01	1.22	100.1
MTA 15a	56.15	22.85	11.97	0.115	1.76	0.34	0.64	3.78	0.97	0.11	< 0.01	1.44	100.1
MTA 15b	58.89	22.28	10.93	0.073	1.74	0.2	0.48	3.25	0.93	0.07	< 0.01	1.27	100.1
MTA 15c	56.94	21.83	12.39	0.162	1.7	0.31	0.51	3.66	0.86	0.15	< 0.01	1.18	99.68

through retrograde evolution may be determined (Vance, 1998). Pseudosections are especially useful for pelitic rocks as minerals in pelites are sensitive to *P-T* changes, allowing formation of diagnostic mineral assemblages. Pseudosections are preferred over conventional geothermobarometry as it allows for a more robust evaluation of chemical and mineralogical relationships in *P-T* space (Vance and Mahar, 1998). A number of authors (e.g. Tinkham et al., 2001; Johnson et al., 2003; White et al., 2007) have successfully used this approach to assess stable mineral assemblages in metapelitic rocks (Baldwin et al., 2005). A number of programs capable of generating phase diagrams are currently available; the program used in this study was THERMOCALC (Powell et al., 1998).

THERMOCALC

THERMOCALC is a versatile program capable of calculating conventional phase diagrams, petrogenetic grids, and pseudosections (Bucher and Fry, 2002). THERMOCALC (*v. 3.26*) and the dataset of Holland and Powell (1998, version 5.5, updated Nov. 2003), was used in this study to model phase relationships of the AMCC footwall (Powell and Holland, 1988; Holland and Powell, 1998; Powell et al., 1998). This program calculates mineral equilibria involving solid solutions through the simultaneous solution of non-linear equations (Powell et al., 1998). Equilibrium relationship equations used in pseudosections are supplemented by mass balance equations (Powell et al., 1998). THERMOCALC contains two main components: the application itself, and the internally consistent thermodynamic dataset it uses (Powell et al., 1998). Solution models are continually added to the thermodynamic dataset enabling modeling to more precisely approximate natural systems (Baldwin et al., 2005; Holland and Powell, 1998).

THERMOCALC requires three input files in order to operate: a preference file, a file containing the thermodynamic properties of the phases, and a file that contains coded *a-X* (activity-composition) relationships of the solid solution phases as well as scripts to specify the type of calculation to perform and the rock composition (Powell and Holland, 2001). The last file is modified by the user to create the desired diagram, with great importance placed on choosing a chemical system. The chemical system, specified in terms of molar proportions of oxides, indicates which phases and the substitutions within them will be considered (Powell et al., 1998). The bulk composition of the rock must be made up of an assemblage of phases in interest (Powell et al., 1998). Phases can only involve those end members that occur in the thermodynamic dataset used (Powell et al., 1998). Solution models for phases in interest are entered into the THERMOCALC data file as coded *a-X* relationships. Choosing the correct chemical system is vital for representing the compositions of all the phases in interest (Powell and Holland, 2001). The chemical system K_2O-FeO-MgO-Al_2O_3-SiO_2-H_2O (KFMASH) has been very successful in modeling reactions in pelitic systems (Powell et al., 1998; Worley and Powell, 1998). One major limitation with the KFMASH system is that plagioclase feldspar is not incorporated into calculations although it is generally abundant in pelitic rocks (Worley and Powell, 1998). This study incorporated Na_2O and CaO (NCKFMASH) into the chemical system, so critical solid solution can occur between plagioclase end-members. Manganese (MnO) was not included in the chemical system as the garnet end-member spessartine is the only mineral which this oxide would be incorporated into. Garnet in the AMCC is extremely iron-rich and almost purely almandine. Including MnO would therefore have a negligible effect on the position of phase equilibria boundaries and was therefore ignored.

Zoning of garnets in metamorphic rocks is problematic as rims are typically not in equilibrium with surrounding minerals. Fractionation of the effective bulk composition is caused by garnet growth (Vance and Mahar, 1998) and must be taken into consideration when choosing a chemical system. Initial petrographic observations of garnets present led to the belief that zoning was a possibility as most appeared to have a core riddled with inclusions. Four garnets from two slides (3 from MTAF13, 1 from MTA15c) were compositionally mapped for manganese, magnesium, calcium, and iron on the electron microprobe at WSU. Mapping of these elements confirmed only slight zoning of calcium (Figure 5-2). Microprobe data shows little compositional variability between rims and core of garnets with respect to calcium, suggesting that this slight zoning is not indicative of growth zoning.

Pseudosection calculations were performed in the model chemical system NCKFMASH in order to account for all the major chemical components of the phases present. Bulk rock composition, from XRF data, was entered as molar proportions into the THERMOCALC data file. Phases containing ferric iron are not capable of being modeled; however XRF data treats all iron as ferric. Simple conversion of ferric to ferrous iron is completed by multiplying by a factor of .899. Essential phases in metapelites do not typically incorporate ferric iron as a major component (Vance and Mahar, 1998). Major phases can contain small amounts of iron as ferric iron but stoichiometry suggests that these amounts are trivial (Vance and Mahar, 1998).

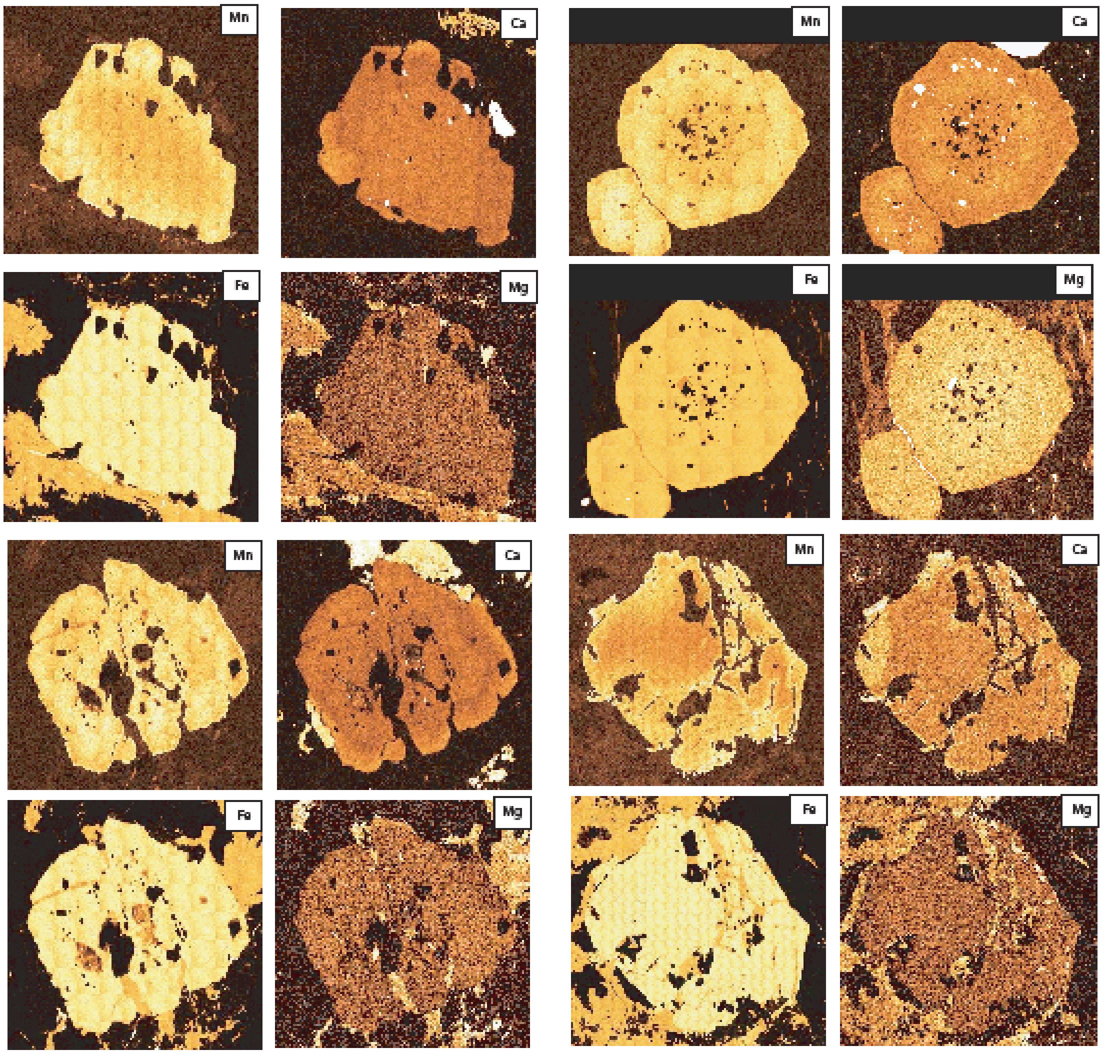

Figure 5-2. X-ray maps of manganese, calcium, iron, and magnesium of garnets in samples MTAF13 and MTA15c. Maps show slight zoning with respect to calcium and manganese.

The amount of water in the system must be inferred indirectly. Water is assumed to be in excess (saturated) until melting occurs (Vance and Mahar, 1998). Above the solidus, the amount of water is set to be just in excess at the solidus (Powell and Holland, 2001). Two data files were thus necessary for a complete pseudosection: one in which water is in excess below the solidus and another where water was set as eight molar percent (just at saturation at the solidus) for calculations above the solidus. This amount of water allowed hydrous minerals to stay in the system without hindering melt formation. Table 5-2 shows bulk composition of MTAF13 used in pseudosection calculations.

Three output files also exist: a data file that contains the results of the calculations performed, a file containing extended results of the calculations performed, and a file that contains results that can be assembled for the drawpd graphics application to plot the phase diagram as a postscript file (Powell and Holland, 2001). Output files automatically overwrite after each THERMOCALC run. A separate file is needed where calculation results are assembled. This file assembles the lines of the pseudosection through the drawpd application, which generates postscript output. It is often best practice to build up diagrams line by line on paper before assembling the results in a separate file, as THERMOCALC does not calculate both stable and metastable extensions of lines.

Table 5-2. Whole rock bulk composition of MTAF13.

Component	Mol %
SiO_2	67.45
Al_2O_3	14.75
CaO	0.92
MgO	3.28
FeO	10.00
K_2O	2.51
Na_2O	1.10
H_2O	8.00

Pseudosections are built based on the composition and relative molar abundance of minerals in each assemblage field. The lines that make up pseudosections are phase stability boundaries. Points, where the modes of two phases are zero, and lines, where the mode of one phase is zero, are calculated from the lower variance field (Powell et al., 1998). THERMOCALC does not give the relative stabilities of points and lines, requiring manual application of this through the phase rule and Schreinemakers' analysis. Schreinemakers' rules state that: the metastable extension of phase [i] lies between two

[i] producing reactions in which all angles between stable minerals are less that 180° (Spear, 1993; Bucher and Fry, 2002). The phase rule, under equilibrium conditions, relates the number of variables in a system and the number of equations that can be written to form the fewest possible phases (Hyndman, 1985; Bucher and Fry, 2002):

$$V = C + 2 - P$$

where V is the variance or degrees of freedom in the system; C equals the number of components; P refers to the number of phases in the system; and the number 2 is held constant, representing the two intensive variables pressure and temperature (Hyndman, 1985; Bucher and Fry, 2002). Four stability fields must exist around one invariant point. Following the phase rule, each field must systematically increase or decrease by a variance of one so that two fields separated by a line will not have the same variance; two divariant fields will be separated by a univariant line (Figure 5-3) (Powell and Holland, 2001).

THERMOCALC outputs the mineral composition and modal information for each field calculated. Isopleths of phases can also be calculated by setting a compositional variable of a phase to a range of particular values. In this way, a whole pseudosection can be contoured for a compositional variable of a phase, thus illustrating how a mineral changes composition with pressure and temperature. Direct measurement of the mineral compositions of phases using microprobe analysis allows for the accurate selection of the equilibrium field on a contoured pseudosection. Measured compositional variables of different phases should all coincide within or around the same peak mineral assemblage field on the pseudosection.

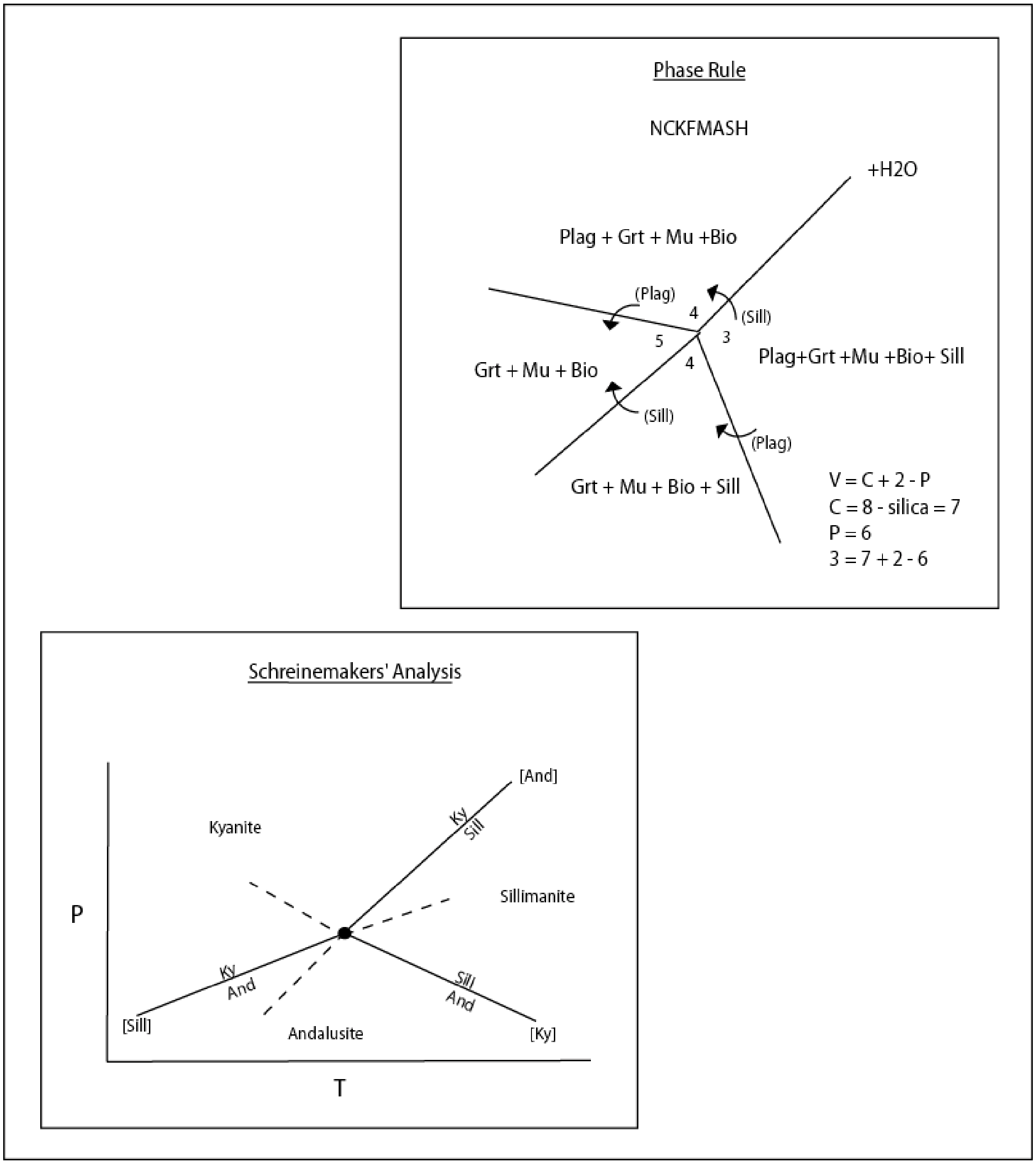

Figure 5-3. Illustration showing the phase rule and Schreinemakers' analysis. Arrows on the phase rule diagram indicate a phase leaving the system. P = phase, C = component, V = variance, and 2 represents the two intensive variables pressure and temperature. The component silica is set in excess and therefore is not considered a component in the equation. NCKFMASH refers to the chemical system used in the construction of pseudosections. Dashed lines on Schreinemakers' Analysis indicated metastable extensions. Sill = sillimanite, Ky = kyanite, and And = andalusite.

Microprobe Analysis

Microprobe analysis was completed using the Cameca Camebax electron microprobe at Washington State University in Pullman, Washington. Biotite, plagioclase feldspar, garnet, and muscovite were analyzed at 15 kV accelerating voltage, 10 nA beam current conditions. A total of eight biotite, six feldspar, five garnet, and two muscovite grains were analyzed for a total of twenty-five spot analyses on biotite, thirty on feldspar, one-hundred-one on garnet, and six on muscovite on the two thin sections MTAF13 and MTA15c. Results whose percentages did not fall in the range of 99-101% for garnet and plagioclase and 94-100% for biotite and muscovite were discarded. Micas typically contain 4-6% water in their crystalline structure which is not recorded in probe analysis, thus results of < 94% are considered reliable. This left forty-eight spot analyses on garnet, sixteen on feldspar, nine on biotite, and four on muscovite on slide MTAF13. Slide MTA15c resulted in thirty-six spot analyses on garnet, six on feldspar, nine on biotite, and two on muscovite.

AX

The THERMOCALC subprogram AX is an activity calculation program that uses raw microprobe data to calculate mineral end member activities and to convert the elemental oxide data to cation unit formulae needed for subsequent geothermobarometry calculations made using THERMOCALC (Grice, 2006). Using the assumed peak metamorphic mineral assemblage from petrographic observations, calculations in AX were carried out at 4.0 kbar and 650°C. AX calculates end member activities using ideal and non-ideal mixing models. Standard deviations given in the results represent the minimum error, as the uncertainties stem from typical microprobe error (0.05 wt% minimum + 1.5% relative on each oxide) and are propagated to the calculated activities; they do not take into account activity model uncertainties (Powell and Holland, 2001).

THERMOCALC uses the least-squares method in average *P-T* as this allows for the determination of pressures and temperatures from the thermodynamics of an independent set of reactions, including uncertainties and correlations on the activities and enthalpies of formation of the end-members (Powell and Holland, 1994). It is best to start by calculating average pressure at a series of temperatures, as temperatures are typically known better through the general phase relationships of a rock (Powell and Holland, 1994). Once a pressure is calculated, the range of pressures in which temperatures are calculated are easily determined. Calculations are much more robust if done so in this manner, as only one variable is being solved for directly without iteration (Powell and Holland, 1994).

The composition of the mean average plagioclase was paired against mean garnet, biotite, and ± muscovite compositions for estimation of peak metamorphic conditions. Two sets of results are reported, one where muscovite is included in the calculations and another where muscovite is not included. An Excel worksheet by (Waters, http://www.earth.ox.ac.uk/~davewa/pt/pt02_mica.html, 11/07) was used to plot error ellipses from the results of average *P-T* and their uncertainties.

CHAPTER 6

RESULTS

PETROGRAPHY

The Prichard Formation in the Anaconda-Pintlar and Flint Creek ranges outcrops as a cliff-forming reddish-brown weathering metapelite. Outcrop scale mapping was not accomplished as weathering of the rocks is intense and leaves little to be observed at the macroscopic scale. Samples were collected *in situ* near the top of a cirque along a ~ 1 mile traverse at approximate GPS location E 033031 N 5103478 near Lake of the Isle, west of Anaconda, Montana. Samples were taken when there appeared to be a lithologic change in the outcrop or after so many paces had been taken and no change was observed.

A wide range of bulk compositions exists between the thirty thin sections from the twenty-two collected hand samples. Pelitic, quartz-rich, and mafic horizons are found throughout collected samples. There is no distinct lithologic-spatial relationship among collected samples. Mafic and quartz-rich samples were collected between pelitic samples. Pelitic layers are much more common than both mafic and quartz-rich horizons.

Leucosome on the outcrop scale appears as discordant lensoidal “stringers”, not longer than a few feet in length. More migmatitic, leucosome rich rocks are present as large boulders in the talus beneath the cliffs. Smaller cm-scale patches of leucosome are present in pelitic hand samples. Quartz-rich horizons are distinct from pelitic layers in outcrop as they are felsic and do not contain abundant mica. Mafic horizons are not as easily identified in outcrop as their weathered surface appears almost identical to pelitic horizons. Hand samples of mafic layers contain small but visible garnet, which is much rarer in pelitic hand samples.

Phases present in the pelitic schist unit include quartz, biotite, sillimanite, plagioclase, muscovite, potassium feldspar, and garnet. Potassium feldspar is found in association with leucosome as is large, idioblastic muscovite. Accessory phases in pelitic rocks include zircon and/or monazite, opaques, and apatite. Quartz, amphibole, garnet, plagioclase, and chlorite are present in mafic horizons. Opaques are present as an accessory phase. Garnet grains in mafic rocks are ~1 mm in diameter with irregular, embayed rims. Mafic rocks are thought to be old, altered sills. Quartz-rich sections are primarily composed of fine-grained quartz and biotite with lesser muscovite, plagioclase, and garnet. Garnet is extremely retrograded in these layers. Very minor radiation halos are present in biotite, indicating zircon and/or monazite is present as an accessory phase. Opaques are also present as an accessory phase in quartz rich samples.

Pelitic schists can be categorized into two groups: garnet-bearing and garnet-absent. Garnet-absent schists are more abundant and contain a wider range of variability in the modal amounts of phases. Consistent through all samples is a foliation comprised of both biotite and fibrolitic sillimanite. In most cases, these two minerals are typically present in equal proportions. However, in some rocks primary fibrolite almost entirely comprises the foliation while in others biotite is the main constituent. Secondary fibrolite is also present in pelitic rocks. Secondary fibrolite tends to overgrow quartz and feldspar. Typically, the amount of secondary fibrolite is proportional to the quantity of primary fibrolite. These samples contain large grains of plagioclase and potassium feldspar ≥ 4mm and lesser quartz than most samples. Crenulation cleavage is developed within fibrolitic bands. Muscovite is less common in rocks where biotite is the main phase comprising the foliation. A few large laths of late muscovite crosscut the foliation in some sections. In few sections, muscovite appears to be altering to fibrolite. Sillimanite is present in all sections as slender needles, fibrolite, and xenoblastic grains. One sample is composed of ~50% sillimanite, where it is present as fibrolite, needles, xenoblastic and idioblastic crystals with secondary fibrolite tending to overprint more idioblastic grains. Some sections also appear to have muscovite replacing sillimanite within the foliation. Leucosome patches occur in more than half of the samples. Plagioclase grains are typically abundant in most slides, except for a few sections where it occurs only as small, xenoblastic grains in small patches with muscovite and quartz. This may represent a replacement texture or pseudomorph of a melt pocket.

Typical modal proportions of pelitic schists containing garnet are quartz = 30%, sillimanite = 25%, biotite = 30%, muscovite = 5%, feldspar = 5%, and garnet = <5%. Both biotite and fibrolite comprise foliation in garnet bearing metapelites. Garnet is a minor constituent, making up less than ~5% of the slide. Large xenoblastic sillimanite grains, needles, and fibrolite, are present with some fibrolite overgrowth. Garnet contains inclusions of feldspar, quartz, biotite, and sillimanite needles. Garnet appears as sub-idioblastic grains that are fractured and crosscut by veins filled with late biotite.

The equilibrium mineral assemblage for the pelitic schists was determined by textural relationships. Garnet + plagioclase + sillimanite + biotite + quartz +/- muscovite are considered to be part of the peak mineral assemblage. Plagioclase, sillimanite needles, and biotite are all found as inclusions within garnet suggesting contemporaneous growth of these minerals during prograde metamorphism. Some sections contain laths of muscovite within biotite foliation, while others contain laths that are more typically of late phase growth and crosscut foliation.

Table 6-1. Mineral abbreviations.

Abbreviation	Mineral
Ab	Albite
Als	Aluminosilicate
An	Anorthite
Bio	Biotite
Cd	Cordierite
Chl	Chlorite
Grt	Garnet
H_2O	Water
Kspar	Potassium Feldspar
Ky	Kyanite
Leuc	Leucosome
Liq	Liquid (Leucosome)
Mus	Muscovite
Ortho	Orthoclase
Plag	Plagioclase
Ru	Rutile
Sill	Sillimanite
Zo	Zoisite

Modal proportions in sample MTAF13 are quartz = 30%, sillimanite = 20%, biotite = 30%, muscovite = <5%, feldspar = 10%, and garnet = <5%. The equilibrium metamorphic assemblage in sample MTAF13 is Grt + Plag + Sill + Bio + Qtz + Mus. Mineral abbreviations are shown in (Table 6-1). Accessory phases include oxides, monazite, zircon, and apatite. Minor prograde 5% muscovite is intergrown with matrix biotite (Figure 6-1a), along with few, small > 1 mm laths of muscovite occurring in plagioclase, indicating early growth of the mineral (Figure 6-1b). Muscovite also appears to be in textural equilibrium with garnet. Muscovite appears to have grown throughout the evolution of the rock as indicated by early growth by inclusions in plagioclase and later growth by textural equilibrium with garnet. Muscovite grains of about the same size also cut biotite foliation, suggesting late, post-peak growth (Figure 6-1c). Schistosity is defined by biotite and fibrolite. Garnet occurs as small ~125 µm - 1 mm idioblastic to subidioblastic crystals (Figure 6-2a). Larger garnet ~750 µm -1 mm typically contains inclusions of biotite, plagioclase, and quartz. Most garnet is fractured and contains veins filled with late biotite (Figure 6-2b). Although garnet is distributed throughout the thin section, a notable cluster of garnet is

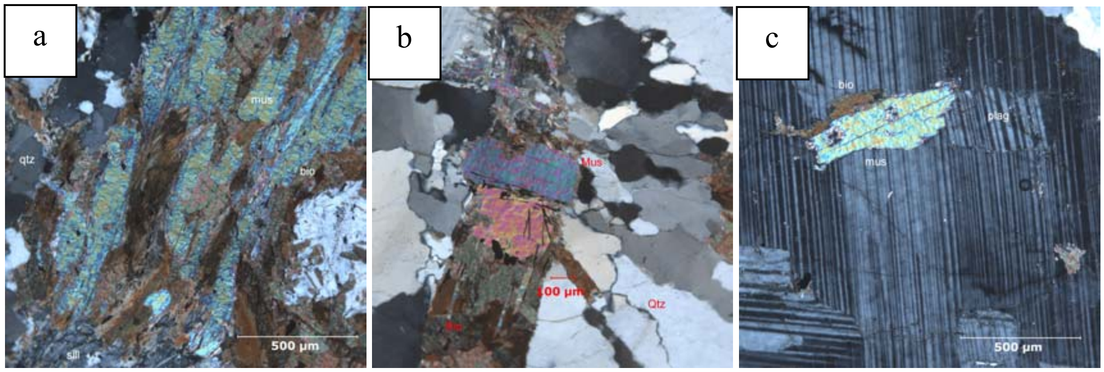

Figure 6-1. Photomicrographs of muscovite within MTAF13, showing stability throughout the evolution of footwall rocks. All photographs were taken using the 10x objective. Figure 6-1a shows muscovite intergrown with biotite, which comprises part of the foliation of the rock. 6-1b shows muscovite cross-cutting biotite foliation, indicating late growth of the mineral. Plagioclase with inclusions of muscovite is also indicative of early growth (6-1c).

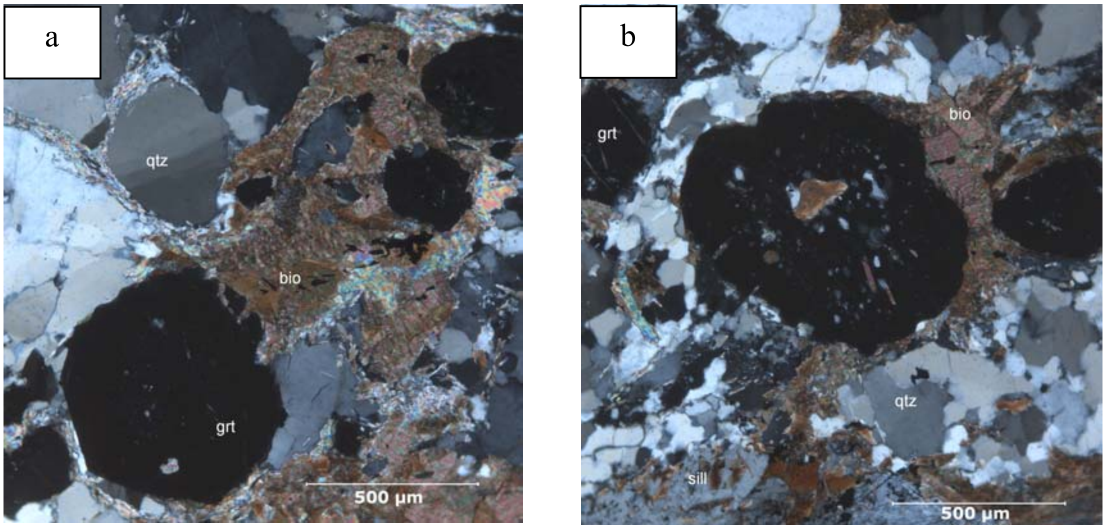

Figure 6-2. Typical growth habit and size of garnet within pelitic schists (6-2a). Inclusion suit in 6-2b consists of biotite, plagioclase, quartz, and sillimanite. Sillimanite needles are very small and are not seen under this magnification. Photomicrographs were taken under the 10x objective of sample MTAF13.

present in one region of the section adjacent to a muscovite and quartz leucosome patch. Garnet in this cluster is mainly set cleanly in quartz. Large, up to 5 mm, idioblastic plagioclase grains are prevalent throughout the slide. Plagioclase contains inclusions of biotite, sillimanite, and quartz (Figure 6-3). Quartz grains vary in size, generally showing undulatory extinction with irregular sutured boundaries. Sillimanite is abundant and takes on many different growth habits. Fibrolite occurs within biotite bands (Figure 6-4a). Large, up to 3mm, prismatic sillimanite is also present, often with biotite and oxide overgrowths and monazite/zircon inclusions (Figure 6-4b). Xenoblastic grains of sillimanite are intergrown with matrix biotite and usually contain small amounts of fibrolite and/or sillimanite needles (Figure 6-4c). Sillimanite needles occur as inclusions within almost every grain in the slide.

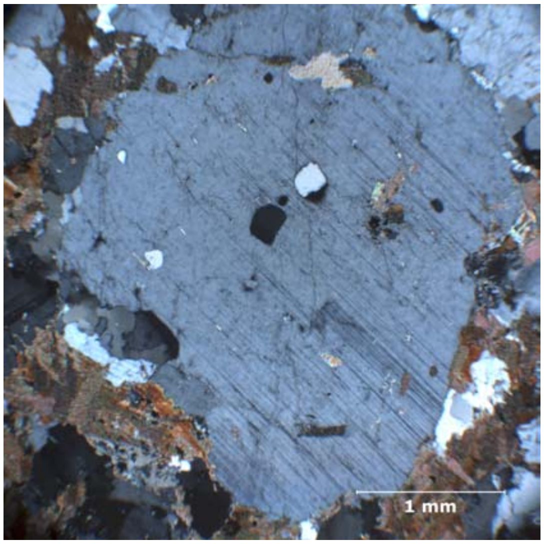

Figure 6-3. Large plagioclase grain containing inclusions of biotite, quartz, and sillimanite in sample MTAF13. Sillimanite is present as very small needles in the upper left part of the grain. Observed under 4x magnification.

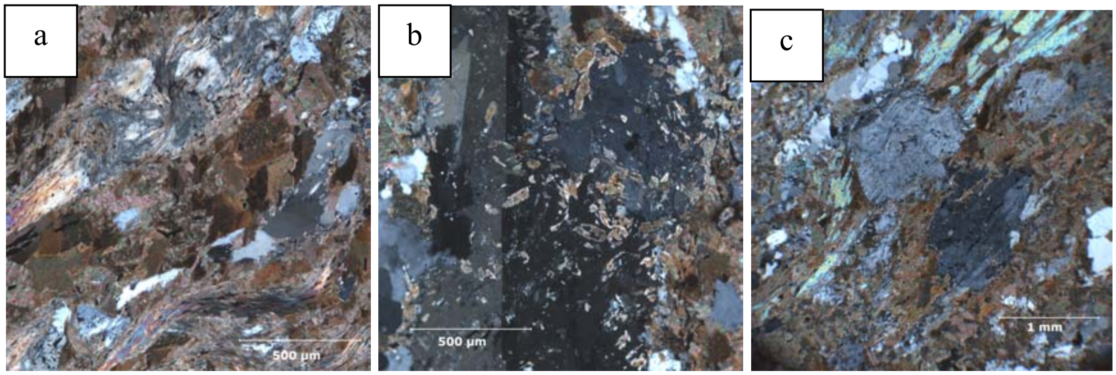

Figure 6-4. Fibrolite intergrown with biotite to comprise the foliation in MTA15b. 6-4b shows large idioblastic sillimanite grains with biotite overgrowths in slide MTAF13. Large grey, xenoblastic grains in 6-4c are yet another common growth habit of sillimanite in footwall rocks of the AMCC (picture of MTAF13). All photomicrographs were taken under the 10x objective.

Melt although present within rock MTAF13, is also not considered to be part of the main peak mineral assemblage. Melt occurs as small discordant pods that have sharp boundaries (Figure 6-5). Leucosome is dominated by coarser quartz and muscovite grains.

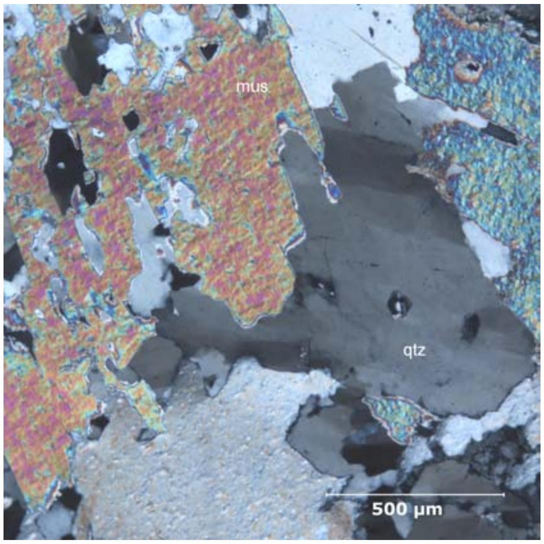

Figure 6-5. Leucosome within MTAF13. Large muscovite and quartz grains are the typical constituents of melt with in metapelites. View is under 10x magnification.

Sample MTA15c is a garnet bearing metapelite with similar modal proportions to MTAF13: quartz = 30%, sillimanite = 25%, biotite = 30%, muscovite = <5%, feldspar = <5 % and garnet = <5%. The main difference between these samples is the modal amount of plagioclase and leucosome. Feldspar occurs as small ≤500 µm xenoblastic grains in association with muscovite and quartz, which could represent a replacement texture. Leucosome is less defined and only occurs in small ~2 mm blebs in hand samples, while melt in MTAF13 is more distinct and is ≥ 4 inches in hand sample. Melt in thin section shows large quartz grains with undulatory extinction with minor muscovite. Lesser garnet is found in this sample that in MTAF13. These grains are slightly more altered than garnet in MTAF13. Fractures and biotite veins cut garnet.

MTA15c exhibits a stronger foliation than MTAF13. Biotite comprises most of the foliations with some intermixed fibrolite. Quartz grains within foliation are usually elongated in the direction of the fabric. Quartz exhibits undulatory extinction with irregular sutured boundaries. Sillimanite is also found as xenoblastic grains with secondary fibrolite overgrowing it in some places.

Mineral Chemistry

Representative electron microprobe analyses for garnet, biotite, plagioclase, and muscovite are shown in Table 6-2. Complete microprobe analyses results can be found in Appendix B. Rocks MTAF13 and MTA15c show slight variations in mineral chemistry compared to each other with even smaller disparity between like grains within the same slide.

Garnet

Garnet in both MTAF13 and MTA15c is almandine-rich and unzoned. Garnet within slide MTAF13 has an average composition of $X_{Alm}^{Grt} = .83$, where $X_{Alm}^{Grt} = [Fe^{2+} / (Fe^{2+} + Mg + Mn + Ca)]$. Magnesium, manganese, and calcium end-members were calculated in the same form, resulting in $X_{Pyp}^{Grt} = .07$, $X_{Spss}^{Grt} = .07$, $X_{Gr}^{Grt} = .04$, respectively. Calculation of garnet for $X_{Fe,}$ where $X_{Fe,} = [Fe / (Fe^{2+} + Mg)]$, is on average $X_{Fe,} = .92$.

Garnet in sample MTA15c is slightly more almandine-rich with average $X_{Alm}^{Grt} = .87$. Magnesium, manganese, and calcium end members averaged $X_{Pyp}^{Grt} =.06$, $X_{Spss}^{Grt} =.04$, $X_{Gr}^{Grt} = .02$, respectively. These garnets have an average of $X_{Fe,} = .93$. Where garnet rims show less than a half weight percent zoning in MTAF13, garnets in sample MTA15c have an average of almost one weight percent increase spessartine content at the rims with a decrease in pyrope, which is characteristic of retrograde reequilibration (House, 1997). Although elemental mapping of garnets suggest slight zoning of calcium in garnets (Figure 5-1), microprobe data indicate only a slight molar variation in the grossular component.

Table 6-2. Representative microprobe analysis.

	Garnet MTAF13		Garnet MTA15c		Plagioclase MTAF13		Plagioclase	Biotite	Biotite	Muscovite	Muscovite
Weight %	C	R	C	R	C	R	MTA15c	MTAF13	MTA15c	MTAF13	MTA15c
Al2O3	20.83	20.86	20.73	20.64	26.12	24.74	23.36	20.24	20.67	36.96	36.59
SiO2	36.95	37.27	36.21	36.10	59.67	60.69	63.84	33.33	32.48	45.08	44.26
FeO	36.12	36.93	38.55	37.97	0.04	-0.02	0.09	25.72	26.34	1.14	1.28
CaO	1.40	1.02	0.57	0.98	6.34	5.86	4.29	0.00	0.00	0.00	0.00
MgO	1.95	1.39	1.49	1.46				5.37	4.88	0.28	0.31
MnO	2.83	2.98	2.24	2.28				0.08	0.06	0.00	0.02
K2O					0.06	0.04	0.04	8.72	8.96	9.49	9.66
Na2O					7.54	8.15	9.16	0.23	0.26	1.19	1.14
TiO2								2.42	1.63	0.43	0.45
Total	100.08	100.45	99.79	99.43	99.77	99.46	100.78	96.11	95.28	94.57	93.71
Cations											
Al	1.99	1.99	2.02	2.01	1.31	1.30	1.21	3.71	3.85	5.82	5.83
Si	3.00	3.02	2.97	2.98	2.71	2.71	2.78	5.18	5.13	6.02	5.99
Fe	2.45	2.50	2.62	2.62	0.00	0.00	0.00	3.36	2.48	0.13	0.14
Ca	0.12	0.09	0.06	0.09	0.28	0.28		0.00	0.00	0.00	0.00
Mg	0.24	0.17	0.16	0.18				1.23	1.15	0.06	0.06
Mn	0.20	0.20	0.19	0.16				0.01	0.01	0.00	0.00
K					0.01	0.00	0.00	1.73	1.81	1.62	1.67
Na					0.69	0.71	0.78	0.07	0.08	0.31	0.30
Ti								0.28	0.19	0.04	0.14
Total	7.99	7.97	8.02	8.02	4.99	5.00	4.77	15.57	14.70	14.00	14.14
Plag(An)					0.21	0.28	0.21				
X(Fe)	0.91	0.94	0.94	0.94				0.73	0.75		
X^{Grt}_{Alm}	0.82	0.84	0.87	0.86							
X^{Grt}_{Pyp}	0.08	0.06	0.06	0.06							
X^{Grt}_{Spss}	0.06	0.07	0.05	0.05							
X^{Grt}_{Gr}	0.04	0.03	0.02	0.03							

Feldspar

Matrix plagioclase in sample MTAF13 consists typically of large idioblastic grains of X_{An}^{Pl} =.22-.32, where X_{An}^{Pl} = [Ca/(Ca + Na + K)] based on recalculation to eight oxygens. No significant intragrain zoning occurs, although anorthite content varies up to one weight percent between grains. Plagioclase in MTA15c consist of small, xenoblastic grains that contain X_{An}^{Pl} =.16-.32. Plagioclase is rare in this slide and occurs in small patches with muscovite and quartz. Anorthite content in these grains varies up to two weight percent, although no zoning could be determined due to the size of the grains.

Biotite

Biotite grains were recalculated based on eleven oxygens and show uniform composition. Biotite in sample MTAF13 has a mean X_{Fe} = .73. MTA15c shows more variability with an average of $X_{Fe,}$ = .75, a high of X_{Fe} = .76, and a low of X_{Fe} = .66. TiO_2 concentrations vary from 1.71-2.41 and 1.62-2.21 weight percent in MTAF13 and MTA15c, respectively. Composition of biotite does not differ significantly when in contact with garnet.

Muscovite

Muscovite was recalculated based on eleven oxygens. Muscovite in sample MTAF13 has a mean X_{Fe} = .73, with a low of X_{Fe} = .70 and a high of X_{Fe} = .74. Muscovite in MTA15c contains more variability with an average of $X_{Fe,}$ = .67, a high of X_{Fe} = .70, and a low of X_{Fe} = .64. Silica per unit formula was 3.00 in all samples analyzed.

THERMOCALC

The constructed pseudosection shows subsolidus and suprasolidus phase relations for rock MTAF13 in the model system NCKFMASH (Figure 6-6; 6-6a). The equilibrium

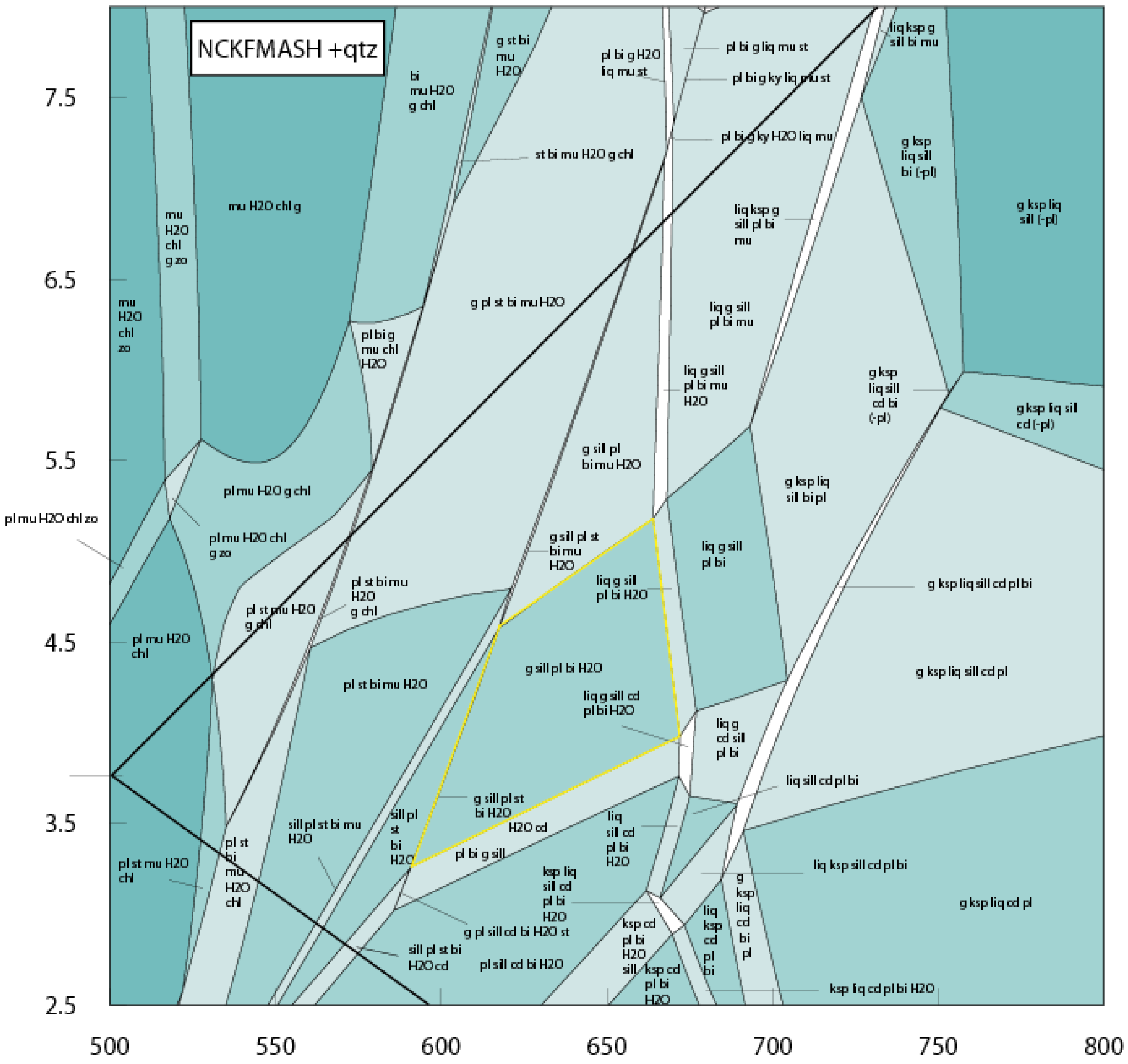

Figure 6-6. NCKFMASH pseudosection of sample MTAF13. Peak mineral assemblage is outlined in yellow. Lines on a pseudosection should be considered bands instead of sharp boundaries. Muscovite is considered to be part of the peak assemblage based on petrographic analysis. Muscovite is stable directly above the outlined field. Aluminum triple point is that of Holdaway (1971) and constructed by Baldwin (personal comm.).

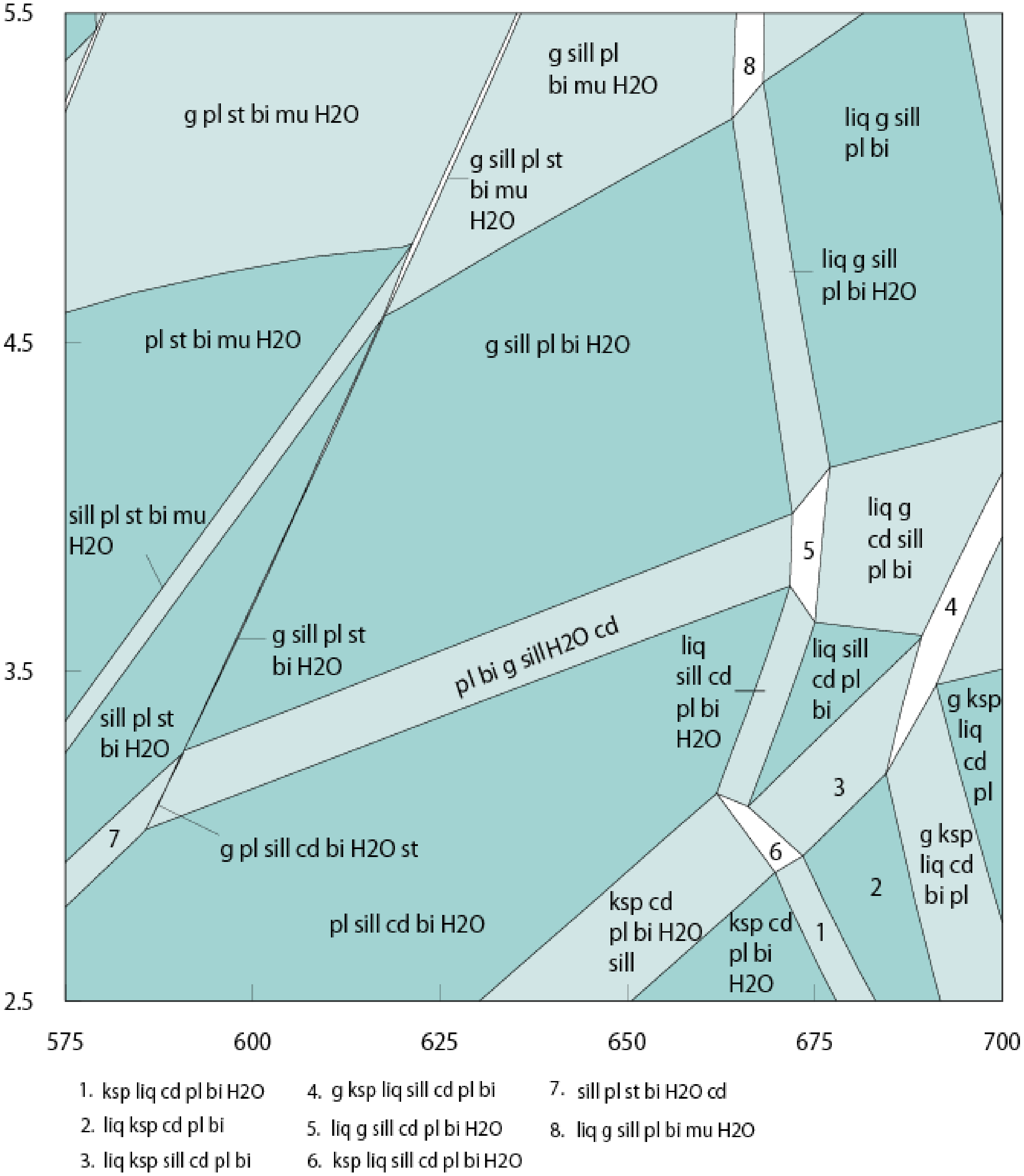

Figure 6-6a. Enlarged image of the peak mineral assemblage and surrounding fields.

mineral assemblage, based on petrographic and microprobe analyses, is Bio + Grt + Sill + Qtz + Plag + Mus and is constrained to 3.3-5.3 kbars and 590-665°C. Muscovite was stable throughout the evolution of the rock. Melt is considered to be late phase.

THERMOCALC calculates phase proportions on a one-oxygen basis; as a result, molar percent can be generally taken to approximate volume percent (Johnson et al., 2003). Modal proportions of the peak mineral assemblage in MTAF13, based on THERMOCALC are: garnet = 2%, plagioclase = 12%, sillimanite = 14%, biotite = 35%, and quartz = 37%. THERMOCALC estimations are similar to modal proportions observed petrographically with a slightly lower concentration (6%) of sillimanite and a higher modal amount of quartz (7%).

Mineral Stability

The absence of staurolite in the AMCC pelites allows further constraints to be placed on the peak metamorphic conditions obtained in the footwall of the AMCC. Staurolite stability ranges a small temperature field from 520-680°C over the entire pressure of the pseudosection. Staurolite breaks down readily once outside its stability field and typically will not be perceptible even if the prograde path of the rock had passed through that field, which is the likely case of AMCC rocks. The staurolite *out* isograd, with the trivariant Bio + Grt + Sill + Qtz + Plag + H2O + St field, provides a lower bound on the temperature of the equilibrium mineral assemblage described above (Figure 6-7). Cordierite is stable over a wide temperature window but confined to lower pressures. Lack of cordierite in AMCC pelites also confines the peak mineral assemblage. The trivariant field Bio + Grt + Sill + Qtz + Plag + H2O + Cd provides a lower bound on pressure (Figure 6-8). These two phases, along with the position of the solidus, tightly

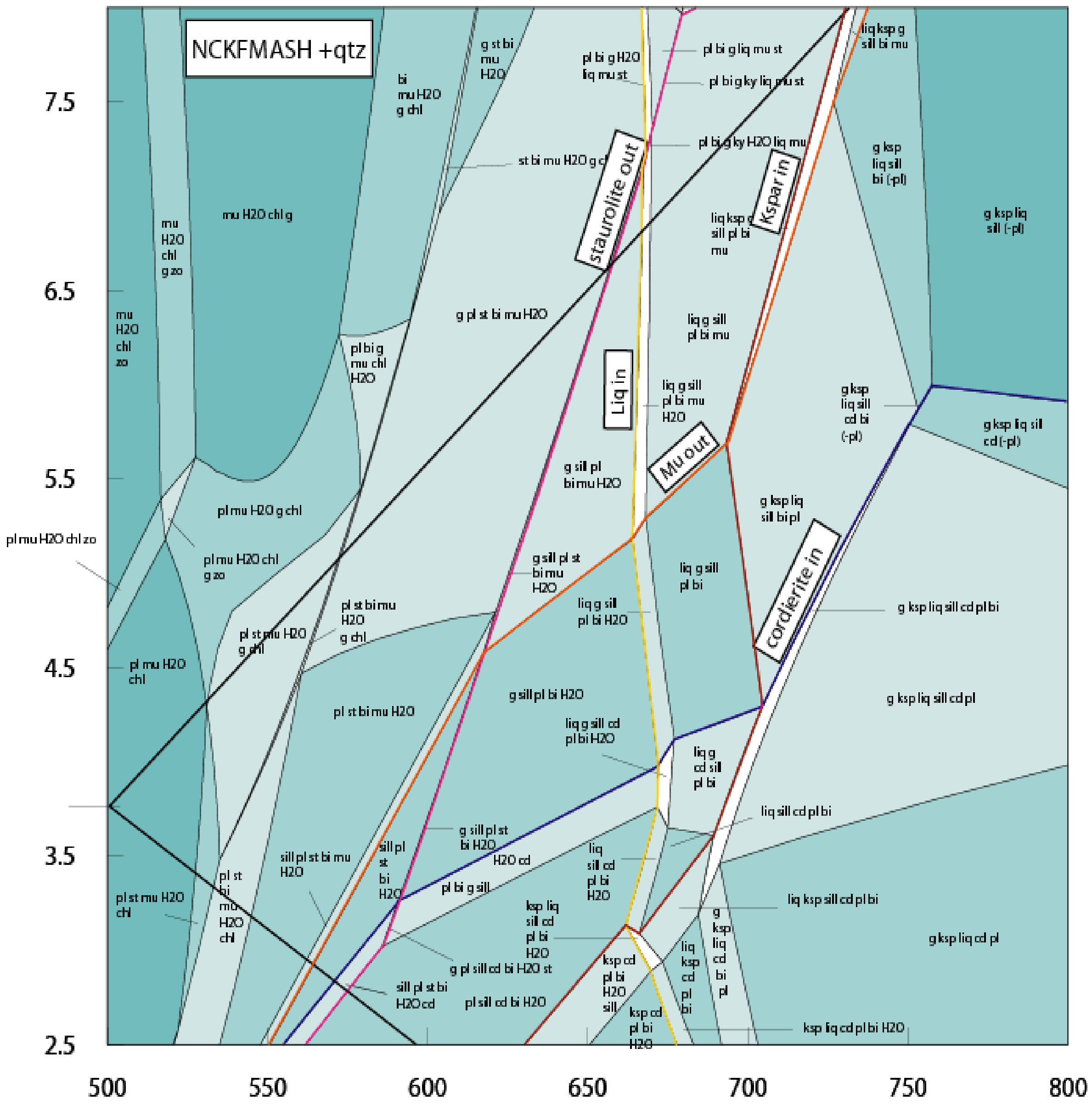

Figure 6-7. NCKFMASH pseudosection with phase isograds highlighted. These isograds place constraints on peak metamorphism. The staurolite out-isograd places the lower temperature limits on metamorphism, as it is not observed in petrographic analysis. It is outlined in pink. The cordierite in-isograd constrains the lower pressure boundary and is outlined in blue. The liquid in-isograd, outlined in yellow, constrains the upper temperature limit. Potassium feldspar (kspar) in-isograd is shown in red. Kspar is not present in the rock, placing yet another constraint on the peak mineral assemblage. The muscovite out-isograd is outlined in orange. Little prograde muscovite is in equilibrium with the peak mineral assemblage. It is likely that peak metamorphic conditions crossed the muscovite out-isograd and into the trivariant field Grt +Sill + Plag +Bio +Mus +H2O.

confine the *P-T* window in which these rocks evolved. Melt is not ubiquitous between samples, indicating maximum *T* conditions occurred either just above or below the solidus, depending on bulk composition, and thus can be used as another boundary line on the equilibrium *P-T* conditions. The solidus (where melt is introduced into the assemblage) occurs at 665°C, with the trivariant field Bio + Grt + Sill + Qtz + Plag + H2O + Melt constraining the upper temperature field of the peak mineral assemblage (Figure 6-8).

Sillimanite is the only aluminosilicate (Al_2SiO_5) mineral present in the AMCC footwall samples. The Al_2SiO_5 triple point from Holdaway (1971), calculated by Baldwin (2007, personal comm.) .is superimposed on the pseudosection. This shows that the mineral field Bio + Grt + Sill + Qtz + Plag + H2O is well within sillimanite stability.

Isopleths

Garnet, biotite, and plagioclase compositional isopleths calculated in THERMOCALC are overlain on the pseudosection (Figure 6-8). Configuration of plagioclase isopleths vary from nearly horizontal to sub-vertical. Composition of plagioclase varies from $An_{.25-.60}$ across the entire pseudosection. Higher anorthite compositions occur at the higher and lower end of the temperature spectrum on the pseudosection. Plagioclase leaves the system on the upper left side of the diagram, where calcium goes into zoisite. Plagioclase also leaves the diagram in the upper right corner around 5.5 kbars at 700°C. Mean plagioclase composition from microprobe results is $An_{.28,}$ which corresponds perfectly to the $An_{.28}$ isopleth on the pseudosection that runs through the peak metamorphic mineral assemblage Bio + Grt + Sill + Qtz + Plag (Figure 6-8). Melt-bearing assemblage fields surrounding the peak mineral assemblage contain

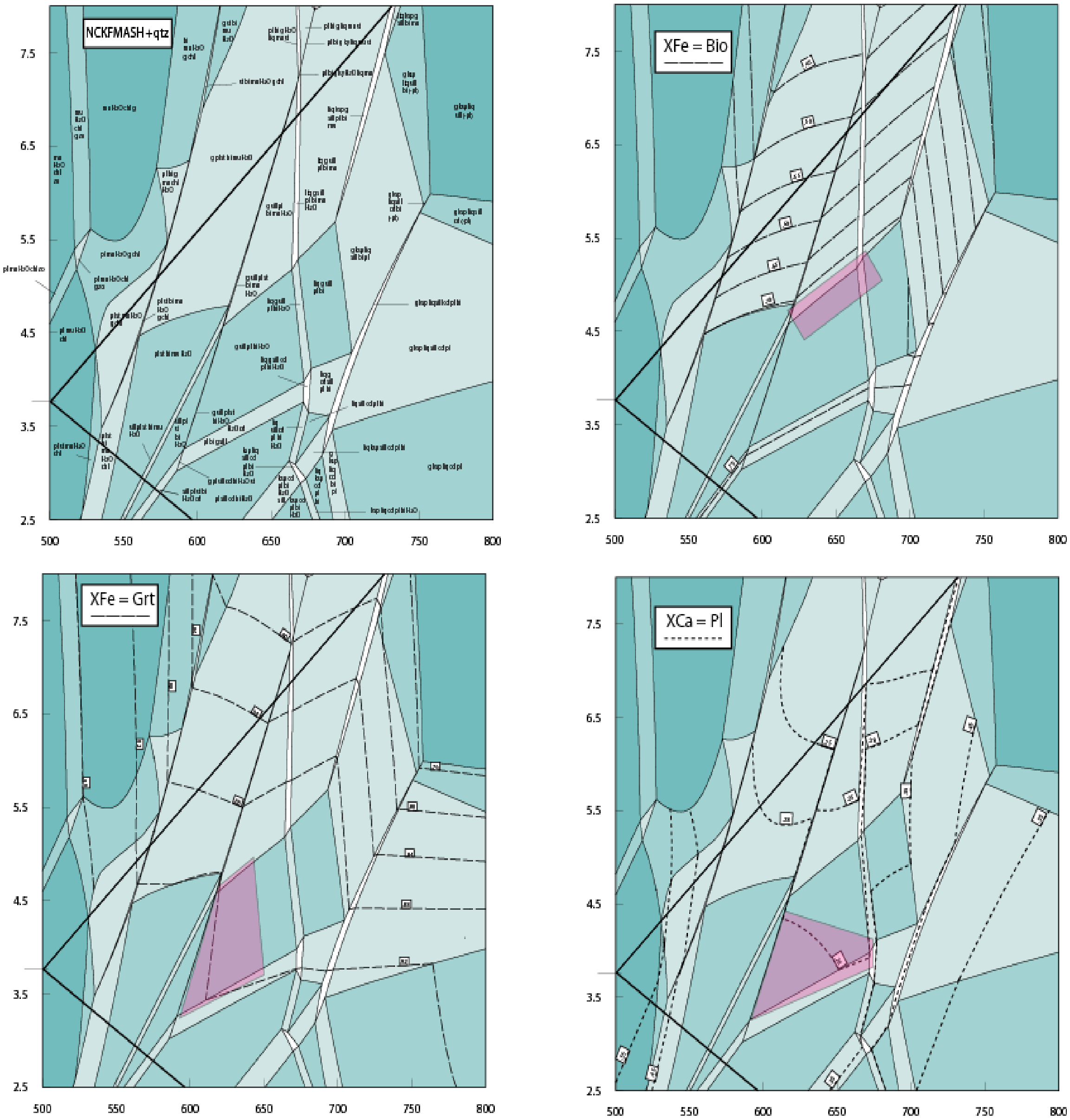

Figure 6-8. NCKFMASH pseudosection contoured for biotite, garnet, and plagioclase, respectively. Areas highlighted in pink show approximate area of where microprobe data corresponds on each contoured pseudosection.

plagioclase compositions of X_{An}^{Pl} =.25-.35.

Biotite isopleths range from X_{Fe} =.45 -.75 and are mainly confined to the center of the diagram, as biotite enters mineral assemblages at 530°C and leaves the system at around 750°C. Iron content in biotite is highest at low pressures and steadily decreases with an increase of pressure. Biotite isopleths X_{Fe} =.70 and X_{Fe} =.75 straddle the peak mineral assemblage. As the peak mineral assemblage field has mean X_{Fe} =.73, this isopleth would run in between the X_{Fe} =.70 and X_{Fe} =.75 passing through the field.

Garnet enters the system at around 550°C with the maximum X_{Fe} content of X_{Fe} =.96. With increased pressures and temperatures iron content decreases, with pressure more of a control than temperature. The garnet isopleth X_{Fe} =.92, which corresponds to the mean averaged garnet composition based on probe data, is vertical and sits on the lower end of the temperature field of the peak metamorphic mineral assemblage (Figure 6-8). As garnet grows and modal proportions increase, plagioclase must break down and become more albitic (Spear, 1993). This is consistent with the THERMOCALC information, where with a modal increase in garnet plagioclase composition decreases its calcium content.

Ideally isopleths of garnet, biotite, and plagioclase would all intersect in the equilibrium mineral assemblage field at a point, resulting in a precise temperature and pressure of formation. However, realistically metamorphic rocks reach equilibrium conditions over a range of pressures and temperatures indicating that phase isopleths would not necessarily intersect but lie close to one another, which is observed on the contoured pseudosection. Based on the equilibrium mineral assemblage Bio + Grt + Sill

+ Qtz + Plag, *P-T* is restricted to 3.3-5.3 kbars and 590-665°C. Garnet, plagioclase, and biotite isopleths all intersect this field.

Average Pressure-Temperature

Mineral compositions can be sensitive indicators of *P-T* conditions and thus mineral chemistry is key to geothermobarometry. End member activities calculated in AX from rocks MTAF13 and MTA15c were imported into THERMOCALC to estimate the pressure-temperature regime for which they formed based on their modal mineral assemblage. Table 6-3 shows AX calculated end member activities and subsequent THERMOCALC Average Pressure-Temperature results using average plagioclase, garnet, and biotite compositions. Two sets of results are presented, one with muscovite included and one with muscovite omitted. Sample MTAF13 yielded higher pressures and lower temperatures (with a stronger correlation and smaller errors) than sample MTA15c when muscovite was not included as a stable phase in the calculations. *P-T* results for MTAF13 are 534 ± 84°C and 5.13 ± 1.24 kbars. MTA15c resulted in a temperature of 603 ± 106°C and a pressure of 3.56 ± 1.78 kbars. Based on petrographic observations, sample MTA15c contains more muscovite that appears to be in equilibrium with the peak mineral assemblage compared to sample MTAF13. When muscovite is included in THERMOCALC average pressure-temperature calculations differences between the two results are negligible with *P-T* for MTAF13 at 539 ± 70°C at 4.8 ± 0.8 kbar and 567 ± 70°C at 4.4 ± 0.9 kbar for MTA15c. A slight decrease in pressure (.33 kbars) occurs in MTAF13 when muscovite is incorporated into the calculations; however results are within error of one other. With muscovite included, sample MTA15c decreases in

Table 6-3. AX calculated end-member activities and subsequent THERMOCALC Average Pressure-Temperature results.

Sample	MTAF13	MTAF13 with muscovite	MTA15c	MTAF15c with muscovite
Activities	at 650°C	at 650°C	at 650°C	at 650°C
Garnet	mean	mean	mean	mean
py	0.000460	0.000460	0.000380	0.000380
gr	0.000057	0.000057	0.000014	0.000014
spss	0.000390	0.000390	0.000081	0.000081
alm	0.550000	0.550000	0.630000	0.630000
Biotite	mean	mean	mean	mean
phl	0.009600	0.009600	0.009600	0.009600
ann	0.130000	0.130000	0.130000	0.130000
east	0.015000	0.015000	0.015000	0.015000
Plagioclase	mean	mean	mean	mean
an	0.300000	0.300000	0.300000	0.300000
ab	0.800000	0.800000	0.800000	0.800000
Muscovite		mean		mean
mu	-	0.780000	-	0.780000
pa	-	0.370000	-	0.370000
Results				
aH2O	1	1	1	1
T°C	534	539	603	567
s.d.(T)	84	70	106	79
P kbar	5.13	4.8	3.56	4.41
s.d.(P)	1.24	0.81	1.78	0.9
correl.	0.82	0.85	0.64	0.8

temperature by 36°C and increases in pressure by ~ 1 kbar with almost half of the error (.9 kbars), bringing its results closer to MTAF13. Excel was used to plot points on the error ellipses for the average *P-T* determinations using the Holland and Powell (1990) program and dataset with correlated uncertainties (Waters, 2008). Figure 6-9 shows calculated error ellipses on the pseudosection.

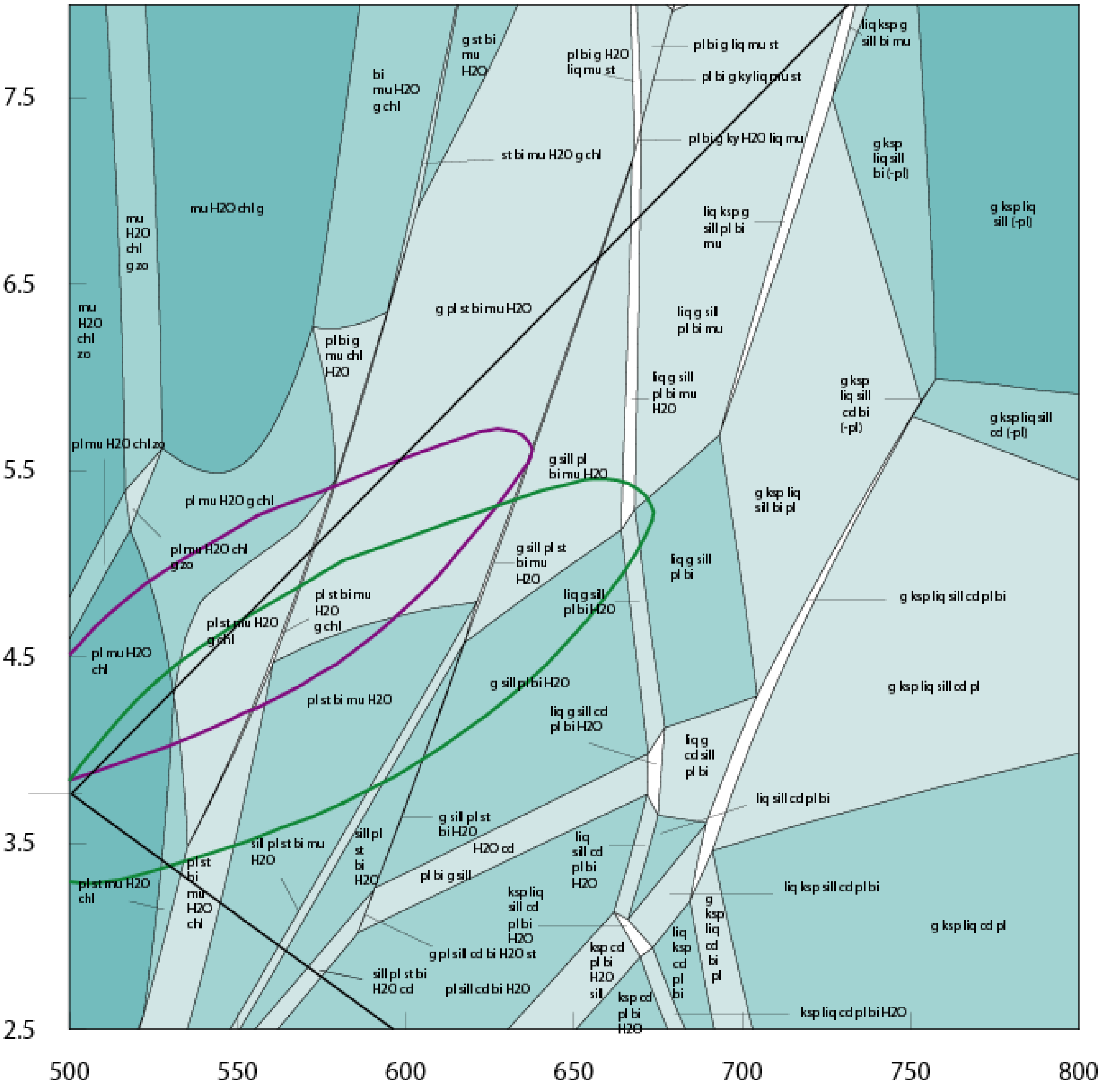

Figure 6-9. P-T ellipses from THERMOCALC Average Pressure-Temperature calculations with muscovite incorporated as an end-member. Green ellipse corresponds to MTA15c and purple ellipse corresponds to MTA13. These calculations contain inherently large errors and are used only as an estimate for metamorphic conditions.

Independent reactions were calculated in THERMOCALC to determine average *P*-*T* conditions. Both thermometer and barometer equations contain uncertainties that are a function of calculated mineral end member activities, thermodynamic data, and microprobe analyses, resulting in errors correlating to the calculated *P*-*T* (Grice, 2006; Holland and Powell, 1994). There is an inferred displacement of the equilibrium to correspond within the *P*-*T* of formation which is chiefly accomplished by altering the end members of minerals in proportion to their uncertainties (Powell and Holland, 1994). This results in the equilibrium shifting in a highly correlated, constrained way as the equilibrium involve overlapping subsets of the end-members (Powell and Holland, 1994). The four independent reactions acting as the barometer and thermometer for MTAF13, when muscovite was included as an end member in calculations, are, respectively:

1. annite + quartz + 2 sillimanite = almandine + muscovite
2. pyrope + 2 grossular + 3 eastonite + 6 quartz = 3 phlogopite + 6 anorthite
3. grossular + 3 eastonite + 6 quartz = 2 phlogopite + 3 anorthite + muscovite
4. 2 phlogopite + 5 annite + 12 sillimanite = 5 almandine + 3 eastonite + 4 muscovite

and

1. 7 phlogopite + 12 sillimanite = 5 pyrope + 3 eastonite + 4 muscovite
2. 3 phlogopite + 4 sillimanite = pyrope + 3 eastonite + 4 quartz
3. annite + quartz + 2 sillimanite = almandine + muscovite
4. 2 grossular + 3 almandine + 3 eastonite + 6 quartz = 2 pyrope + 3 annite + 6 anorthite

Geothermobarometry equations calculated in THERMOCALC from average *P*-*T* for

MTA15c and MTAF13, excluding muscovite, can be found in Appendix C. Calculations in Average Pressure-Temperature mode in THERMOCALC are quick, do not give equilibrium mineral assemblages, and usually contain large errors. However, it is a viable method to check against the inferred equilibrium mineral assemblage based on pseudosection interpretation.

P-T Evolution

Footwall rocks of the Anaconda metamorphic core complex evolved along a clockwise *P-T* path that passed through chlorite, staurolite, and possibly andalusite stability fields (Figure 6-10). These phases are not observed in thin section, as they have long since reacted away. A plethora of sillimanite occurs within footwall rocks as growth of this mineral occurred throughout the evolution of the rocks. Prograde, peak, and post-peak sillimanite within samples indicated prolonged time spent in sillimanite stability. Sample MTAF13 is a melt bearing rock, indicating that maximum temperature rose above the solidus. The position of the solidus is a function of each individual bulk rock's composition, making it conceivable that some rocks did not melt. Potassium feldspar is not associated with this sample indicating that temperatures were not hot enough to reach potassium feldspar stability. MTAF13 reached amphibolite facies metamorphism and equilibrated at temperatures just below or at the solidus.

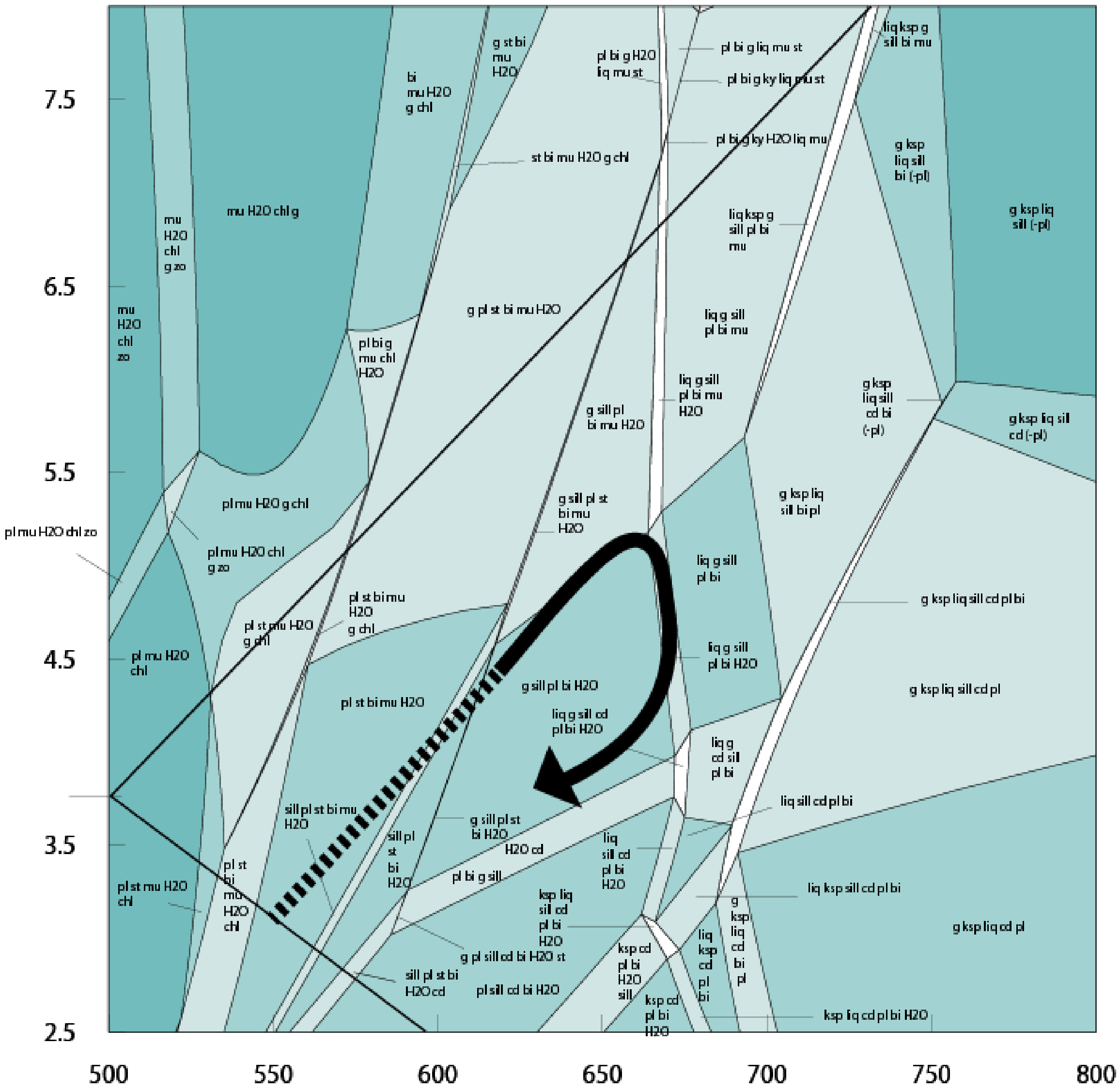

Figure 6-10. NCKFMASH pseudosection with arrow indicating *P-T* evolution of footwall rocks. Dashed line indicates inferred path. Note that arrow crosses into muscovite and melt stability fields.

CHAPTER 7

DISCUSSION

Introduction

Regional Cretaceous compressional forces were the driving mechanism in metamorphosing pelites to amphibolite schists in the Anaconda metamorphic core complex footwall. Unlike other North American Cordilleran core complexes, the AMCC shows little evidence of replacement or reequilibration of minerals, indicating only one metamorphic event has been recorded. The AMCC is also unique as minerals equilibrated at pressures substantially less than those found in northern core complexes (Table 2-1). Peak metamorphism in the AMCC occurred at 79 Ma (Foster et al., 2007; Grice, 2006; Grice et al, 2005; Kalakay et al., 2004). As is the case in many core complexes, footwall rocks of the AMCC have been intruded by plutonic bodies during extension. Recent thermobarometry studies on footwall rocks by Grice (2006) resulted in higher temperatures, by almost 100°C, than what was found in this study. The most likely cause of this is that the chosen rock for thermobarometry was in close proximity to a Cretaceous quartz diorite sill.

AMCC Thermobarometry

The equilibrium metamorphic assemblage of the AMCC footwall is Bio + Grt + Sill + Qtz + Plag + Mus. Microprobe analyses on the modeled pseudosection for MTAF13 indicates a peak assemblage of Bio + Grt + Sill + Qtz + Plag. Both the garnet and plagioclase isopleths run through this field while the two biotite isopleths X_{Fe} =.70 and X_{Fe} =.75 straddle the mineral assemblage field which has X_{Fe} =.73. Petrographic analysis indicates that muscovite is in equilibrium with the peak mineral assemblage and appears to have grown throughout the history of the rock. Plagioclase contains inclusions of muscovite suggesting early growth, while very little muscovite is in equilibrium with garnet, suggesting later growth of the mineral. The trivariant mineral assemblage Bio + Grt + Sill + Qtz + Plag + H2O + Mus sits right above the peak mineral assemblage field according to the derived pseudosection. As muscovite is in equilibrium in this assemblage, it is likely that the zone of equilibration extends into this field. Many fields that the rock passed through to reach peak metamorphism contain muscovite, which explains much of the early growth of the mineral. The presence of leucosome indicates that temperatures and pressures where high enough for localized *in situ* melting. Leucosome is not prevalent and occurs as small, tight lenses. The divariant field directly above and to the right of the peak assemblage is Bio + Grt + Sill + Qtz + Plag + H2O + Mus + Melt, suggesting that the rock crossed into these conditions at its maximum temperatures.

Pseudosection modeling and petrographic analysis of sample MTAF13 yield very similar results. Realistically, lines on a pseudosection are not sharp boundaries, due to errors on the activity models, and should rather be considered as bands. Microprobe analysis indicates peak metamorphism to have a mineral assemblage of Bio + Grt + Sill + Qtz + Plag. When lines are considered as bands instead of discrete lines the peak assemblage incorporates some muscovite into the system as is observed petrographically. The probable reason for the slight variations in observations versus modeling is that the modeled system is a simplification. For example, it does not incorporate titanium, manganese, or Fe^{3+} into the system and assumes a pure H_2O fluid.

Previous work by Grice (2006) suggests peak metamorphism of AMCC rocks, located away from quartz diorite sills, is Cd + Bio + Grt + Kspar + Plag + Qtz + Sill. A major difference in this conclusion of assemblage is the type of feldspar present. Potassium feldspar found in footwall rocks by Grice (2006) could suggest that samples considered to not be effected by contact metamorphism from granitic sills were in fact still too close and were thermally altered by the intrusions.

THERMOCALC modeling in average *P-T* of footwall rocks by Grice (2006) indicate peak metamorphic conditions were reached at 3.8 ± 1.8 kbar and 657 ± 176°C based on the AX calculated end-member phases Grt + Bio + Plag + Cd . If potassium feldspar was in fact in equilibrium in this metapelite as petrographic analysis by Grice (2006) indicated, it should have been incorporated into THERMOCALC as an end-member phase. As it was not, results are not considered reliable as the mineral chemistry of the rock is not correlated with petrographic observations. This rock was sampled .4 km distance from a quartz diorite sill, which most likely underwent contact metamorphism. The presence of cordierite, potassium feldspar, and melt are all indicators that this rock experienced higher temperatures (and pressures), as modeling suggests, than rocks in this study. Average *P-T* calculations for sample MTAF13 in this study yields P-T conditions of 4.8 ± 0.8 kbar and 539 ± 70°C (Table 6-3). Errors on the latter results are inherently smaller as average pressure and average temperature where calculated individually, allowing for a separate set of independent reactions to be used as the thermometer and barometer. Thermobarometry in this study is therefore interpreted to more accurately reflect the true regional metamorphic conditions of AMCC footwall rocks, as overprint textures, rims on garnets, and other typical indicators of polyphase metamorphism are not observed in the rocks selected for this study. Rapid exhumation of AMCC footwall rocks is considered to be the primary reason retrograde affects are minimal.

CORDILLERAN COMPLEXES

Foster et al. (2007) has concluded that Eocene metamorphic core complexes in the North American Cordilleran are linked by transfer faults in the Lewis and Clark fault zone (Figure 3-3). The LCL is also thought to have accommodated extension along the southern boundaries of the Shuswap, Okanagan, and Kettle (the latter two are domes within the Shuswap) metamorphic core complexes which extend west-north-west into southern Canada (Foster et al., 2007). Differential extension along the LCL is thought to be the result of the Kula, Farallon, and Pacific plates moving northward at the plate boundary (Foster et al., 2007). It is theorized that since these northern Cordilleran core complexes show striking similarities in the timing of exhumation and extension that they have all been subjected to comparable metamorphic pressures and temperatures (Foster et al., 2007*)*. This study has clearly defined the *P-T* evolution of AMCC footwall rocks. It shows that the AMCC has exhumed rocks of much shallower crustal levels in comparison to Bitterroot, Clearwater, Priest River, and Shuswap metamorphic core complexes. Crustal levels exposed in the AMCC are similar to pressures found in the Pioneer MCC at 3.5 kbars (Silverberg, 1990). These shallow pressures may be directly related to the width of the complexes, which are both relatively narrow (Table 2-1).

South of the LCL lies the Bitterroot and Anaconda metamorphic core complexes. The Bitterroot metamorphic core complex (Bitterroot MCC) has been extensively studied, although deciphering its history has been more difficult as it has been extensively overprinted during Tertiary extension. Conventional thermobarometry was used to calculate peak metamorphic conditions of the M2 event, using rim analyses, which yielded a *P-T* of 6-8 kbar and 675-725°C (House et al., 1997; Foster et al., 2001). Extensional tectonics that exhumed upper amphibolite grade rocks in the Bitterroot MCC began around 59 Ma (Table 2-1) (Foster et al., 2001; Hodges and Applegate, 1993; House and Hodges, 1994; Foster and Fanning, 1997).

The Prichard Formation is the protolith for metapelites in both the Bitterroot and Anaconda MCCs, and both typically contain the same mineral assemblages. Exception lies in that sillimanite may overprint kyanite in the BMCC with thermobarometers recording equilibration with kyanite (House et al., 1997). The aluminosilicate kyanite rather than sillimanite would be in concordance with calculated *P-T* conditions for Bitterroot MCC metapelites, as it is indicative of higher pressures. Garnet amphibolites in the Bitterroot MCC yielded similar temperatures as the metapelites but with pressures around 5-6 kbars (House et al., 1997). House et al. (1997) hypothesized that the lower pressures in the garnet amphibolites were due to errors in the solution models used in thermobarometry calculations, or that they equilibrated at lower pressures than the surrounding metapelites, perhaps recording isothermal decompression following peak metamorphism. Polymetamorphism in the Bitterroot and Boehls Butte (Clearwater) metamorphic core complex makes it harder to ascertain peak metamorphic assemblages related to M2 events as mineral assemblages are often obscured. Thermobarometry data from the Clearwater metamorphic core complex (Clearwater MCC) is consistent with the findings in the Bitterroot MCC for the M2 event, suggesting that regional upper-amphibolite facies metamorphism was laterally extensive (House, 1997).

The Clearwater MCC was exhumed within a transtensional pull-apart zone in the LCL around 52-46 Ma (Foster et. al., 2007; Doughty, 2002). Middle Eocene dextral movement along this fault is responsible for tectonic unroofing (Doughty, 2002). Footwall rocks in the Clearwater MCC are also composed of the lower Belt Supergroup Prichard Formation. Grover et al. (1992) concluded that M2 events occurred at 8-11 kbars and 575-750°C (Foster et al., 2007; Doughty et al., 2006). The mineral assemblage of these amphibolite grade rocks is Grt + Bio + Mus + Pl + Qtz + Als (Grover et al., 1992). All three aluminosilicates are found in aluminous schists at Boehls Butte; however kyanite is the dominant aluminosilicate (Grover et al., 1992). Occurrence of fibrolite is considered to be the result of *P-T* conditions crossing into the sillimanite field after peak metamorphism (Carey et al., 1992). Clearwater MCC amphibolites also contain evidence of M3 isothermal decompression in which rocks equilibrated at 4-6 kbars (Grover et al., 1992). Although pressures for the M3 event are more comparable to peak metamorphic conditions in the AMCC, AMCC rocks contain no evidence of overprinting as Clearwater MCC rocks clearly do with cordierite + corundum and cordierite + hercynite decompression reaction textures (Grover et al., 1992). The three metamorphic events evident in the Clearwater and Bitterroot MCCs correspond to an early event whose metamorphic history is hard to decipher, main phase metamorphism contemporaneous with initial deep seated intrusions of the Idaho batholith during compressional events of the Cretaceous Sevier orogeny, and rapid isothermal decompression associated with extension during tectonic denudation of the thickened Sevier hinterland (Grover et al., 1992; Carey et al., 1992; Lang and Rice, 1985). Recent Lu-Hf geochronologic dating on garnet amphibolites in the Clearwater MCC has provided evidence of a 1.0 Ga metamorphic event, although significance of this early event is poorly understood (Grant et al., 2004).

Northwest of the Clearwater MCC lies the Priest River metamorphic core complex (Priest River MCC). This complex exhibits great tectonic exhumation, in which Precambrian basement rock is exposed. This could be the result that unroofing occurred by a pair of east and west verging detachment faults (Foster et al., 2007; Doughty and Price, 1999). Three large tectonic blocks comprise the Priest River MCC, each differing in grades of metamorphism (Doughty and Price, 1999). The Prichard Formation, again, is the protolith for metapelitic rocks in this complex (Foster et al., 2007; Doughty and Price, 1999; Doughty and Price, 2000). The core of the Spokane dome (part of the Priest River's footwall) contains a peak assemblage of Sill + Ky + Ortho + Ru + Grt with geothermobarometry suggesting metamorphic conditions in the range of 7-11 kbars and 770-930°C (Doughty and Price, 1999). Lower grades of metamorphism occur throughout the complex near faults and plutons (Doughty and Price, 1999). Peak metamorphism in the Priest River MCC occurred around 86-72 Ma (Doughty et al., 1998; Doughty and Chamberlain, 2004) with the onset of extension occurring at 55 Ma (Doughty and Price, 1999).

The very complicated Shuswap metamorphic core complex (Shuswap MCC) lies to the northwest of the Priest River MCC in Canada, with its terrane extending down in to Washington, US (Brown and Read, 1983). The Shuswap MCC is a parautochthonous basement appearing in tectonic windows such as the Monashee and Okanagan complexes (Lorencak et al., 2001; Eyal et al., 2006). These domal culminations expose high-grade, deeply exhumed metamorphic and plutonic rock (Johnson, 2006). A north-south trending detachment fault bounds the Shuswap MCC. Juxtaposed across the fault are upper amphibolite facies rocks in the footwall and unmetamorphosed rocks in the hanging wall (Lorencak et al., 2001). Deepest exposed levels of the Shuswap MCC occur in the Monashee complex which is cored by Paleoproterozoic basement (Johnson, 2006). Peak metamorphic mineral assemblage within the mylonitic footwall is Grt + Sill + Kspar + Bio + Plag + Qtz + Melt (Johnson, 2006). Peak metamorphic conditions were reached around 6-9 kbars at 620-820°C (Vanderhaeghe et al., 2003). These temperatures and pressures are consistent with peak metamorphic conditions found in the Valhalla metamorphic core complex. This domal culmination lies on the eastern exposed edge of the Shuswap MCC and reached upper amphibolite facies at around 8 kbars and 800°C (Spear, 2004; Carr and Simony, 2002; Schaubs and Carr, 1997). Peak mineral assemblage present in pelitic schists is Grt + Sill + Kspar + Melt (Schaubs and Carr, 1998). M2 metamorphic conditions were reached during crustal shortening and thickening in the Cretaceous (Carr and Simony, 2002) around 60 Ma in the Shuswap and Valhalla MCCs just before extension started occurring along detachment faults around 58Ma (Spear, 2004; Vanderhaeghe et al., 2003).

Onset of extension within core complexes north of the Snake River Plain has been hard to decipher due to retrograde affects produced during exhumation. As only one metamorphic event is observed petrographically within the AMCC, these metapelites are ideal for geochronology. Preliminary geochronology on the AMCC suggests two clearly defined events for metamorphism and extension, based on granitic intrusions. Dating zircon and monzonite within footwall rocks would further constrain the exact timing of metamorphism. If the timing of metamorphism is in fact not synchronous with extension, new insight into the formation of the metamorphic core complexes would be revealed.

Geothermobarometry on North American Cordilleran metamorphic core complexes indicate upper amphibolite facies metamorphism was reached during the Cretaceous due to crustal shortening and thickening of the foreland. This study shows that the AMCC exposes the shallowest crustal levels in comparison to the Bitterroot, Clearwater, Priest River, Shuswap MCCs (Table 2-1). While the AMCC appears to have reached peak metamorphism and was exhumed around the same time as other regional core complexes, the conditions of peak metamorphism are distinctly different. The lower end of the temperature spectrum recorded in the Clearwater MCC corresponds the closest to that found in the AMCC, however temperatures at the high end of the spectrum for Clearwater MCC rocks, around 750°C, are significantly greater than what is found in the AMCC at ~665°C. Pressures recorded in the AMCC are about half of what is recorded in other Cordilleran core complexes. Shallower crustal exposures than that found in the AMCC have not been observed. Developments in numerical modeling of MCC development may ultimately provide insight into the differences between the various regional core complexes.

The process of gravity-driven flow of orogenic crust due to its own weight was proposed to explain zones of surface extension in active convergent regions (Coney and Harms, 1984; Rey et al., 2001). Gravitational collapse is currently the most accepted theory for the formation of metamorphic core complexes. Since the 1980's when gravitational flow of orogenic crust was first introduced, scientists have been refining the assessment that gravitational potential energy could drive tectonic process from balancing forces in the crust and lithosphere (Rey et al., 2001). When a positive perturbation is applied to the crust, causing an excess in potential energy, the gravitational collapse is divergent with particles moving away from the deformed domain (Rey et al., 2001).

Three types of divergent settings are possible, however only two show surface expressions. The first type of divergent collapse is described by gravitational sliding of upper crust away from thickened regions by extensional detachments and deep thrust faults that connect to the foreland (Rey et al., 2001). The second model consists of the lower-crust decoupling from the upper-crust (Rey et al., 2001). Decoupling causes horizontal spreading of a low-viscosity region, leading to thinning of the orogenic crust and thickening of surrounding crust (Rey et al., 2001). Combining both of these models produces the third model. Upper crustal material is moved away from the thickened regions through faulting, while the ductile crust moves upward to fill the space beneath the detachments and towards the foreland which endures thickening (Rey et al., 2001). Evidence that supports this third model is: 1) extension and thinning synchronous with thrusting and thickening in the foreland, 2) continuity between faults in thickened regions and thrust at the foreland, and 3) ductile deformation beneath the detachment as evidenced by low-pressure, high-temperature metamorphism (Rey et al., 2001).

New modeling by Bendick and Baldwin (personal comm., 2008) may provide insight into the depth of crustal exposure in core complexes relative to their width, suggesting that the wider the core complex the deeper they will be exhumed. Their preliminary model shows if accreted terrains are pushed up and over the craton a core develops beneath the thickened crust. Gravity collapse of the thickened crust results in a vertical rise of the core with a low angle normal fault expressed at the surface (personal comm., 2008). The difference in crustal exposure in North American Cordilleran metamorphic core complexes could be a local affect of craton thickness (Bendick personal comm., 2008). Only a 10% difference in thickness would be required to produce the depths of exposure between the Bitterroot MCC (6-8 kbars) and the Anaconda MCC (3-5 kbars) (Bendick personal comm., 2008).

CHAPTER 8

CONCLUSION

Peak metamorphic conditions in the Anaconda metamorphic core complex were reached around 79 Ma (Grice, 2006) at conditions of 3.3-5.3 kbar and 590-665°C, recording significantly lower peak metamorphic conditions than Cordilleran metamorphic core complexes north of it (Table 2-1). The amount of exhumation in the AMCC is not more that ~5 kbars (or about 15 km depth) since early Eocene time, which is almost half of the exhumation of the northeastern part of the Bitterroot (MCC), the closest neighboring core complex (Foster et al., 2007).

Peak mineral equilibria of the metapelitic Prichard Formation in the AMCC footwall is Grt + Plag + Sill + Bio + Qtz + Mus. Average pelites pass through the reaction St + Ms + Qtz ↔ Bt + Grt + Sill + Pl + H_2O and with increasing *P-T* Grt + Ms + Qtz ↔ Bt + Sill + Pl + H_2O (Johnson et al., 2003). These equations account for the lack of abundant muscovite and small modal amounts of garnet in modeled rocks. Microprobe data confirms the peak mineral assemblage as plagioclase, garnet, and biotite isopleths tightly straddle the field or pass through it on the constructed pseudosection (Figure 6-8). Average pressure-temperature calculations in THERMOCALC also verify peak *P-T* with results of 539 ± 70°C at 4.8 ± 0.8 kbar. The results of this study are robust due to the fact that only one metamorphic event is observed in the rocks and microprobe data validates the chosen equilibrium mineral assemblage based on petrographic observations.

The findings of this study improve the understanding of orogens, as it provides a detailed analysis on metamorphic rocks affected by Sevier compressional events. The significantly lower *P*-*T* conditions at which footwall rocks of the Anaconda metamorphic core complex equilibrated at in comparison to complexes north of it afford insight into the tectonic processes involved during convergence. Models for metamorphic core complex formation are continuously being developed, making it necessary to have a solid understanding of the *P*-*T* evolution of the rocks within them.

APPENDIX A

THIN SECTION DESCRIPTIONS

Pelitic Layer

Sample: MTA15a, MTA15b, MTA15c

These three slides are compositionally and almost modally identical. The presence of multiple garnets is the key difference between these three pelitic slides and the other pelitic samples. Average composition of garnet bearing metapelites is shown in Table C-1. The equilibrium mineral assemblage is Grt + Plag + Bio + Sill + Qtz + Mus.

Table C-1. Estimated averaged composition for garnet bearing metapelites.

Phase	Percent
Quartz	30
Sillimanite	25
Biotite	30
Feldspar	5
Muscovite	5
Garnet	<5

Accessory phases include opaques, apatite, and zircon and/or monazite. Garnets are small >1mm, subidoblastic, and contain many inclusions of quartz, feldspar, and biotite. Garnets are typically partially encased by biotite foliation and in contact with quartz and sillimanite. Sillimanite in contact with garnet usually occurs as xenoblastic grains with some fibrolite overgrowth. Some minor retrograde white mica occurs between the boundary of garnet and biotite. Garnet is fractured with veins of biotite. Quartz grains in contact with garnets are small with cataclastic texture which fades into larger grains with distance from the garnet.

A strong foliation is exhibited in these rocks. Biotite comprises most of the foliations with some intermixed fibrolite. Radiations halos can be found within biotite grains. Quartz grains within foliation and are usually elongated in the direction of the fabric. Quartz exhibits undulatory extinction with irregular sutured boundaries.

Sillimanite is prolific throughout the slides, occurring as large prismatic grains, xenoblastic grains, or small slender needles. Needles of sillimanite occur as inclusions in all other phases. Fibrolite occurs sparingly within biotite foliation bands and overprints larger xenoblastic and idioblastic sillimanite grains. These larger prismatic grains can be riddled with biotite overgrowth as well. Sillimanite grains range in size from tiny needles to < 3mm.

Leucosome is not largely present in these three thin-sections. Prograde muscovite grains ~2 % are found within matrix biotite. Larger up to 1mm grains are present and appear to be more indicative of late phase growth. Lesser white mica (phengite) is found around some garnet-biotite contacts.

Plagioclase is rare, usually only present as small grains. When present it occurs with muscovite and quartz, which could indicate secondary growth. Very few large, up to 1mm, idioblastic grains are found sparingly through the slides.

Sample: MTAF1, MTA4, MTA5, MTA8, MTA9B, MTA11, MTA13, MTA17, MTA2,
MTA3, MTA6, MTA9, MTA12, MTA14, MTA16

These slides represent non-garnet bearing metapelites of the Prichard Formation within the footwall of the AMCC. They generally exhibit the same metamorphic characteristics and are mineralogically similar, although modal amounts of each mineral varies from slide to slide. Table C-2 shows the composition variability found within these metapelites. Grains are fine grained and contain abundant sillimanite and biotite. Three slides are outliers in this group as they contain minerals not found in other non-garnet bearing metapelite samples.

Table C-2. Low, average, and high percentages of phases present in non-garnet bearing pelites.

Phase	**Average**	**Low**	**High**
Quartz	30%	10%	40%
Sillimanite	25%	10%	50%
Biotite	25%	15%	35%
Muscovite	5%	>1%	12%
Feldspar	10%	2%	20%

Equilibrium assemblage in these slides appears to be Plag + Bio + Sill + Qtz ± Mus which was determined by textural relationships. Accessory phases include opaques, apatite, and zircon and/or monazite. Biotite and fibrolite compose the metamorphic foliation. Radiation halos are found within biotite. Sillimanite is abundant and appears in four crystal forms. Slender needles are abundant and occur as inclusions in all phases. Primary fibrolite tends to comprise foliation while secondary fibrolite overprints some feldspar and other sillimanite crystals. Xenoblastic sillimanite grains are present and are usually fractured. Biotite, sillimanite needles, and opaque inclusions are consistently found within larger, prismatic grains of sillimanite. Biotite and secondary fibrolite tend to overgrow these grains. Quartz grains vary in size and show undulatory extinction with irregular, sutured boundaries. Within foliation bands, quartz is typically elongated in the direction of the fabric. Feldspar occurs as large ≥3 mm idioblastic grains that can contain inclusions of biotite, sillimanite needles, quartz, and rarer muscovite.

Few large muscovite grains are present but appear to be due to late phase growth rather than part of the peak metamorphic assemblage, as these grains crosscut foliation. Minor prograde muscovite is intergrown with matrix biotite, along with few, small ≤ 1mm laths of muscovite occurring in plagioclase, indicating equilibrium growth of these three minerals at some point during prograde evolution. Muscovite also occurs in leucosome. Leucosome consists of idiobalstic quartz, plagioclase, muscovite and lesser, large ≥ 3 mm potassium feldspar grains.

Slide MTA5 is the only slide in this series that contains garnet. Garnet is rare, composing less than 2% of the slide and is no larger than 500 μm. Staurolite is present in slides MTA11 and MTA16 as one and two grains, respectively. These large grains are subidoiblastic, contain inclusions of sillimanite needles, and appear to be zoned.

Quartz Rich Layer

Sample: MTA3b, MTA7

These two slides represent quartz rich horizons within the Prichard Formation. These layers are defined by >50% quartz and have an ultra fine grained texture. Table C-3 shows estimated modal proportions of phases present. Quartz is the main constituent which is strained and displays undulatory extinction and exhibits irregular, sutured boundaries. Garnet present in these two slides are extremely altered and contain inclusions of quartz, feldspar, and biotite. Wherever garnet is biotite is in contact with it. Biotite is the only mica present except for a few laths of chlorite where biotite is breaking down. Chlorite makes up less than 1% of the slides. Biotite laths are slightly aligned in the development of foliation. Sillimanite needles are sparse throughout the slide. Opaques are present.

Table C-3. Estimated composition of quartz rich rocks.

	MTA3B	**MTA7**
Phase	**Percentage**	**Percentage**
Quartz	65	55
Biotite	20	25
Feldspar	10	15
Garnet	>5	>5

Mafic Layer

Sample: MTA10

Mafic horizons of the Prichard Formation are distinct in thin section as amphiboles are common. This rock is thought to be the result of an old, deformed sill that was intruded into the protolith during some point of its evolution. Table C-4 show estimated composition of this rock. Opaques and rutile are common accessory phases.

Table C-4. Estimated composition of mafic rock MTA10.

MTA10	
Phase	**Percentage**
Quartz	45
Pyroxene	15
Amphibole	15
Feldspar	20
Garnet	5
Biotite	2

Chlorite is present as sub-idioblastic grains. Hornblende occurs as small idioblastic grains. Hornblende is less common than calcic clinoamphibole, which appears as small, idioblastic ~ ≤ 500 μm grains that are unaltered. Quartz grains are large with undulatory extinction and irregular, sutured boundaries. Biotite is present as small random grains. Quartz ≥ 2mm grains contain sparse inclusions of biotite and rutile. Plagioclase is present as ≤ 500 μm idioblastic grain and occurs in clusters with amphiboles. Large garnet ≤ 1 mm grains are prevalent through out the slide. Garnet contains inclusions of quartz.

APPENDIX B

MICROPROBE RESULTS

Table B-1. Microprobe analyses of garnet.

Analyses	MgO	Al_2O_3	SiO2	FeO	MnO	TiO_2	CaO	Total
Garnet Core								
MTAF13 map2 pt19	1.99	21.03	36.71	36.45	2.67	0.01	1.36	100.22
MTAF13 map2 pt20	1.97	20.99	36.61	36.31	2.57	0.02	1.40	99.87
MTAF13 map2 pt21	1.85	20.94	36.65	36.19	2.95	0.01	1.13	99.73
MTAF13 map2 pt23	2.16	20.98	36.76	36.08	2.63	0.01	1.38	100.00
MTAF13 map2 pt24	1.88	20.96	36.67	35.92	3.36	0.02	1.12	99.93
MTAF13 map2 pt25	2.11	21.01	36.57	36.17	2.68	0.00	1.46	100.00
MTAF13 map2 pt26	1.99	20.94	36.68	36.25	2.64	0.00	1.32	99.82
MTAF13 map2 pt27	1.95	20.83	36.95	36.12	2.83	0.00	1.40	100.08
MTAF13 map2 pt28	1.95	21.19	36.34	35.52	2.85	0.02	1.44	99.31
MTAF13 map2 pt29	1.92	20.92	36.53	35.96	2.66	0.01	1.34	99.33
MTAF13 map2 pt30	2.03	20.98	36.28	36.28	2.85	0.03	1.13	99.58
MTAF13 map1 pt33	1.86	20.63	36.05	36.80	2.73	-0.01	1.11	99.17
MTAF13 map1 pt34	1.92	20.50	36.49	37.00	2.65	0.02	1.13	99.71
MTAF13 map1 pt35	1.80	20.70	36.91	37.23	2.75	0.04	1.19	100.62
MTAF13 map1 pt36	1.90	20.82	37.01	36.99	2.58	0.02	1.06	100.38
MTAF13 map1 pt37	1.85	20.62	37.17	36.74	3.05	-0.01	1.18	100.60
MTAF13 map1 pt38	1.56	20.89	36.66	36.66	2.84	0.00	1.11	99.72
MTAF13 map1 pt41	1.58	20.87	37.02	36.31	3.43	0.00	1.02	100.24
MTAF13 map1 pt42	1.65	20.65	36.94	35.96	3.09	0.02	1.51	99.83
MTAF13 map1 pt43	1.67	20.94	37.09	36.40	3.16	0.00	1.42	100.68
MTAF13 map1 pt44	1.67	20.71	36.82	35.90	3.41	-0.01	1.03	99.54
MTAF13 map1 pt45	1.47	20.83	37.10	37.14	3.24	0.00	1.05	100.83
MTAF13 map1 pt48	1.61	20.50	36.65	36.02	4.05	0.01	1.56	100.41
MTAF13 map1 pt49	1.49	20.55	36.87	36.19	3.92	0.00	1.34	100.35
MTAF13 map1 pt52	1.46	20.75	36.86	36.44	3.21	0.03	1.01	99.77
MTAF13 map1 pt53	1.71	20.65	36.32	36.21	3.40	0.00	1.25	99.55
MTAF13 map1 pt54	1.47	20.88	37.02	36.81	3.42	0.02	1.05	100.67
MTAF13 map1 pt55	1.48	20.76	37.33	37.29	2.97	-0.01	0.98	100.81
MTAF13 map1 pt56	1.57	20.81	37.16	37.05	3.03	0.04	1.05	100.71
MTAF13 map3 pt58	1.21	20.67	36.07	36.32	3.65	-0.01	1.50	99.42
MTAF13 map3 pt59	1.41	20.62	36.65	36.06	4.12	0.01	1.01	99.89
MTAF13 map3 pt60	1.58	20.72	36.38	36.25	3.99	0.01	0.99	99.92
MTAF13 map3 pt63	1.75	20.60	36.45	36.29	2.97	-0.01	1.42	99.46
MTAF13 map3 pt64	1.51	20.72	36.09	36.01	3.74	0.01	1.22	99.30
MTAF13 map3 pt65	1.38	20.26	35.72	36.43	3.84	0.01	0.95	98.59
MTAF13 map3 pt66	1.23	20.60	35.92	36.53	3.91	0.09	1.00	99.27
MTAF13 map3 pt68	1.74	20.94	36.10	36.31	3.51	0.00	1.12	99.72
MTAF13 map3 pt69	1.77	20.80	36.30	36.87	2.96	0.01	1.19	99.89
MTA15c map1 pt74	1.79	20.99	36.07	38.30	1.58	0.02	0.95	99.69
MTA15c map1 pt75	1.95	21.16	35.77	39.34	1.20	0.02	0.47	99.91
MTA15c map1 pt76	1.83	21.02	36.33	39.07	1.30	0.05	0.46	100.05

Table B-1. continued.

Analyses	**MgO**	**Al$_2$O$_3$**	**SiO2**	**FeO**	**MnO**	**TiO$_2$**	**CaO**	**Total**
MTA15c map1 pt78	1.91	20.75	35.92	39.28	1.24	0.02	0.40	99.53
MTA15c map1 pt80	1.58	20.88	36.25	39.21	1.71	0.01	0.55	100.20
MTA15c map1 pt83	1.66	20.86	36.17	38.94	1.83	0.03	0.52	100.01
MTA15c gt2 pt85	1.49	20.73	36.21	38.55	2.24	0.04	0.57	99.83
MTA15c gt2 pt86	1.65	20.36	35.95	38.73	1.79	0.05	0.59	99.13
MTA15c gt2 pt88	1.65	20.86	36.38	39.07	1.09	0.01	0.60	99.66
MTA15c gt2 pt89	1.88	20.78	36.37	39.42	0.88	0.03	0.59	99.95
MTA15c gt2 pt90	1.95	20.88	36.18	39.53	0.77	0.08	0.58	99.96
MTA15c gt2 pt91	1.90	20.99	36.22	39.45	0.79	0.05	0.57	99.97
MTA15c gt2 pt92	1.91	20.69	36.11	39.39	0.95	0.03	0.58	99.64
MTA15c gt2 pt93	1.80	20.96	36.38	39.13	1.14	0.02	0.76	100.19
MTA15c gt2 pt98	1.74	20.95	36.23	38.76	1.42	0.02	0.95	100.07
MTA15c gt2 pt99	1.55	20.92	36.33	38.57	1.80	0.03	0.94	100.14
MTA15c pt100	1.90	20.96	36.06	38.91	1.21	-0.03	0.57	99.58
MTA15c pt101	1.75	20.76	36.07	38.86	1.51	0.05	0.48	99.48
MTA15c pt104	1.72	21.10	35.75	39.43	1.40	0.02	0.50	99.92
MTA15c pt105	1.81	21.01	36.25	39.59	1.12	0.00	0.52	100.29
MTA15c pt111	1.80	20.85	36.20	38.98	1.26	-0.02	0.65	99.71
Garnet Rim								
MTAF13 map1 pt39	1.40	20.80	36.63	37.18	2.93	0.00	0.98	99.93
MTAF13 map1 pt40	1.28	21.17	37.16	36.73	3.20	-0.01	1.46	100.99
MTAF13 map1 pt47	1.48	21.00	36.88	36.76	3.21	0.01	1.13	100.46
MTAF13 map1 pt50	1.49	20.93	37.15	36.51	3.63	0.02	1.27	101.01
MTAF13 map1 pt51	1.39	20.86	37.27	36.93	2.98	-0.01	1.02	100.45
MTAF13 map3 pt61	1.40	20.55	35.94	36.54	3.24	0.00	1.45	99.11
MTAF13 map3 pt62	1.57	20.60	36.19	36.39	3.77	0.07	1.05	99.64
MTAF13 map3 pt72	1.32	20.83	36.24	36.78	3.22	0.03	1.68	100.10
MTAF13 map2 pt31	1.59	20.90	36.62	36.03	4.00	-0.01	1.15	100.28
MTAF13 map2 pt32	1.51	20.96	36.68	35.66	3.85	0.04	1.16	99.85
MTA15c gt2 pt84	1.34	20.93	36.17	38.22	2.71	0.00	0.67	100.04
MTA15c gt2 pt94	1.64	20.81	36.25	38.90	1.27	0.02	1.00	99.89
MTA15c gt2 pt95	1.37	21.22	36.29	38.56	2.34	0.01	0.53	100.32
MTA15c gt2 pt96	1.27	20.64	36.17	37.97	2.37	0.01	0.96	99.40
MTA15c gt2 pt97	1.35	20.97	36.07	38.22	2.23	0.03	1.00	99.86
MTA15c map1 pt73	1.46	20.64	36.10	37.97	2.28	0.01	0.98	99.43
MTA15c map1 pt81	1.36	20.84	35.68	38.08	2.47	0.01	0.93	99.37
MTA15c map1 pt82	1.32	20.69	36.20	37.49	2.54	-0.01	0.93	99.15
MTA15c pt102	1.17	20.58	36.54	38.15	2.39	0.06	1.09	99.97
MTA15c pt103	0.99	21.03	35.86	37.14	3.28	0.02	1.22	99.53
MTA15c pt106	1.14	20.91	36.04	38.29	2.92	0.05	0.82	100.17
MTA15c pt107	1.11	20.84	35.91	37.82	3.11	0.01	0.63	99.44
MTA15c pt108	0.99	20.96	36.63	36.86	3.51	0.05	1.31	100.31
MTA15c pt109	1.00	20.71	36.49	36.45	3.18	0.07	1.83	99.73
MTA15c pt110	1.26	20.74	36.52	37.69	3.14	0.01	0.76	100.12

Table B-2. Microprobe analyses of feldspar.

Analyses	Al_2O_3	SiO_2	FeO	CaO	Na_2O	K_2O	Totals
Feldspar							
MTAF13 pl1 pt1	23.57	62.32	0.09	4.64	8.88	0.03	99.54
MTAF13 pl1 pt2	23.61	62.30	0.14	4.57	8.93	0.05	99.62
MTAF13 pl1 pt3	24.13	61.42	0.11	5.00	8.46	0.09	99.21
MTAF13 pl2 pt2	23.66	62.15	0.02	4.69	8.67	0.09	99.28
MTAF13 pl2 traverse	24.84	62.20	0.03	5.55	8.64	0.04	101.31
	25.21	60.00	-0.01	6.34	7.84	0.07	99.45
	24.85	60.76	0.02	5.84	7.97	0.08	99.52
	24.75	60.75	0.01	5.65	8.18	0.08	99.41
	26.12	59.67	0.04	6.34	7.54	0.06	99.75
	25.08	60.19	0.01	6.21	8.00	0.07	99.56
	24.69	60.35	0.35	5.73	8.18	0.04	99.33
	24.84	60.38	-0.07	6.13	7.71	0.05	99.04
	25.61	59.67	0.04	6.66	7.60	0.06	99.64
	25.16	59.69	-0.14	6.83	7.50	0.08	99.12
	25.43	59.67	-0.17	6.85	7.70	0.07	99.56
	24.74	60.69	-0.02	5.86	8.15	0.04	99.47
MTA15c pl1 pt3	25.24	59.52	0.31	6.64	7.70	0.05	99.47
MTA15c pl1 pt4	23.36	63.84	0.09	4.29	9.16	0.04	100.78
MTA15c pl1 pt5	23.30	63.69	0.04	3.90	9.64	0.04	100.60
MTA15c pl1 pt6	22.57	64.12	0.02	3.23	9.55	0.05	99.53
MTA15c pl1 pt12	22.93	63.96	0.07	3.64	9.51	0.09	100.21
MTA15c pl1 pt13	22.60	64.42	0.13	3.41	9.40	0.09	100.05

Table B-3. Microprobe analyses of biotite.

Analyses	**MgO**	**Al_2O_3**	**SiO_2**	**FeO**	**MnO**	**TiO_2**	**CaO**	**Na_2O**	**K_2O**	**Total**
Biotite										
MTAF13 bt2 pt2	5.27	20.38	33.32	25.24	0.08	2.06	0.00	0.22	8.97	95.55
MTAF13 bt2 pt3	5.04	20.11	33.07	25.05	0.09	2.16	-0.01	0.28	8.76	94.56
MTAF13 bt2 pt4	5.11	19.95	33.15	25.61	0.10	2.20	0.01	0.24	8.72	95.09
MTAF13 bt2 pt5	5.23	20.21	32.72	25.51	0.13	1.93	0.00	0.30	8.67	94.71
MTAF13 bt3 pt6	5.28	20.45	32.99	24.93	0.14	1.88	-0.01	0.33	8.83	94.83
MTAF13 bt3 pt8	5.56	20.36	33.03	24.78	0.09	2.06	0.01	0.25	8.42	94.56
MTAF13 bt3 pt9	5.52	20.10	33.01	26.21	0.10	1.46	0.01	0.26	8.45	95.12
MTAF13 bt3 pt10	5.57	20.03	32.98	26.54	0.08	1.71	0.00	0.22	8.10	95.24
MTAF13 bt3 pt11	5.37	20.24	33.33	25.72	0.08	2.42	0.00	0.23	8.72	96.12
MTA15c bt1 pt1	4.84	20.08	33.12	25.59	0.10	1.62	0.01	0.29	8.53	94.19
MTA15c bt1 pt2	4.85	20.15	33.21	25.84	0.07	1.86	0.01	0.34	8.61	94.93
MTA15c bt1 pt4	4.87	20.29	32.81	25.55	0.03	2.01	-0.02	0.28	8.69	94.52
MTA15c bt2 pt1	4.84	20.13	33.09	25.34	0.05	1.71	-0.02	0.32	8.76	94.22

MTA15c bt2 pt2	5.17	20.24	32.40	27.05	0.11	1.62	0.01	0.22	7.38	94.20
MTA15c bt2 pt3	4.74	20.06	32.98	25.22	0.04	2.21	0.02	0.35	8.76	94.39
MTA15c bt3 pt1	4.72	20.25	32.48	26.75	0.06	1.70	0.00	0.27	8.68	94.92
MTA15c bt3 pt2	4.88	20.67	32.48	26.34	0.06	1.63	-0.01	0.26	8.96	95.28
MTA15c mu1 pt1	4.81	20.38	32.51	26.08	0.07	1.85	-0.01	0.27	8.71	94.67

Table B-4. Microprobe analyses of muscovite.

Analyses	**MgO**	**Al_2O_3**	**SiO_2**	**FeO**	**MnO**	**TiO_2**	**CaO**	**Na_2O**	**K_2O**	**Total**
Muscovite										
MTAF13 mu1 pt12	0.28	36.96	45.08	1.14	-0.05	0.43	0.00	1.19	9.49	94.51
MTAF13 mu1 pt13	0.23	37.02	44.60	1.14	0.03	0.48	0.00	1.02	9.44	93.98
MTAF13 mu1 pt14	0.21	36.83	44.30	1.09	0.03	0.45	-0.01	1.25	9.52	93.67
MTAF13 mu1 pt15	0.31	36.59	44.26	1.28	0.02	0.45	0.00	1.14	9.66	93.69
MTA15c mu2 pt1	0.25	36.87	43.90	0.95	0.01	0.38	0.00	1.12	9.66	93.15
MTA15c mu2 pt2	0.28	36.89	44.24	0.90	0.00	0.38	0.01	1.07	9.60	93.37

APPENDIX C

THERMOCALC DATA

Table C-1. Data file used in THERMOCALC calculations

```
% NCKFMASH datafile
% ==========================================================================
chl 4

    x(chl) 0.35 %0.35
    y(chl) 0.51 %0.51
    Q(chl) 0.485 %0.485

 % ------------------------------------------------

  p(afchl) 1  1    1  2 -1  y -1  Q

  p(clin)  2  1    0  1  2  Q
           2    0  1 -2/5  x    3  1 -1  y

  p(daph)  1  2    0  1  2/5  x    3  1 -1  y

  p(ames)  1  1    0  2  1  y -1  Q

% ------------------------------------------------
  sf

  W(afchl,clin)  18   0  0
  W(afchl,daph) 14.5 0  0
  W(afchl,ames) 20   0  0
  W(clin,daph)   2.5 0  0
  W(clin,ames)  18   0  0
  W(daph,ames)  13.5 0  0

 % ------------------------------------------------
 10

  x(Fe,M23)  1  1    0  1  1  x
  x(Mg,M23)  1  1    1  1 -1  x

  x(Al,M1)   1  1    0  2  1  y -1  Q
  x(Fe,M1)   1  2    0  1  1  x    1  2 -1  y  1  Q
  x(Mg,M1)   1  2    1  1 -1  x    1  2 -1  y  1  Q

  x(Al,M4)   1  1    0  2  1  y  1  Q
  x(Fe,M4)   1  2    0  1  1  x    1  2 -1  y -1  Q
  x(Mg,M4)   1  2    1  1 -1  x    1  2 -1  y -1  Q

  x(Al,T2)   1  1    0  1  1  y
  x(Si,T2)   1  1    1  1 -1  y

 % ------------------------------------------------
```

```
 afchl  1  4    x(Mg,M23) 4   x(Mg,M1) 1   x(Mg,M4) 1   x(Si,T2) 2
   check 0 0 0

 clin   4  5    x(Mg,M23) 4   x(Mg,M1) 1   x(Al,M4) 1   x(Al,T2) 1  x(Si,T2) 1
   check 0 1/2 1/2

 daph   4  5    x(Fe,M23) 4   x(Fe,M1) 1   x(Al,M4) 1   x(Al,T2) 1  x(Si,T2) 1
   check 1 1/2 1/2

 ames   1  4    x(Mg,M23) 4   x(Al,M1) 1   x(Al,M4) 1   x(Al,T2) 2
   check 0 1 0


% ==============================================================
st 2
     x(st) 0.89

  p(mst)   1 1      1  1 -1  x

  p(fst)   1 1      0  1  1  x

  sf

  w(st) -8 0 0

  2  x(Mg)   1 1      1  1 -1  x

     x(Fe)   1 1      0  1  1  x

  mst     1  1      x(Mg)  4

  fst     1  1      x(Fe)  4

liq 8

      q(L)     0.18
      fsp(L)   0.29
      na(L)    0.44
      an(L)    0.0043
      ol(L)    0.002
      x(L)     0.85
      h2o(L)   0.51

% ------------------------------------------------

   p(q)    1 1      0  1  1  q

   p(ab)   1 2      0  1  1  fsp    0  1  1  na

   p(ksp)  1 2      0  1  1  fsp    1  1 -1  na

   p(an)   1 1      0  1  1  an

   p(sil)  1 1      1  5 -1 q -1 fsp -1 an -1 ol -1 h2o

   p(fo)   1 2      0  1  1  ol   1  1 -1  x
```

```
  p(fa)   1 2      0  1  1  ol   0  1  1  x

  p(h2o)  1 1      0  1  1  h2o

% -------------------------------------------------
  sf

  W(qab)        12  0  -0.4
  W(qksp)       -2  0  -0.5
  W(qan)       -10  0     0
  W(qsil)       12  0     0
  W(qfo)        12  0  -0.4
  W(qfa)        14  0     0
  W(qh2o)       15  0     0

  W(abksp)      -6  0   3.0
  W(aban)        0  0     0
  W(absil)      12  0     0
  W(abfo)       10  0     0
  W(abfa)        2  0     0
  W(abh2o)       1  0  -0.2

  W(kspan)       0  0  -1.0
  W(kspsil)     12  0     0
  W(kspfo)      12  0     0
  W(kspfa)      12  0     0
  W(ksph2o)     11  0 -0.45

  W(ansil)       0  0     0
  W(anfo)        0  0     0
  W(anfa)        0  0     0
  W(anh2o)       9  0 -0.85

  W(silfo)      12  0     0
  W(silfa)      12  0     0
  W(silh2o)     16  0     0

  W(fofa)       18  0     0
  W(foh2o)      11  0  -0.5

  W(fah2o)      12  0     0

% -------------------------------------------------
  10

  fac   1 1      1  1 -1  h2o

  pq    1 1      0  1  1  q

  xab   1 2      0  1  1  fsp    0  1  1  na

  xksp  1 2      0  1  1  fsp    1  1 -1  na

  pan   1 1      0  1  1  an
```

```
   psil   1 1     1  5 -1 q -1 fsp -1 an -1 ol -1 h2o

   pol    1 1      0  1  1  ol

   xFe    1 1      0  1  1  x

   xMg    1 1      1  1 -1  x

   ph2o  1 1      0  1  1  h2o

% ------------------------------------------------
% ideal mixing activities

 qL     1  2      fac 1 pq 1
       make  1  qL 4

 abL    1  2      fac 1 xab 1

 kspL   1  2      fac 1 xksp 1

 anL    1  2      fac 1 pan 1

 silL   1  2      fac 1  psil 1
       make   1  silL  8/5
       DQF  -10 0 0

 foL    1  3      fac 1  pol 1  xMg  5
       make  1  foL 2
       DQF  -15 0 0

 faL    1  3      fac 1  pol 1  xFe  5
       make  1  faL 2
       DQF  -15 0 0

 h2oL   1  1      ph2o 2

% ======================================================================
% ternary ksp:    Cbar1 ASF

ksp   3

   na(ksp) 0.2
   ca(ksp) 0.01
% ------------------------------------------------
   p(san)   1 1    1 2 -1 na -1 ca
   p(ab)    1 1    0 1  1 na
   p(an)    1 1    0 1  1 ca
% ------------------------------------------------
   asf
     w(sanab)  25.1 -0.0108  0.338
     w(sanan)   40    0     0
     w(aban)    3.1   0     0

      san  1.0    0  0
      ab   0.643  0  0
      an   1.0    0  0
```

```
% -------------------------------------------------
   3
   x(K)     1 1    1 2 -1 na -1 ca
   x(Na)    1 1    0 1  1 na
   x(Ca)    1 1    0 1  1 ca
% -------------------------------------------------
   san      1 1     x(K) 1
   abh      1 1     x(Na) 1
   an       1 1     x(Ca) 1
      DQF   7.03  -0.00466   0
% ================================================================
% ternary plag:   Cbar1 ASF

pl 3

    ca(pl) 0.32
    k(pl) 0.005
% -------------------------------------------------
   p(ab)    1 1    1 2 -1 k -1 ca
   p(an)    1 1    0 1  1 ca
   p(san)   1 1    0 1  1 k
% -------------------------------------------------
   asf

     w(aban)   3.1   0     0
     w(sanab)  25.1 -0.0108  0.338
     w(sanan)   40   0     0

    ab   0.643  0  0
    an   1.0    0  0
    san  1.0    0  0
% -------------------------------------------------
   3
   x(K)     1 1    0 1  1 k
   x(Na)    1 1    1 2 -1 k -1 ca
   x(Ca)    1 1    0 1  1 ca
% -------------------------------------------------
   abh      1 1     x(Na) 1
   an       1 1     x(Ca) 1
      DQF   7.03  -0.00466   0
   san      1 1     x(K) 1

% ____________________________________________________________

bi 4

 x(bi) 0.50      % bulk Fe/(Fe + Mg) 0.76 % 0.50
 y(bi) 0.45      % x(Al,M1) 0.62 % 0.45
 N(bi) 0.23      % 3(x - x(Fe,M2))0.07 % 0.23

% -------------------------------------------------

  p(phl)  2 2    1  1 -1   x    1  1 -1  y
          1    0  1 -2/3   N

  p(ann)  1 1    0  2  1   x  -1/3  N
```

```
  p(east) 1 1    0  1  1   y

  p(obi)  2 2    0  1 -1   x    0  1  1  y
          1    0  1  1   N

% -------------------------------------------------

  sf

  W(phl,ann)    9  0  0
  W(phl,east)  10  0  0
  W(phl,obi)    3  0  0
  W(ann,east)  -1  0  0
  W(ann,obi)    6  0  0
  W(east,obi)  10  0  0

% -------------------------------------------------
  7

  x(Al,M1)  1 1    0  1  1   y

  x(Fe,M1)  2 2    0  1  1   x    1  1 -1  y
            1    0  1 2/3  N

  x(Mg,M1)  2 2    1  1 -1   x    1  1 -1  y
            1    0  1 -2/3 N

  x(Fe,M2)  1 1    0  2  1  x -1/3  N

  x(Mg,M2)  1 1    1  2 -1  x  1/3  N

  x(Al,T1)  1 1    1/2 1  1/2  y

  x(Si,T1)  1 1    1/2 1 -1/2  y

% -------------------------------------------------
   phl      4  4    x(Mg,M1) 1   x(Mg,M2) 2   x(Al,T1) 1   x(Si,T1) 1
        check 0 0 0

   ann      4  4    x(Fe,M1) 1   x(Fe,M2) 2   x(Al,T1) 1   x(Si,T1) 1
        check 1 0 0

   east     1  3    x(Al,M1) 1   x(Mg,M2) 2   x(Al,T1) 2
        check 0 1 0

   obi      4  4    x(Fe,M1) 1   x(Mg,M2) 2   x(Al,T1) 1   x(Si,T1) 1

        make       2   phl 2/3 ann 1/3
        DQF      -10.73  0  0
        check 1/3 0 1

%____________________________________________________________________

cd 3
     x(cd) 0.6
```

```
     h(cd) 0.5

% -------------------------------------------------

  p(crd)    1 1      1  2 -1  x -1  h

  p(fcrd)   1 1      0  1  1  x

  p(hcrd)   1 1      0  1  1  h

% -------------------------------------------------

ideal

% -------------------------------------------------

4  x(Mg)    1 1      1  1 -1  x

   x(Fe)    1 1      0  1  1  x

   h        1 1      0  1  1  h

   noth     1 1      1  1 -1  h

% -------------------------------------------------

     crd     1    2      x(Mg)  2    noth  1

     fcrd    1    2      x(Fe)  2    noth  1

     hcrd    1    2      x(Mg)  2       h  1

%__________________________________________________________________________

g 3
     x(g)   0.80   % Fe/(Fe+Mg) 0.95
     z(g)   0.06   % Ca/(Fe+Mg+Ca) 0.03

%------------------------------------------------------------------

   p(gr)   1  1    0  1  1  z
   p(alm)  1  2    1  1 -1  z    0  1  1  x
   p(py)   1  2    1  1 -1  z    1  1 -1  x

% -------------------------------------------------
   sf

   W(gr,alm)        0  0  0
   W(gr,py)        33  0  0
   W(alm,py)       2.5  0  0

% -------------------------------------------------
   3

   xFeM1   1  2    1  1 -1  z    0  1  1  x
```

```
  xMgM1   1  2    1  1 -1  z    1  1 -1  x

  xCaM1   1  1    0  1  1  z

% ------------------------------------------------

 gr      1  1      xCaM1  3

 alm     1  1      xFeM1  3

 py      1  1      xMgM1  3

% ______________________________________________________________________

opx 4

     x(opx) 0.5   % Fe/*Fe+Mg)
     y(opx) 0.15  % x(Al,M1)
     N(opx) 0.38  % 2(x(Fe,M2) - x)

% ------------------------------------------------

   p(en)   1 1   1  3 -1  x -1  y -1/2 N

   p(fs)   2 1   0  1       -1/2 N
           2   0  1  1  x    1  1 -1  y

   p(mgts) 1 1   0  1  1  y

   p(fm)   2 1   0  1  1  N
           2   0  1  1  x    0  1  1  y

% ------------------------------------------------
 sf

  W(en,fs)      6.8  0  0
  W(en,mgts)      0  0  0
  W(en,fm)      4.5  0  0
  W(fs,mgts)     -1  0  0
  W(fs,fm)      4.5  0  0
  W(mgts,fm)    1.2  0  0

% ------------------------------------------------

 5

 x(Al,M1) 1 1   0  1  1  y

 x(Mg,M1) 2 1   1  2 -1  y  1/2 N
          2   0  1 -1  x    1  1 -1  y

 x(Fe,M1) 2 1   0  1       -1/2 N
          2   0  1  1  x    1  1 -1  y

 x(Mg,M2) 1 1   1  2 -1  x -1/2 N
```

```
 x(Fe,M2) 1 1   0  2  1  x  1/2 N

% ------------------------------------------------

     en      1  2     x(Mg,M1)  1   x(Mg,M2) 1
        check 0 0 0

     fs      1  2     x(Fe,M1) 1   x(Fe,M2) 1
        check 1 0 0

    mgts     1  2     x(Al,M1) 1   x(Mg,M2) 1
        check 0 1 0

     fm      1  2     x(Mg,M1)  1   x(Fe,M2) 1
        check 1/2 0 1
        make       2      en 1/2    fs 1/2
        DQF    -6.95  0  0

% ====================================================================
% NKFMASH white mica, after Coggon&Holland, 2002

mu  4

          fe(mu)      0.45  % Fe/(Fe+Mg) %0.45
          y(mu)       0.96  % XAl,M2A %.96
          na(mu)       0.05  % XNa,A 0.11 %.05
          % ------------------------------------------------
          p(mu)       1 1   0  2  1 y -1  na
          p(pa)       1 1   0  1  1 na
          p(cel)      1 2   1  1 -1 fe       1  1 -1  y
          p(fcel)     1 2   0  1  1 fe       1  1 -1  y
          % ------------------------------------------------
  asf
     W(mu,pa)     10.12 0.0034  0.353
     W(mu,cel)     0.00 0.0000  0.200
     W(mu,fcel)    0.00 0.0000  0.200
     W(pa,cel)    52.00 0.0000  0.000
     W(pa,fcel)   52.00 0.0000  0.000
     W(cel,fcel)   0.00 0.0000  0.000

     mu           0.63 0.0 0.0
     pa           0.37 0.0 0.0
     cel          0.63 0.0 0.0
     fcel         0.63 0.0 0.0
          % ------------------------------------------------
   7
     x(K,A)      1  1   1  1 -1  na
     x(Na,A)     1  1   0  1  1  na
     x(Al,M2A)   1  1   0  1  1  y
     x(Fe,M2A)   1  2   0  1  1  fe    1  1 -1  y
     x(Mg,M2A)   1  2   1  1 -1  fe    1  1 -1  y
     x(Si,T1)    1  1   1  1 -1/2  y
     x(Al,T1)    1  1   0  1  1/2  y
          % ------------------------------------------------
     mu         4  4  x(K,A) 1    x(Al,M2A) 1 x(Al,T1) 1  x(Si,T1) 1
                  check 0  1  0
```

```
    pa        4  4  x(Na,A) 1   x(Al,M2A) 1 x(Al,T1) 1  x(Si,T1) 1
                   check 0  1  1
    cel       1  3   x(K,A) 1    x(Mg,M2A) 1 x(Si,T1) 2
                   check 0  0  0
    fcel      1  3   x(K,A) 1    x(Fe,M2A) 1 x(Si,T1) 2
                   check 1  0  0
%___________________________________________________________________

ky sill and q H2O zo pa ma

*

fluidpresent yes
fluidexcess no
setexcess q
setallcomps

ignore

setdefTwindow   200 1300
setdefPwindow   2  11

pseudo yes
% ----------------------------------------------
% ----------------------------------------------
% MTA12 XRF mole% of oxides analysis
% ----------------------------------------------
%           H2O SiO2  Al2O3  CaO  MgO  FeO  K2O  Na2O
setbulk yes 8.00 67.45 14.75  0.92 3.28 10.00 2.51 1.10
% ----------------------------------------------
setmodeiso yes
zeromodeiso yes
setiso no

project no

drawpd yes
moreprec

*
```

Note water is set at 8 mol% for calculations above the solidus. Below the solidus water is in excess and therefore taken out of the bulk composition and just set as fluidexcess in the scripts.

Table C-2. Independent sets of reactions from Average Pressure-Temperature results using data from samples MTAF13 and MTA15with and without the muscovite end-member.

Average Pressure

MTA15c

Independent set of reactions

1) gr + q + 2sill = 3an
2) py + gr + mu = phl + 3an
3) py + 2gr + 3east + 6q = 3phl + 6an
4) gr + alm + mu = ann + 3an

MTAF13

Independent set of reactions

1) ann + q + 2sill = alm + mu
2) py + 2gr + 3east + 6q = 3phl + 6an
3) gr + 3east + 6q = 2phl + 3an + mu
4) 2phl + 5ann + 12sill = 5alm + 3east + 4mu

Average Temperature

MTA15c

Independent set of reactions

1) 7phl + 12sill = 5py + 3east + 4mu
2) 3phl + 4sill = py + 3east + 4q
3) ann + q + 2sill = alm + mu
4) 4gr + 3phl + 12sill = py + 3east + 12an

MTAF13

Independent set of reactions

1) 7phl + 12sill = 5py + 3east + 4mu
2) 3phl + 4sill = py + 3east + 4q
3) ann + q + 2sill = alm + mu
4) 2gr + 3alm + 3east + 6q = 2py + 3ann + 6an

Average Pressure, No Muscovite

MTA15c

Independent set of reactions

1) gr + q + 2sill = 3an
2) py + 2gr + 3east + 6q = 3phl + 6an
3) 2py + 4gr + 3ann + 12sill = 3alm + 3east + 12an

MTAF13

Independent set of reactions

1) gr + q + 2sill = 3an
2) py + 2gr + 3east + 6q = 3phl + 6an
3) 2gr + 3alm + 3east + 6q = 2py + 3ann + 6an

Average Temperature, No Muscovite

MTA15c

Independent set of reactions

1) 3phl + 4sill = py + 3east + 4q
2) 4gr + 3phl + 12sill = py + 3east + 12an
3) py + ann = alm + phl

MTAF13

Independent set of reactions

1) 3phl + 4sill = py + 3east + 4q
2) py + ann = alm + phl
3) 2gr + 3alm + 3east + 6q = 2py + 3ann + 6an

References Cited

Armstrong, R., 1972. Low-angle (denudation) faults, hinterland of the Sevier orogenic belt, eastern Nevada and western Utah. Geological Society of America Bulletin, v. 83, p. 1729-1754.

Bloomfield, S., 1983. The Proterozoic Greyson-Spokane Transition Sequence: a Stratigraphic and Gravity Study, west-central Montana. Thesis, Department of Geosciences, University of Montana.

Brown, R., and Read, P., 1983. Shuswap terrane of British Columbia: a Mesozoic 'core complex'. Geology, v. 11, p. 164-168.

Burchfield, B.C., Cowan, D., and Davis, G., 1992. "Tectonic overview of the cordilleran orogen in the western United States." The Cordilleran Orogen: Coterminous U.S. Volume G-3 Decade of North American Geology. Eds., B. C. Burchfiel, P. W. Lipman, and M. L. Zoback. Boulder, CO: Geological Society of America, pp. 407-480.

Burmester, R. F., McClelland, W. C., and Lewis, R. S., 2004, U-Pb dating of plutons along the transfer zone between the Bitterroot and Priest River metamorphic core complexes: Geological Society of America Abstracts with Programs, v. 36, p. 72.

Carey, J.W., Rice, J., and Grover, T., 1992. Petrology of Aluminous Schist in the Boehls Butte Region of Northern Idaho: Geologic History and Aluminum-Silicate Phase Relations. American Journal of Science, v. 292, p. 445-473.

Carr, S., and Simony, P., 2002. Cretaceous-early Tertiary tectonic evolution of the Valhalla Complex, southern Omineca Belt, British Columbia. Abstracts with Programs; Geological Society of America, v.34, no.6, p.109.

Coney, P., 1974. Structural Analysis of the Snake Range 'Decollement,' East-Central Nevada. Geological Society of America Bulletin, v. 85, no. 6, p. 973 – 978.

Coney, P., 1980. Cordilleran metamorphic core complexes: An overview *in* Cordilleran Metamorphic Core Complexes. Eds. Crittenden, M., D. Jr., Coney, P., and Davis, H. Geological Society of America, Memoir 153.

Coney, P., 1980a. Introduction. *in* Cordilleran Metamorphic Core Complexes. ed. Crittenden, M Jr., Coney, P., and Davis, H. Geological Society of America, Memoir 153.

Coney, P.J., and Harms, T.A., 1984. Cordilleran Metamorphic Core Complexes; Cenozoic Extensional Relics of Mesozoic Compression. Geology, v. 12, p. 550-554.

Crittenden, M. Jr., Coney, P., and Davis G., 1978. Penrose Conference Report. Tectonic significance of metamorphic core complexes in the North American Cordillera. Geology, v. 6, no. 2, p. 79.

Davis, G., 1977. Characteristics of metamorphic core complexes, southern Arizona. Geological Society of America Abstracts with Programs, v. 9, p.944.

Davis, G., and Coney, P., 1979. Geologic development of the Cordilleran metamorphic core complexes. Geology, v. 7, no. 3, p. 120-124.

Doughty, T., 2002. Eocene Structural Evolution of the Boehls Butte Anorthosite and Clearwater Core Complex, North Central Idaho: A Basement-Involved Extensional Strike-Slip Relay. Abstracts with programs: Geological Society of America, v. 34, no. 6, p.332.

Doughty, P. T., and Chamberlain, K. R., 2004. New U-Pb SHRIMP evidence for multiple metamorphic events in the northern U.S. Cordillera: Eocene, Cretaceous, and late Precambrian (Grenville) events: Geological Society of America Abstracts with Programs, v.36, p. 271.

Doughty, T., and Price, R., 1999. Tectonic evolution of the Priest River complex, northern Idaho and Washington- A reappraisal of the Newport fault with new insights on metamorphic core complex formation. Tectonics, v. 18, no. 3, p.375-393.

Doughty, T., and Price, R., 2000. Geology of the Purcell Trench rift valley and Sandpoint Conglomerate: Eocene en echelon normal faulting and synrift sedimentation along the eastern flank of the Priest River metamorphic complex, northern Idaho. GSA Bulletin, v. 112, no. 9, p. 1356–1374.

Emmons, W.H., and Calkins, F.C,. 1913. Geology and ore deposits of the Philipsburg quadrangle, Montana. U.S. Geological Survey, Professional Paper 78.

Eyal, Y., Osadetz, K., and Feinstein, S., 2006. Evidence of reactivation of Eocene joints and pre-Eocene foliation planes in the Okanagan core complex, British Columbia, Cananda. Journal of Structural Geology, 28, p. 2109-2120.

Grover, T., Rice, J., and Carey, J.W., 1992. Petrology of Aluminous Schist in the Boehls Butte Region of Northern Idaho: Phase Equilibria and P-T Evolution. American Journal of Science, v. 292, p. 474-507.

Foster, D.A., 2000. Tectonic evolution of the Eocene Bitterroot metamorphic core complex, Montana and Idaho *in* Geological field trips, western Montana and adjacent areas, Eds. Roberts, S., and Winston, D., Rocky Mountain Section of the Geological Society of America, University of Montana, p. 1-29.

Foster, D., Doughty, P., Kalakay, T., Fanning, C., Coyner, S., Grice, W., and Vogl, J., 2007. Kinematics and Timing of Exhumation of Metamorphic Core Complexes Along the Lewis and Clark Fault Zone, Northern Rocky Mountains, USA *in* Exhumation

Associated with Continental Strike-Slip Fault Systems. Eds. Till, A., Roeske, S., Sample, J., and Foster, D. Geological Society of America Special Paper 434.

Foster, D. and Fanning, M., 1997. Geochronology of the northern Idaho batholith and the Bitterroot metamorphic core complex: Magmatism preceding and contemporaneous with extension. GSA Bulletin, v.109, no.4, p. 379-394.

Foster, D. and Kalakay, T., 2003. Exhumation and kinematics of Eocene metamorphic core complexes along the Lewis and Clark strike-slip system. Geological Society of America Abstracts, no. 182-2, November 2-5.

Foster, D., Schafer, C., Fanning, C., and Hyndman, D., 2001. Relationships between crustal partial melting, plutonism, orogeny, and exhumation: Idaho-Bitterroot batholith. Tectonophysics, 342, p. 313-350.

Garmezy, L., 1983. Geology and geochronology of the southeast border of the Bitterroot dome: implications for the structural evolution of the mylonite carapace. PhD dissertation, Pennsylvania State University, University Park, Pennsylvania.

Grice, W. C. Jr., 2006. Exhumation and Cooling History of the Middle Eocence Anaconda Metamorphic Core Complex, Western Montana. Thesis, Department of Geological Sciences, University of Florida.

Grice, W.C., Foster, D., and Kalakay, T., 2005. Quantifying Exhumation and Cooling of the Eocene Anaconda Metamorphic Core Complex, western Montana. Geological Society of America Annual Meeting Abstracts, no. 98-9.

Grice, W. C., Foster D., Kalakay, T., Bleik, H., and Hodge, K., 2004. Style and timing of crustal attenuation in the Anaconda metamorphic core complex, western Montana. Geological Society of America Abstracts, Denver, session 236.

Hodges, K. V. and Applegate, J., 1993. Age of Tertiary extension in the Bitterroot metamorphic core complex, Idaho-Montana. Geology (Boulder), v.21, no.2, p.161-164.

Holdaway, M.J., 1971. Stability of andalusite and the aluminum silicate phase diagram. American Journal of Science, 271, 97–131.

Holland, T.B. and Powell, R., 1998. An internally consistent thermodynamic data set for phases of petrologic interest: Journal of Metamorphic Petrology, v. 16, p. 309-342.

House, M. and Hodges, K.V., 1994. Limits on the tectonic significance of rapid cooling events in extensional settings; insights from the Bitterroot metamorphic core complex, Idaho-Montana. Geology (Boulder), v.22, no.11, p.1007-1010.

House, M.A., Hodges, K.V., and Bowring, S.A., 1997. Petrological and geochronological constraints on regional metamorphism along the northern border of the Bitterroot batholith. Journal of Metamorphic Geology, v. 15, no. 6, pp 753-764.

Johnson, B., 2006. Extensional shear zones, granitic melts, and linkage of overstepping normal faults bounding the Shuswap metamorphic core complex, British Columbia. GSA Bulletin, March/April 2006, v. 118, no. ¾, p. 366–382.

Johnson, T. E., Brown, M., and Solar, G. S., 2003. Low–pressure subsolidus and suprasolidus phase equilibria in the MnNCKFMASH system: Constraints on conditions of regional metamorphism in western Maine, northern Appalachians. American Mineralogist, v. 88, p. 624–638.

Kalakay, T., Foster, D., and Grice, W.C., 2004. Tectonomagnetic architecture of the Sevier orogenic wedge of western Montana. Geological Society of America Abstracts, Denver, session 184.

Kalakay, T., John, B., and Lageson, D., 2001. Fault-controlled pluton emplacement in the Sevier fold-and-thrust belt of southwest Montana, USA. Journal of Structural Geology, 23, p. 1151-1165.

Kalakay, T., Foster, D., and Lonn, J., 2004a. Growth and collapse of the Sevier tectonic wedge: New evidence from the cordillera of western Montana. Geological Society of America Abstracts, Rocky Mountain (56th) and Cordilleran (100th) joint meeting, n. 23-8.

Kalakay, T., Foster, D., and Thomas, R., 2003, Geometry, kinematics and timing of extension in the Anaconda extensional terrane, western Montana: Northwest Geology, v. 32, p. 124-133.

Lang, H., and Rice, J., 1985. Geothermometry, Geobarometry, and T-X (Fe-Mg) Relations in Metapelites, Snow Peak, Northern Idaho. Journal of Petrology, v. 26, part 4, p.889-924.

Liu, M., 2001. Cenozoic extension and magmatism in the North American Cordillera: the role of gravitational collapse. Tectonophysics, v. 342, p.407– 433.

Lonn, J., McDonald, C., Lewis, R., Kalakay, T., O'Neill, J., Berg, R., and Hargrave, P., 2003. Preliminary Geologic Map of the Philipsburg 30' x 60' Quadrangle, Western Montana. Montana Bureau of Mines and Geology, Open File No. 48.

Lorencak, M., Seward, D., Vanderhaeghe, O., Teyssier, C., and Burg, J., 2001. Low-temperature cooling history of the Shuswap metamorphic core complex, British Columbia: constraints from apatite and zircon fission-track ages. Can. J. Earth Sci., 38, p. 1615–1625.

Madsen, J., Thorkelson, D., Friedman, R., and Marshall, D., 2006. Cenozoic to Recent Plate Configuration of the Pacific basin: Ridge subduction and slab window magmatism in western North America. *Geosphere*, v. 2, no. 1, p. 11–34.

Misch, P., 1960. Regional structural reconnaissance in central-northeast Nevada and some adjacent areas: Observations and interpretations. Intermountain Association of Petroleum Geologist, 11th Annual Field Conference, Guidebook, p. 17-42.

O'Neill, J., and Lageson, D., 2003, West to east geologic road log: Paleogene Anaconda metamorphic core complex: Georgetown Lake Dam – Anaconda - Big Hole Valley: Northwest Geology, v. 32, p. 29-46.

O'Neill, J., Lonn, J., Lageson, D., and Kunk, M., 2004. Early Tertiary Anaconda Metamorphic Core Complex, southwestern Montana. Canada Journal Earth Science, 41, p. 63 -72.

Pauli, S., Kalakay, T., and Wolfe, M., 2003. Exposing the brittle-plastic transition in a deeply-rooted detachment system, Anaconda extensional terrane, western Montana. Geological Society of America Abstracts, Rocky Mountain Section Meeting, section 9.

Porder, S., 1997. Metamorphism and metasomatism of the Lower Prichard Formation: a petrologic, geochemical and thermobarometric study of the lowermost member of the Belt/Purcell Supergroup. Thesis, Department of Geosciences, University of Montana.

Powell, R. and Holland, T., 1988. An internally consistent dataset with uncertainties and correlations; 3, Applications to geobarometry, worked examples and a computer program. Journal of Metamorphic Geology, 6, 173–204.

Powell, R., and Holland, T., 1994. Optimal geothermometry and geobarometry. American Mineralogist, v. 79, p. 120-133.

Rey, P., Vanderhaeghe, O., and Teyssier, C., 2001. Gravitational collapse of continental crust: definition, regimes and modes. Tectonophysics 342, p. 435– 449.

Schaubs, P. and Carr, S., 1998. Geology of metasedimentary rocks and Late Cretaceous deformation history in the northern Valhalla complex, British Columbia. Can. J. Earth Sci., 35, p. 1018–1036.

Sears, J., and Hendrix, M., 2004. Lewis and Clark Line and the rotational origin of the Alberta and Helena salients, North America Cordillera. Geological Society of America, Special Paper 383.

Silverberg, D., 1990. The tectonic evolution of the Pioneer metamorphic core complex, south-central Idaho. Thesis, Department of Earth, Atmospheric, and Planetary Sciences, Geology, Massachusetts Institute of Technology.

Spear, F., 1993, Metamorphic Phase Equilibria and Pressure-Temperature Paths: Monograph, Mineralogical Society of America, Washington DC, USA, 799 p.

Spear, F., 2004. Fast cooling and exhumation of the Valhalla metamorphic core complex, southeastern British Columbia. International Geology Review, v.46, no.3, p.193-209.

Tinkham, D., Zuluaga, C., and Stowell, H., 2001. Metapelitic phase equilibria modeling in MnNCKFMASH: the effect of variable Al_2O_3 and MgO/(MgO +FeO) on mineral stability. Geological Materials Research, 3, p. 1-42.

United States Geological Survey (USGS) 2005. http://pubs.usgs.gov/of/2005/1235/export/nr_geo_mud.txt. Accessed February 19, 2007.

Vanderhaeghe, O., Teyssier, C., McDougall, I., and Dunlap, W., 2003. Cooling and exhumation of the Shuswap Metamorphic Core Complex constrained by $^{40}Ar/^{39}Ar$ thermochronology. GSA Bulletin, v. 115, no. 2, p. 200–216.

Waters, D., 2008. http://www.earth.ox.ac.uk/~davewa/pt/pt02_mica.html. Last modified October 12, 2004. Accessed November, 2007.

White, R., Powell, R., and Holland, J., 2007. Progress relating to calculation of partial melting equilibria for metapelites. Journal of Metamorphic Geology, v. 25, p. 511-527.

Yin, A., and Oertel, G., 1995. Strain analysis of the Ninemile fault zone, western Montana: insights into multiply deformed regions. Tectonophysics, 247. pp. 133-143.